THE UNIVERSITY
of ADELAIDE

Trailing Edge Noise Prediction Using a RANS-based Statistical Method (RSNM)

Cristobal Albarracin

School of Mechanical Engineering
The University of Adelaide
South Australia 5005
Australia

A thesis submitted in fulfillment of the
requirements for the degree of Ph. D. in
Engineering on December 10, 2018

Ph. D. Thesis

Accepted version
one day in the near future

School of Mechanical Engineering
The University of Adelaide
South Australia 5005
Australia

Typeset by the author using LaTeX.
Printed in Australia.

Abstract

Airfoil self noise is produced when an airfoil is immersed in an undisturbed flow. Flow turbulence created in the boundary layer and wake of the airfoil generates pressure fluctuations, which are scattered by the trailing edge (TE), radiating noise to the far field. TE noise is one of the dominant mechanism of airfoil self noise in low Mach number, high Reynolds Number flows. These conditions occur in many applications such as wind turbines, aircraft, submarines, fans, air conditioning units and turbomachinery in general.

The overall aim of this research is to investigate and develop a RANS-based Statistical Noise Model (RSNM) for trailing edge noise. The method combines Reynolds-averaged Navier-Stokes (RANS) turbulent flow solutions with statistical models of the turbulent flow field, namely the turbulent velocity cross-spectrum.

Hot wire anemometry is used to investigate the flow in the boundary layer of sharp edged struts with zero pressure gradient (ZPG) and adverse pressure gradients (APG). Single-point and two-point statistics are presented, including mean and RMS velocity profiles, probability density functions, third and fourth order moments, power spectral density, two-point correlations and coherence function. An empirical model for the turbulent velocity cross-spectrum is developed, based on the measured statistics. The cross-spectrum model is constructed by combining an autospectrum model and a model for the spatial coherence function.

RANS computational fluid dynamics (CFD) simulations are performed for three different two-dimensional airfoils (NACA 0012, DU-96-180 and the FP12 flat sharp-edged strut) at a wide range of operating conditions. The simulation results are validated against new experimental data, as well as data from the literature. The CFD results are sampled in the region around the trailing edge and used as input data to the noise prediction model.

Noise calculations are performed for all cases using different turbulent velocity cross-spectrum models. The baseline model is an adaptation of the Gaussian formulation

used in jet noise predictions by Morris and Farassat (2002), which is modified to account for the presence of the sharp trailing edge. Modifications to the cross-spectrum model are assembled by changing the auto-spectrum model and/or the model for the spatial coherence function.

Noise predictions for the NACA 0012 and DU-96-10 airfoils using the baseline model are in excellent agreement with experimental data. Noise predictions for the FP12 airfoil produced the correct slope, but underpredicted the noise levels by up to 15 dB.

The baseline model outperformed all the modifications investigated in this thesis.

Declarations

Originality

This work contains no material which has been accepted for the award of any other degree of diploma in any university or other tertiary institution. To the best of my knowledge and belief, this work contains no material previously published or written by another person, except where due reference has been made in the text.

Permissions

I give consent to this copy of my thesis, when deposited in the University Library, being made available for loan and photocopying, subject to the provisions of the Copyright Act 1968.

I also give permission for the digital version of my thesis to be made available on the web, via the University's digital research repository, the Library catalogue, the Australasian Digital Theses Program (ADTP) and also through web search engines, unless permission has been granted by the University to restrict access for a period of time.

Acknowledgements

I would like to acknowledge all of the people and institutions who have contributed to this thesis or supported me during my time as a postgraduate student.

First of all, to my supervisors, Professor Con Doolan, Professor Colin Hansen and Dr Laura Brooks. Without their guidance, this thesis would never have been completed.

I would like to thanks all the people in the school of Mechanical Engineering who provided technical help, ideas and useful discussions that contributed to the work presented here. In particular, many thanks to Dr Jesse Coombs for his helpful advice on statistics and on CFD matters, to Dr Danielle Moreau for her help with hot wire anemometry and for facilitating some of the data for validation and to Richard Jones for his help with OpenFoam.

I would like to thank my parents, for their unwavering support, both emotional and financial. Without their support I would have been unable to start this work, let alone finish it.

Many thanks to Dr Christopher Tome and Ms Jennifer Short, for their sharp eyes as proof readers and their continuous encouragement.

Most importantly, I would like to express my gratitude to my wife Macarena for her extraordinary patience and encouragement, which eventually resulted in the completion of this thesis.

Finally, many thanks to the Chilean Government and CONICYT for their financial support through the scholarship program Becas Chile.

Contents

Abstract **i**

Declarations **iii**

Acknowledgements **v**

Nomenclature **xi**

1 Introduction **1**

1.1 Literature review 2

1.1.1 Empirical methods 4

1.1.2 Direct methods 4

1.1.3 Hybrid methods 6

1.1.3.1 Methods based on time accurate CFD 7

1.1.3.2 RANS based methods 8

1.1.3.3 Stochastic Noise Generation and Radiation (SNGR) 9

1.1.3.4 Surface pressure approach 9

1.1.3.5 Methods based on statistical models for the two-point velocity correlation 11

1.1.4 Available models for the velocity two-point velocity correlation 12

1.2 Summary 13

1.3 Aims and objectives 13

1.4 Contributions to the field 14

1.5 Publications arising from this thesis 15

2 Experimental methods **17**

2.1 Experimental setup 17

2.2 Airfoil models 18

2.3 Aligning the traverse 18

2.4 Hot wire anemometry 19

2.4.1 Frequency response of the anemometer . . . 20
2.4.2 Calibration . . . 20
2.5 Error analysis . . . 21
2.5.1 Uncertainty specification for measured statistical quantities . . 23
2.5.2 Digital signals . . . 24
2.5.3 Mean velocity . . . 24
2.5.4 RMS velocity . . . 25
2.5.5 Higher order moments . . . 26
2.5.6 Autocorrelations . . . 26
2.5.7 Cross-correlation . . . 27
2.5.8 Autospectrum . . . 27
2.5.9 Probability density functions . . . 28
2.6 Summary . . . 29

3 Experimental results **35**
3.1 Integral boundary layer parameters . . . 36
3.1.1 Mean and RMS velocity profiles . . . 38
3.1.2 Turbulence dissipation . . . 39
3.1.3 Probability density functions . . . 39
3.1.4 Higher order moments . . . 41
3.1.5 Integral length scale . . . 42
3.1.6 Autocorrelation function . . . 44
3.1.7 Turbulent velocity two-point correlation . . . 44
3.1.8 Turbulent velocity auto-spectrum . . . 46
3.1.9 Turbulent velocity cross-spectrum . . . 54
3.1.10 Coherence function . . . 54
3.2 Summary . . . 56

4 Derivation of the Noise Prediction Method **59**
4.1 Introduction . . . 59
4.2 Model derivation . . . 59
4.2.1 Cross-spectrum model . . . 63
4.3 Alternative cross-spectrum models . . . 64
4.4 Spatial coherence models . . . 65
4.4.1 Gavin's Simplified Anisotropic Model (SAM) . . . 66
4.4.2 Proposed semi-empirical model . . . 67
4.4.2.1 Dependency on spatial separation in the wall-normal direction. . . . 68

4.4.2.2 Dependency on spatial separation in the spanwise direction. . . . 69
4.4.2.3 Dependency on spatial separation in the streamwise direction. . . . 69
4.5 Autospectrum models . . . 73
4.5.1 Gaussian spectrum . . . 75
4.5.2 Pope's model spectrum . . . 76
4.6 RANS implementation . . . 78
4.6.1 Correction for finite span . . . 79
4.6.1.1 Calculating the noise from a single strip . . . 80
4.7 Summary . . . 82

5 Numerical investigation **85**
5.1 RANS . . . 85
5.2 The SST $k-\omega$ turbulence model . . . 86
5.3 Numerical schemes . . . 87
5.4 Boundary conditions . . . 88
5.5 Selected airfoils . . . 89
5.6 The computational grids . . . 90
5.7 Verification of CFD results . . . 90
5.7.1 NACA-0012 airfoil . . . 93
5.7.2 Du-96-180 airfoil . . . 94
5.7.3 FP-12 airfoil . . . 94
5.8 Summary . . . 97

6 Results **99**
6.1 Introduction . . . 99
6.2 Sampling domain . . . 99
6.3 RANS CFD results for the NACA 0012 airfoil . . . 100
6.3.1 Reynolds number effects . . . 101
6.3.2 Effect of angle of attack . . . 101
6.4 Validation of RANS data for the NACA 0012 airfoil . . . 103
6.5 RANS CFD results for the DU-96-180 airfoil . . . 105
6.5.1 Reynolds number effects for the Du-96-180 airfoil . . . 106
6.5.2 Effect of angle of attack for the Du-96-180 airfoil . . . 107
6.6 Validation of RANS data for the Du-96-180 airfoil . . . 108
6.7 RANS CFD results for the FP12 airfoil . . . 109
6.8 Acoustic results fo the NACA 0012 airfoil . . . 111

6.8.1 Zero angle of attack . . . 113
6.8.1.1 Effect of changing the spatial coherence model 116
6.8.2 Non-zero angle of attack . . . 116
6.9 Acoustic results for the DU-96-180 . . . 117
6.10 Acoustic results for the FP12 airfoil . . . 119
6.11 Effect of length scales on acoustic results . . . 120
6.12 Effect of underpredicting turbulent kinetic energy and dissipation. . . . 120
6.13 Effect of incorrectly modelling the turbulence spectrum . . . 121
6.14 Summary . . . 122

7 Conclusions and future work **135**
7.1 Future work . . . 139

Appendices **151**

A Two-point correlation curve fits at various y/δ locations. **153**

B Alternative correction for finite span **159**
B.1 RANS implementation . . . 159
B.1.1 Correction for finite span . . . 160

Nomenclature

C_f	Skin friction coefficient
E	Velocity spectrum function
E_{11}	Longitudinal velocity spectrum
H	Shape factor, δ^*/θ
K	Kurtosis
L	Length scale , $c_\ell k^{3/2}/\epsilon$
L_{11}	Longitudinal integral length scale
R_{11}	Longitudinal velocity correlation
Re_θ	Reynolds number based on momentum thickness
Re_c	Reynolds number based on chord
S	Skewness
$S(\mathbf{x}, \omega)$	Power spectral density of the far field pressure
T_i	Turbulence intensity
U_∞	Free stream velocity
U_c	Convection velocity
Λ_f	Correlation length
β	Pressure gradient parameter
δ	Boundary layer thickness
δ^*	Displacement thickness
δ_{ij}	Kronecker delta

ℓ	Correlation length scale
ℓ_s	Length scale
ℓ_{sz}	Spanwise coherence length
ϵ	Turbulence dissipation
η	Kolmogorov scale, $(\nu^3/\epsilon)^{1/4}$
γ^2	Coherence function
κ	Wavenumber
$\mathbf{u}$	Velocity vector
$\mathbf{y}$	Source location
μ	Dynamic molecular viscosity
μ_t	Eddy viscosity
ν	Kinematic viscosity
ω_s	Frequency scale, $2\pi/\tau_s$
ρ	Fluid density
τ_s	Time scale, $c_\tau k/\epsilon$
τ_w	Wall shear stress
θ	Momentum thickness
c	Airfoil chord
c	Speed of sound
c_ℓ	Length scale coefficient
c_τ	Time scale coefficient
erf	Gauss error function
f_a	Anisotropy factor
k	Turbulence kinetic energy
k_a	Acoustic wave number
p_{ij}	Compressive stress tensor
u_τ	Friction velocity

u_s Velocity scale, $\sqrt{2k/3}$

List of Figures

2.1 Schematic of the wind tunnel contraction with extension plates and model used in the experiments. The coordinate system was centered at the trailing edge of the model at the mid span point. 30
2.2 Experimental setup. 30
2.3 Test cases used in the experiments. The models have a trailing edge of 1 mm thickness. 31
2.4 The CT anemometer containing a Wheatstone bridge, a feedback amplifier, and an electronic testing subcircuit, adapted from Bruun (1995). 32
2.5 Ideal response of the CT anemometer to the square wave test. 32
2.6 Typical calibration curves for before (red) and after (blue) a set of measurements. 32
2.7 Local Turbulence Intensity as a function of normalized distance to the wall. 33
2.8 Integral time scale and number of statistically independent samples for measurements in the near wake of the FP-12. 33
2.9 Normalized error for the mean and RMS velocity. 33
2.10 Normalized error for the skewness and kurtosis. 34
2.11 Normalized error for the probability density function as a function of normalized distance to the wall. 34

3.1 Mean Velocity and turbulent kinetic energy profiles and curve fits used to calculate the boundary layer thickness δ,for the ZPG case. $x/c = 1.0008$ 37
3.2 Pressure on the surface for all cases obtained from CFD. 37
3.3 Skin friction coefficient and shape factor as a function of Reynolds number. Current data in ascending Re_θ: Case 1, Case 3, Case 2. . . . 38
3.4 Mean and RMS velocity profiles in wall units. Measurements taken at $x/c = 1.0008$. Circles in Figure 3.4(b) as in legend of Figure 3.4(a). 40

3.5 Turbulence dissipation as a function of normalized distance to the wall. $x/c = 1.0008$ 40
3.6 Probability density functions of turbulent velocity. $x/c = 1.0008$. . . . 42
3.7 Third and fourth order moments of the streamwise velocity measured at $x/c = 1.0008$. 43
3.8 Length scales normalized by boundary layer thickness. Data obtained at $x/c = 1.0008$. 45
3.9 Streamwise autocorrelation for various values of y/δ. $x/c = 1.0008$. . 45
3.10 Two-point correlation for different probe separation values in the wall normal direction Case 1. $x/c = 1.0033$. 47
3.11 Two-point correlation for different probe separation values in the spanwise direction for Case 1. $x/c = 1.0033$. 48
3.12 Two-point correlation for different probe separation values in the wall normal direction for Case 2. $x/c = 1.0033$. 49
3.13 Two-point correlation for different probe separation values in the spanwise direction for Case 2. $x/c = 1.0033$. 50
3.14 Two-point correlation for different probe separation values in the wall normal direction for Case 3. $x/c = 1.0033$. 51
3.15 Two-point correlation for different probe separation values in the spanwise direction for Case 3. $x/c = 1.0033$. 52
3.16 Two-point correlation contours at $y^+ \approx 80$. $x/c = 1.0033$. 53
3.17 Two-point correlation contours at $y/\delta \approx 0.3$. $x/c = 1.0033$. 53
3.18 One-dimensional longitudinal velocity autospectra normalized by Kolmogorov scales, at various positions in the boundary layer. $x/c = 1.0008$. 55
3.19 Cross-spectral density in the wall-normal direction for Case 2. $y/\delta = 0.23$. $x/c = 1.0033$. 55
3.20 Coherence function as a function of $\kappa_1\eta$ for Case 2 at $y/\delta = 0.232$. Measurements taken at $x/c = 1.0033$. 57

4.1 The coordinate system of Ffowcs Williams and Hall (1970). 60
4.2 Measured cross-spectrum (circles) and cross-spectrum calculated using equation 4.29 (solid lines) for Case 2 at $y/\delta = 0.13$. 65
4.3 a)Wall-normal coherence at $y/\delta = 0.39$. b) length scale coefficient c_{ℓ_y} as function of distance to the wall. Data taken at 1 mm downstream of the TE for Case 2. Results for other values of y/δ, and their corresponding exponential fits are shown in Figures A.1(a) to A.1(k). 70

4.4 a)Wall-normal coherence at $y/\delta = 0.55$. b) length scale coefficient c_{ℓ_y} as function of distance to the wall. Data taken at 1 mm downstream of the TE for Case 1. Results for other values of y/δ, and their corresponding exponential fits are shown in Figures A.2(a) to A.2(e). 70
4.5 a)Wall-normal coherence at $y/\delta = 0.39$. b) length scale coefficient c_{ℓ_y} as function of distance to the wall. Data taken at 1 mm downstream of the TE for Case 3. Results for other values of y/δ are shown in Figures A.3(a) to A.3(e). 71
4.6 a) Spanwise coherence for at $y/\delta = 0.39$. b) Empirical parameter c_{ℓ_z}, linear fit and residuals. Data taken at 1 mm downstream of the TE for Case 2. 71
4.7 a) Spanwise coherence for $y/\delta = 0.52$. b) Empirical parameter c_{ℓ_z}, linear fit and residuals. Data taken at 1 mm downstream of the TE for Case 1. 72
4.8 a) Spanwise coherence for $y/\delta = 0.55$. b) Empirical parameter c_{ℓ_z}, linear fit and residuals as a function of y/δ. Data taken at 1 mm downstream of the TE for Case 3. 72
4.9 a) Streamwise autocorrelation for Case 2, at $y/\delta = 0.39$. Symbols: experimental data, Solid line: curve fit. b) Empirical parameter c_{ℓ_x}, linear fit and residuals as a function of distance to the wall. 74
4.10 a) Streamwise autocorrelation for Case 1, at $y/\delta = 0.39$. Symbols: experimental data, Solid line: curve fit. b) Empirical parameter c_{ℓ_x} as a function of distance to the wall. 74
4.11 a) Streamwise autocorrelation for Case 3, at $y/\delta = 0.17$. Symbols: experimental data, Solid line: curve fit. b) Empirical parameter c_{ℓ_x} as a function of distance to the wall. 75
4.12 Longitudinal autospectrum as a function of wavenumber at selected points in the boundary layer for Case 2. Symbols: experimental data, dashed lines: Morris and Farassat model, solid lines: Pope's model. . 77
4.13 Turbulent kinetic energy and dissipation at selected points in the boundary layer for Case 2. Symbols: experimental data, dashed lines: Morris and Farassat model, solid lines: Pope's model. 77
4.14 Schematic of a long-span body divided by N subsections, adapted from Seo and Moon (2007) 79

5.1 Schematic of the CFD simulation domain, adapted from Jones (2013) 91
5.2 The computational grids used for all CFD calculations. 91

6.1 Schematic of the sampling domain used for RSNM acoustic calculations. 100

6.2 Computed acoustic power spectral density of a 15.24 cm chord NACA 0012 airfoil at a free stream velocity of 31.7 m/s ($Re_c \approx 333,000$), calculated with RSNM using three different grid resolutions. 101

6.3 Sampling domain study for a NACA 0012 airfoil at $\alpha = 0$ at $Re_c = 1.5e^6$. 102

6.4 Normalized mean velocity, turbulence kinetic energy and turbulence dissipation profiles for a NACA 0012 airfoil at $\alpha = 0$ at various Reynolds numbers. 104

6.5 Normalized boundary layer thickness, displacement thickness and momentum thickness for a 30.48 cm chord NACA 0012 airfoil at $\alpha = 0$ at various Reynolds numbers. 104

6.6 Normalized mean velocity, turbulent kinetic energy and turbulence dissipation profiles for the suction side of a 30.48 cm chord NACA 0012 airfoil at various angles of attack and at a Reynolds number of $Re_c = 1.5 \times 10^6$. 105

6.7 Normalized mean velocity, turbulent kinetic energy and turbulence dissipation profiles for the pressure side of a 30.48 cm chord NACA 0012 airfoil at various angles of attack and at a Reynolds number of $Re_c = 1.5 \times 10^6$. $x/c = 1$. 106

6.8 Normalized boundary layer thickness, displacement thickness and momentum thickness for a 30.48 cm chord NACA 0012 airfoil at various angles of attack and at a Reynolds number of $Re_c = 1.5 \times 10^6$. Circles: suction side. Squares: pressure side. $x/c = 1$. 106

6.9 Validation of CFD results versus experimental data of Brooks *et al.* (1989). Left) Displacement thickness normalized by chord as a function of Reynolds number. Right) Displacement thickness for various NACA-0012 airfoils at a flow velocity of $U_\infty = 71.3$ m/s at various angles of attack, normalized by displacement thickness at zero angle of attack. $x/c = 0.0043$ and $x/c = 0.0057$. 107

6.10 Mean velocity, turbulent kinetic and dissipation profiles for the suction side of a 40 cm chord NACA 0012 airfoil at a Reynolds numbers of $Re = 1.500.000$. Symbols are experimental data from Herr and Kamruzzaman (2013), solid lines are RANS CFD data. Colors blue, red and green represent angles of attack of 0, 4 and 6 degrees, respectively. $x/c = 1.0038$. 108

6.11 Normalized mean velocity, turbulence kinetic energy and turbulence dissipation profiles for the suction side of a DU 96-180 airfoil at various Reynolds numbers. Solid lines: AoA=3. Dashed lines: AoA=7. $x/c = 1$. 109

6.12 Normalized mean velocity, turbulence kinetic energy and turbulence dissipation profiles for the pressure side of a DU 96-180 airfoil at various Reynolds numbers. Solid lines: AoA=3. Dashed lines: AoA=7. $x/c = 1$. 110

6.13 Integral boundary layer parameters for a DU 96-180 airfoil at various Reynolds numbers. Blue: δ/c, red: δ^*/c, yellow: θ/c. Circles: suction side, squares: pressure side. Experimental data suction side: $+$, experimental data pressure side: $*$. $x/c = 0.0021$. (Devenport *et al.* 2010). 111

6.14 Mean velocity and turbulence intensity profiles for a DU 96-180 airfoil at $R_e = 3.14 \times 10^6$ at $\alpha = 7°$. Symbols: experimental data from (Devenport *et al.* 2010). Solid lines: CFD results. $x/c = 0.0021$. . . . 112

6.15 Boundary layer parameters for The FP12 airfoil at $R_e \approx 5 \times 10^5$ at $\alpha = 0°$ and percentage error. Experimental data taken from Moreau *et al.* (2011) ($x/c = 0.003$) and Chapter 3 ($x/c = 0.00083$). 113

6.16 Mean velocity, turbulence kinetic energy and dissipation profiles for the FP12 airfoil at $R_e \approx 5 \times 10^5$ at $\alpha = 0°$. Blue: experimental data from Moreau *et al.* (2011) at $x/c = 0.0030$. Red: experimental data from Chapter 3 at $x/c = 0.0008$. Yellow: experimental data from Chapter 3 at $x/c = 0.0042$. Solid lines: CFD results at $x/c = 0$. . . . 114

6.17 Acoustic predictions (solid lines) and experimental data of Brooks et al.(1989) for a NACA 0012 airfoil at $\alpha = o$. 125

6.18 Acoustic predictions (solid lines) and experimental data of Brooks et al.(1989) for a NACA 0012 airfoil at $\alpha = o$. 126

6.19 Acoustic predictions (solid lines) and experimental data of Brooks et al.(1989) for a NACA 0012 airfoil at $\alpha = o$. 127

6.20 Acoustic predictions for RSNM baseline (solid lines) and experimental data of Brooks et al.(1989) for a NACA 0012 airfoil at various angles of attack. 128

6.21 Acoustic predictions for RSNM Mod 3 (solid lines) and experimental data of Brooks et al.(1989) for a NACA 0012 airfoil at various angles of attack. 128

6.22 Acoustic predictions for RSNM Mod. 4 (solid lines) and experimental data of Brooks et al.(1989) for a NACA 0012 airfoil at various angles of attack. 129
6.23 Acoustic predictions for RSNM Mod. 5 (solid lines) and experimental data of Brooks et al.(1989) for a NACA 0012 airfoil at various angles of attack. 129
6.24 Acoustic predictions for RSNM Mod. 6 (solid lines) and experimental data of Brooks et al.(1989) for a NACA 0012 airfoil at various angles of attack. 130
6.25 Acoustic predictions for RSNM Mod. 7 (solid lines) and experimental data of Brooks et al.(1989) for a NACA 0012 airfoil at various angles of attack. 130
6.26 Acoustic results for a 91.40 cm chord DU-96-180 airfoil. Symbols: Experimental data of Devenport *et al.* (2010). Solid lines: RSNM at $\alpha = 3°$. Dashed lines: RSNM at $\alpha = 7°$. Red: 28 m/s. Blue: 42 m/s. Black: 58 m/s. 131
6.27 Acoustic results for a 30 cm chord DU-96-180 airfoil at $U_\infty = 40m/s$. $\alpha = 4°$. Symbols: Experimental data of Herr and Kamruzzaman (2013). Solid lines: RSNM predictions 132
6.28 Acoustic power spectral density for the FP12 airfoil at $R_e \approx 5 \times 10^5$ at $\alpha = 0°$. Symbols: experimental data from Moreau *et al.* (2011). Solid lines: RSNM predictions. 132
6.29 Length scale $L = c_\ell k^{3/2}/\epsilon$ for Case 1 (FP12 airfoil) at $R_e \approx 5 \times 10^5$ at $\alpha = 0°$. Symbols: experimental data, $c_\ell = 1$. Solid lines: RANS. . 133
6.30 Effects of changing the length scale on the acoustic predictions of RSNM for the FP12 airfoil at $R_e \approx 5 \times 10^5$ at $\alpha = 0°$. Symbols: experimental data. Solid lines: RSNM. 133
6.31 Effects of using experimental data as input to RSNM in the noise predictions for the FP12 airfoil at $R_e \approx 5 \times 10^5$ at $\alpha = 0°$. Symbols: experimental data. Solid lines: RSNM. 134
6.32 Experimental spectrum compared to baseline Gaussian model using experimental data as input at selected points in the boundary layer. The scaled spectrum $E_s = E/(\epsilon\nu^5)^{(1/4)}$. Solid lines: experimental data. Dashed lines: Gaussian spectrum+50 dB. 134

A.1 Wall-normal coherence at various wall normal distances for Case 2. Dots are experimental data, solid line is a Gaussian curve fit. $x/c = 1.0033$. 154

A.2 WallNormal coherence at various wall normal distances for Case 1. Dots are experimental data, solid line is an exponential curve fit. $x/c = 1.0033$. 155
A.3 WallNormal coherence at various wall normal distances for the Case 3. Dots are experimental data, solid line is an exponential curve fit. $x/c = 1.0033$. 155
A.4 Spanwise coherence at various wall normal distances for Case 2. Dots are experimental data, solid line is a Gaussian curve fit. $x/c = 1.0033$. 156
A.5 Spanwise coherence at various wall normal distances for Case 1. Dots are experimental data, solid line is a Gaussian curve fit. $x/c = 1.0033$. 157
A.6 Spanwise coherence at various wall normal distances for Case 3. Dots are experimental data, solid line is a Gaussian curve fit. $x/c = 1.0033$. 157

B.1 Schematic of a long-span body divided by N subsections, adapted from Seo and Moon (2007) 160

List of Tables

2.1 Summary of experimental uncertainties. 29

3.1 Boundary layer parameters for all cases. 36

4.1 Gavin's SAM model parameters 67
4.2 Curve fit parameters for spatial component of coherence function . . 73

5.1 SST $k-\omega$ model constants 88
5.2 Computational fluid dynamic boundary conditions. 89
5.3 Grid properties 90
5.4 Grid properties or a NACA-0012 airfoil at $Re = 1.5 \times 10^6$ 94
5.5 Grid properties for a NACA-0012 airfoil at $Re = 4 \times 10^6$ 95
5.6 Numerical and experimental displacement thickness δ^* and momentum thickness θ_s, measured at the 1.3 mm downstream of the trailing edge, and drag coefficient C_d, for the NACA-0012 airfoil with a chord based Reynolds number of $Re_c = 1.5 \times 10^6$ and angle of attack of $AoA = 0$. The symbols f_e and f_m stand for exact value (asymptotic value) and measured value. 95
5.7 Order of accuracy and Grid Convergence Index (GCI) for the 30.48 cm chord NACA-0012 airfoil at $Re = 1.5 \times 10^6$. 95
5.8 Grid properties DU-96-180 95
5.9 Numerical and experimental displacement thickness δ^*, momentum thickness θ_s, recorded at 1.9 mm downstream of the trailing edge, and drag coefficient C_d, for the DU 96-180 airfoil, with a chord based Reynolds number of $Re_c = 3,13 \times 10^6$ and angle of attack of $AoA = 7$. The symbols f_e and f_m stand for exact value (asymptotic value) and measured value (Devenport *et al.* 2010). Subscripts s and p denote suction side and pressure side, respectively. 95

5.10 Order of accuracy and Grid Convergence Index (GCI) for the Du96 airfoil. Subscripts s and p denote suction side and pressure side, respectively 96
5.11 Grid properties for the FP-12 airfoil 96
5.12 Boundary layer parameters for the FP-12 airfoil at 0.7 mm downstream of the trailing edge. The symbols f_e and f_m stand for exact value (asymptotic value) and measured value (Moreau *et al.* 2011). . 96
5.13 Order of accuracy and Grid Convergence Index (GCI) for the FP-12 airfoil. 96

6.1 Boundary layer parameters for a NACA 0012 airfoil at various operating conditions. τ_ω obtained at the trailing edge from CFD. Pressure gradient obtained between $0.95c \leq x < c$. Results for the suction side. 103
6.2 Boundary layer parameters for the suction side of a DU-96-180 airfoil at various operating conditions. τ_ω obtained at the trailing edge from CFD. Pressure gradient obtained between $0.95c \leq x < c$. Results for the suction side. 105
6.3 RSNM variations 124

Chapter 1

Introduction

When an airfoil is immersed in an undisturbed flow, a boundary layer is created over the surface of the airfoil and a wake is produced downstream. Flow turbulence is produced in the boundary layer, which generates pressure fluctuations in the fluid. When these pressure fluctuations reach the sharp trailing edge (TE), they encounter an impedance discontinuity, which scatters them as sound waves, radiating noise to the far field. This phenomenon is called trailing edge noise, and it occurs in many engineering applications such as wind turbines, aircraft, submarines, fans and turbo-machinery in general. All these applications generally operate in low Mach number, high Reynolds Number flows. Under these conditions, TE noise is one of the dominant mechanisms of airfoil self noise (Brooks *et al.* 1989).

A reduction in noise emissions is required by environmental regulations in the case of wind turbines and aircraft, for commercial advantages in the case of air conditioning units and other domestic appliances, and for tactical advantage in military applications such as submarines, helicopters and unmanned aerial vehicles (UAVs).

Wind turbine noise is one of the major hindrances for the widespread use of wind energy (Oerlemans *et al.* 2008). TE noise has been identified as the main contributor to wind turbine noise in the absence of inflow turbulence (Migliore and Oerlemans 2004).

TE noise is also a major concern for the aviation industry. Strict noise regulations limit the operation hours of airports and the construction of new airfields, and NASA has set a long term noise reduction goal of 20 dB for commercial aircraft (Lockard and Lilley 2004). There is evidence on the association between exposure to road traffic and aircraft noise and hypertension and ischaemic heart disease, and exposure

to aircraft noise has been shown to increase the risk of high blood pressure (WHO 2011). The Advisory Council for Aeronautics research in Europe ACARE has set a goal of reducing the perceived noise levels of flying aircraft by 65% relative to the capabilities of typical new aircraft in 2000 by the year 2050 (Kallas *et al.* 2011). Since the introduction of high bypass ratio jet engines in commercial aircraft, airframe noise has become comparable to engine noise for aircraft on approach. Hence, any further reduction in overall aircraft noise will require airframe noise to be addressed, and if the long term 20 dB reduction set by NASA is to be achieved, TE noise in particular will have to be reduced (Arguelles *et al.* 2001).

The aim of this research is to provide a method for predicting trailing edge noise that can be used to design quiet airfoils. Reynolds-Averaged Navier Stokes (RANS) simulations are routinely used for aerodynamic design and optimization, therefore, a RANS-based TE-noise prediction method would be greatly beneficial, allowing acoustic optimization of airfoils to be performed at the design stage. RANS is better suited to this task than Large Eddy Simulation (LES), due to the large computational demands of the latter, resulting in very long solution times. This thesis presents a RANS-based Statistical Noise Model (RSNM), which combines a statistical model of the turbulent velocity cross-spectrum with the mean flow data obtained form a RANS flow solution. The noise radiated to the far field is calculated by means of the acoustic analogy of Ffowcs Williams and Hall (1970). Various forms of the turbulent velocity cross-spectrum are investigated and the method is applied to a variety of airfoil shapes at a range of operating conditions, and validated against experimental data from the literature.

1.1 Literature review

The introduction of the jet engine into the aviation industry created a need to minimize the noise produced by aircraft. Lighthill (1952) was the first to provide a theory for noise produced aerodynamically; that is, produced by the airflow itself, and not by the action of vibrating solid bodies. He combined the Navier-Stokes equations and the continuity equation to produce an inhomogeneous wave equation, where the non-linear terms are grouped on one side of the equation and can be considered as sound sources (Lighthill's stress tensor). This is known as Lighthill's acoustic analogy. The problem can be modelled as a volume distribution of quadrupole sources, and dimensional analysis shows that the acoustic power output is proportional to the eighth power of the flow velocity (Lighthill 1952). Curle (1955) provided an

extension of Lighthill's theory to account for the presence of solid boundaries, and showed that sound radiation in the presence of solid boundaries in a turbulent flow is equivalent to a distribution of dipoles, which at low Reynolds numbers radiate much more intensely than Lighthill's quadrupoles, with an intensity proportional to the sixth power of the flow velocity.

Important contributions to Lighthill's theory where made by Ffowcs Williams and Hawkings (1969), who extended it to the presence of solid boundaries in arbitrary motion, which results in an additional distribution of surface sources of a monopole character.

Further extension of Lighthill's theory was provided by Ffowcs Williams and Hall (1970), who found an analytical solution to the diffraction problem of a scattering half plane. Ffowcs Williams and Hall (1970) showed that in the presence of a sharp edge, scattering and diffraction phenomena caused the sources to be made more efficient again, radiating with an intensity proportional to the fifth power of the Mach number. Thus TE noise is more efficient than Lighthill's distribution of quadrupoles or Curle's dipole surface distribution.

Amiet (1976), Chandiramani (1974) and Chase (1972) provided further theoretical developments, formulating the problem of trailing edge noise in terms of the scattering of the surface pressure spectrum immediately upstream of the trailing edge. Howe (1978) provided a unified view of the theory, incorporating the effect of mean motion. Later, Roger and Moreau (2005) extended the theory of Amiet (1975) by providing a correction for leading-edge back-scattering, as Amiet (1975) method failed to obtain the correct directivity patter due to the truncation of the surface integral at the leading edge. Moreau and Roger (2009) validated the model presented in Roger and Moreau (2005) by comparing the predicted noise spectra and directivity with analitical and experimental results, confirming that the model predicts the correct directivity pattern, as well as the correct levels and spectral shape of the radiated noise, provided that the model is fed with accurate correlation lengths and wall-pressure statistics. Because wall pressure fluctuations are more amenable to experimental measurements, this approach has been extensively researched and used.

Trailing edge noise prediction methods can be classified in three broad categories: direct, hybrid and empirical. Each of these approaches has advantages and drawbacks, which will be discussed in the following sections.

1.1.1 Empirical methods

Empirical methods are based on a detailed observation of airfoil flow and noise experimental data, for a wide range of operating conditions . The sound field can then be related to properties like free stream velocity, angle of attack and boundary layer thickness. The most widely used empirical models were proposed by Schlinker and Amiet (1981), developed for predicting helicopter rotor noise; and the BPM (Brooks, Pope and Marcolini) model (Brooks *et al.* 1989), developed for the self-generated noise of an airfoil blade encountering smooth flow.

Empirical models for the surface pressure spectrum for zero-pressure gradient turbulent boundary layers have been developed by Chase (1972), Goody (2004) and Smol'Yakov and Tkachenko (1991) which can be used to calculate the far field sound spectrum by means of the theory of Amiet. Using these methods to calculate the noise spectrum of sharp edged struts at low Reynolds numbers, Moreau *et al.* (2011) found that they showed some agreement with experimental data above 2 kHz. Below this frequency however, the predicted noise levels were significantly less than the experimentally determined noise levels.

Empirical methods are attractive due to their simplicity and because they require very few input parameters; however, their range of application is limited to flow conditions similar to those of the original experiments used to develop them.

1.1.2 Direct methods

Direct methods are designed to calculate the fluid dynamics and acoustics in a single step. They do so by solving the compressible Navier Stokes equations using either Direct Numerical Simulation (DNS) or Large Eddy Simulation (LES). Both of these Computational Fluid Dynamics (CFD) tools have large computational demands, which are further complicated by the following particular features of TE noise problems:

- Noise predictions are required for an observer located in the far field. This calls for a large domain using high performance schemes with minimal numerical dispersion and diffusion, and carefully designed boundary conditions that avoid reflections as the acoustic waves reach the end of the finite domain.
- TE noise is broadband, which means very high spatial and temporal resolution is required to resolve the higher frequency waves, which have short

wavelengths.

- Acoustic waves have very small amplitudes compared with the mean flow, often several orders of magnitude smaller. This requires high-order numerical accuracy if both sound and flow are to be computed simultaneously (Wang *et al.* 2006).

In spite of these difficulties, some researchers have used direct methods for TE noise calculations. Because of its low Reynolds number limitation, DNS has mainly been used for fundamental studies of the airfoil self noise mechanisms via the direct calculation method;

Sandberg *et al.* (2008; 2009) conducted DNS on a NACA 0012 airfoil at a 5 degree angle of attack, for a Reynolds number based on the chord length of $Re = 50,000$, to investigate the self noise mechanisms and the validity of the classical theory of Amiet. They found a strong correlation between the surface pressure spectrum close to the TE on the pressure side and the sound field for an observer below the airfoil and a similar, but with opposite sign correlation for the suction side, suggesting a significant portion of the noise emanates from the TE. Another important finding was that the assumption of frozen turbulence (i.e. the rate of change of an eddy is small compared to its convection velocity and can be neglected) should be used with caution, as the turbulent boundary layer structure changes as it approaches the trailing edge, particularly in the presence of an adverse pressure gradient.

Another fundamental study was performed by Jones and Sandberg (2009), who conducted a DNS study for a NACA 0012 airfoil with a serrated trailing edge, finding that the serrations diminish the spanwise correlation of the vortical structures, hence reducing the associated tonal noise.

LES has been more widely used than DNS for direct noise calculations, due to its less stringent computational demands. Marsden *et al.* (2008) conducted direct TE noise calculations for a NACA 0012 airfoil at zero angle of attack for a Reynolds number of $Re = 500,000$. Good agreement with experimental data was observed. The simulations also showed that acoustic waves emanate from the leading edge due to the backscattering of waves generated at the TE.

Multi-time step multi-size mesh strategies (Gloerfelt and LeGarrec 2009) have made it possible to perform TE noise calculations using LES for a Reynolds number of up to 2.32×10^6 for a NACA 0012 at incidence angle of 2.5° with a truncated TE. Some discrepancies have been observed between the simulations and experimental results; particularly for the vortex shedding frequency, which was overestimated by

the simulation.

An alternative to traditional CFD methods is the Lattice Boltzmann method (LBM), which is an efficient and highly parallelizable approach for the simulation of fluid flows. The LBM solves the discrete Boltzmann equations in combination with a collision model to simulate a Newtonian fluid. The LBM is transient, and can capture flow characteristics such as flow separation, vortex shedding, and sound pressure waves from aeroacoustic sources. LBM has been successfully applied to calculate trailing edge noise by van der Velden *et al.* (2016), who concluded that the methodology was sufficiently accurate for trailing edge noise prediction, in particular for broadband noise. The computational cost, although smaller than for DNS, is still substantial, as van der Velden *et al.* (2016) reported a turn-around time of 730 CPU hours for a simulation of 0.1 physical seconds.

While direct methods provide a powerful tool for fundamental research and can provide great insight into airfoil self noise generating mechanisms, they are too computationally demanding even for today's high performance computers, making their use in industrial applications or in airfoil shape optimization impractical. As a result, hybrid methods have been designed to reduce the computational cost of aeroacoustic simulations. These methods are described in the following section.

1.1.3 Hybrid methods

Hybrid methods decouple the flow calculation from the sound calculation, as the latter can be done as a post processing step. This separation of generation and propagation processes makes the hybrid approach more efficient than the direct approach. A fundamental assumption needs to be made in order to make such a separation; namely the one way coupling of the flow and the sound field. This means that the flow is unaffected by the sound waves, an assumption that is valid for low Mach number, high Reynolds number turbulent flow (Wang *et al.* 2006). Hybrid methods make use CFD simulations to calculate the flow in the vicinity of the aerodynamic source region; hence calculating the acoustic source terms that are used as inputs in the aeroacoustic theory. Once the sound sources are known, the far field sound can be computed by means of numerical or integral methods. The difficulty lies in computing or modelling these sources accurately. When this is achieved, hybrid methods have been proven to be as accurate as direct methods (Khalighi *et al.* 2010) at only a fraction of the computational cost.

Time accurate flow solvers like DNS, LES or unsteady RANS (URANS) can com-

pute the sources directly, while a time averaged solution (RANS) can provide mean turbulent flow data to assemble the sources using stochastic or statistical modelling techniques. This section provides a review of the previous work done using these approaches.

1.1.3.1 Methods based on time accurate CFD

In theory, if the source terms in Lighthill based acoustic analogies are known, the far field sound can be obtained. It is tempting to use DNS to directly calculate the sound source terms, but the computational cost becomes prohibitive for Reynolds numbers of engineering relevance. Therefore LES is typically used to calculate the source terms (Terracol 2005, Marsden *et al.* 2007, Christophe *et al.* 2009). However, LES evaluation times are generally large, and in many aeroacoustic applications (such as TE noise) the presence of solid boundaries calls for very fine near-wall grid resolution in order to resolve small but dynamically important eddies. This stringent near wall grid resolution requirement limits the simulations to a very small span of the airfoil, introducing further uncertainty in the TE noise predictions for the full airfoil span, particularly at low frequencies, where the spanwise coherence of the turbulent fluctuations can be larger than what is feasible to include in the computational domain (Wang and Moin 2000, Christophe *et al.* 2009). Furthermore, the smaller scales of turbulence, responsible for the high frequency content, are either missing or inaccurate as a result of the subgrid-scale modelling (Wang *et al.* 2006). Nonetheless, LES is likely to become the method of choice for TE noise prediction as computer power increases. This is supported by the successful calculation of TE noise performed by many researchers such as Wang *et al.* (2006) and Marsden *et al.* (2007) using LES in combination with the Ffowcs Williams and Hall (1970). Christophe *et al.* (2009) used LES in conjunction with the theory of Curle (1955) to predict the noise generated by a segment of an automotive blade, showing good agreement for frequencies below 1000 Hz, but over-predicting the sound for higher frequencies.

LES has also been used to calculate the surface pressure spectrum near the TE, which is used to calculate the far field noise by the theory of Amiet (1975). Some examples of this approach include its application to airfoil self noise in the presence of TE blowing (Winkler *et al.* 2009), where air is injected to the boundary layer to modify its properties through a slot over the airfoil, and the previously mentioned work of Christophe *et al.* (2009).

Wolf *et al.* (2012) used compressible LES to obtain accurate wall-pressure data, which were used in the FWH acoustic analogy formulation to calculate the noise from a NACA 0012 airfoil at $Re_c = 408,000$ at angles of attack of 0 and 5 degrees. He obtained excellent agreement with the experimental data of Brooks *et al.* (1989).

In an effort to lower the computational demands of LES, hybrid LES/RANS approaches have been pursued. Generally, LES is used only in a very small domain about the source region, embedded in a larger domain treated with less expensive RANS. The RANS simulations are used as inflow and boundary conditions for the LES. This approach was successfully used by Terracol (2005) to calculate TE noise for a flat plate and a NACA 0012 airfoil, both having a blunt trailing edge, and by Wang and Moin (2000) for a bevelled edge flat strut at a chord Reynolds number of 2.15×10^6.

Unsteady RANS (URANS) provides the least detailed simulations. However, it is able to capture the larger flow structures and their associated sound, which makes it suitable for narrow band noise applications such as tonal noise associated with blunt trailing edge vortex shedding (Singer *et al.* 2000), but it is unsuitable for broadband noise calculations of the type under consideration in this project, as it is unable to capture the smaller structures responsible for the high frequency content of TE noise.

1.1.3.2 RANS based methods

Since turbulence is a random process, statistical quantities can be used to describe the flow without the excessive demands of instantaneous knowledge of all flow variables. These statistical quantities include temporal and spatial correlations, as well as length and time scales. However, sound generation and propagation is an inherently time-dependent phenomenon, so the time averaged information available from a RANS simulation is not sufficient by itself to perform noise calculations. To cope with this limitation, two different approaches based on statistical data provided by RANS have been developed; namely Stochastic Noise Generation and Statistical modelling of the turbulent sources.

1.1.3.3 Stochastic Noise Generation and Radiation (SNGR)

Rather than obtaining the sources from time accurate data, which would require the use of expensive DNS or LES, stochastic noise generation and radiation methods generate their own turbulence sources based on prescribed statistical information of the flow, which can be obtained by means of less expensive RANS simulations. The turbulence data can be generated as a sum of random Fourier modes (Karweit *et al.* 1991) or by spatially filtering white noise (Ewert 2008, Dieste and Gabard 2009). Both of these approaches assume homogeneous isotropic turbulence, but the effects of non-homogeneity and anisotropy can be included by using a Smirnov transformation (Smirnov *et al.* 2001). The pressure fluctuations generated by the synthetic turbulence field can then be sampled on a permeable (Kirchhoff) surface surrounding the turbulent region and propagated to the far field by solving the Linearized Euler Equations (LEE) or the Acoustic Perturbation Equations (APE) (Ewert *et al.* 2009).

The Stochastic Noise Generation and Radiation (SNGR) approach has been successfully applied to a variety of aerodynamic noise problems, such as TE noise (Bauer and Zeibig 2006, Ewert 2008, Ewert *et al.* 2009, Dobrzynski *et al.* 2009, Casalino and Barbarino 2011), landing gear noise (Dobrzynski *et al.* 2009), jet and cavity noise (Mesbah 2006). This wide range of applicability makes SNGR very powerful, but its disadvantage lies in the rather large computer resources required for generation and storage of the turbulence time data, which are further increased when numerical methods are used to propagate the sound to the far field.

1.1.3.4 Surface pressure approach

Most statistical methods require a model of the surface pressure spectrum, which can be used to calculate the far field sound by means of the theory of Amiet (1975) or (Chandiramani 1974). There are a number of ways to estimate the wall pressure spectrum, and these are described in the following paragraphs.

Kamruzzaman *et al.* (2007) proposed a model for the wall pressure spectrum based on a spectral solution to the Poisson equation and a Von Karman turbulent kinetic energy spectrum. Of particular importance in this model is the accurate determination of the vertical integral length scale, which can be obtained from local flow statistics provided by a RANS simulation by assuming isotropic turbulence. The effects of anisotropy can be taken into account by means of an anisotropy factor,

without the need for an anisotropic turbulence model (Kamruzzaman *et al.* 2008). This method predicts the correct spectral shape, but has problems predicting the correct sound pressure levels.

Another method for predicting surface pressure spectra was proposed by Lee *et al.* (2005), which uses RANS to obtain the time-averaged flow field characteristics and a spectral correlation model for the prediction of the frequency spectrum of the wall pressure fluctuations. The model works well for equilibrium flows, but underpredicts the middle and higher frequency range of the spectrum for non equilibrium flows.

Another method used to predict the surface pressure spectrum via a RANS solution was proposed by Peltier and Hambric (2007). The method requires a model for the velocity cross correlation function based on a RANS solution and the selection of an appropriate Green's function. Comparison of the wall pressure spectra predicted with this method and experimental data is favorable for the low frequency range, but not good for intermediate and high frequencies.

The surface pressure spectrum can also be obtained from time-resolved Tomographic Particle Image Velocimetry (PIV). Pröbsting *et al.* (2015) showed the feasibility of this approach and obtained good agreement with experimental data for a limited frequency range; however, they also note that hardware limitations, together with the fine sampling interval required, limit the maximum accessible flow velocity and measurement volume, hence limiting the application of the method to relatively low Reynolds numbers.

The surface pressure spectrum can also be measured using an array of pinhole microphones distributed in the streamwise and spanwise direction on the surface of the airfoil. This approach was used by Fischer *et al.* (2015) to calculate the far field noise of a NACA64-618t airfoil in combination with the models of Roger and Moreau (2005) and Howe (1978). The predictions showed excellent agreement with experimental measurements in a frequency range of 500-2000 Hz. Using experimental surface pressure data as input for the noise prediction method is a significant limitation, as these data will not be available for an airfoil at the design stage. Analytical or empirical models for the surface pressure spectrum can be used instead, which can introduce additional errors and uncertainties.

Glegg *et al.* (2008) showed that the unsteady velocity fluctuations in a turbulent boundary layer (TBL) flow can be related to vortex sheet strength as a function of distance to the wall. The vortex sheet strength can be calculated by numerically

inverting a turbulent kinetic energy (TKE) profile obtained from a RANS calculation. The surface pressure spectrum can be obtained from the vortex sheet strength; hence the sound radiated from the TE can be computed.

Catlett *et al.* (2014) proposed a modified version of the Goody (2004) model for adverse pressure gradient flows, based on experimental measurements of the pressure spectrum. The model introduces eight additional empirical coefficients that were tuned to fit the experimental data.

The previously discussed methods use the assumption of spanwise and chordwise homogeneous turbulence in their derivation. This assumption is unlikely to hold in many airfoil configurations, in particular when sinusoidal variations or serrations are used in the trailing edge.

1.1.3.5 Methods based on statistical models for the two-point velocity correlation

If the form of the two-point velocity correlation in the boundary layer close to the trailing edge is known, an acoustic analogy can be used to calculate the noise radiated to the far field. Surprisingly, this approach has not been pursued by many researchers in the past. However, a similar approach has been applied to the prediction of jet noise with some success.

A model for high speed jet fine scale (high frequency) noise, was developed by Tam and Auriault (1999), using adjoint harmonic Greens functions to calculate the intensity spectra in the far field by solving the linearized Euler equations. They used a RANS solution ($k - \epsilon$ model) to provide information for the fine scale turbulence model, which is based on a modelled cross correlation function of the noise sources. Three empirical constants arise in the model, which are calculated from best fit to experimental measurements. Tam and Auriault (1999) obtained good agreement with experimental data, which makes this model a promising tool to apply to other turbulent problems, such as TE noise predictions.

A similar approach to Tam and Auriault (1999) was taken by Morris and Farassat (2002), who also used a RANS solution and a modelled correlation function with a Gaussian form to calculate the far field sound for jet noise with some success. Their approach was based on Lighthill's analogy rather than Euler's linearized equations. The results of both approaches are shown to be equivalent at 90 degrees of the jet axis if similar statistics for the turbulent sources are considered (Morris and Farassat

2002); however, this equivalence does not hold at other angles to the jet axis.

1.1.4 Available models for the velocity two-point velocity correlation

There have been numerous attempts to model the two-point correlation function in jets. The models usually assume isotropic turbulence, such as those proposed by Batchelor (1953) and Ribner (1969), or assume the turbulence is axisymmetric (Goldstein and Rosenbaum 1973, Khavaran 1999). Axisymmetric models tend to perform better than isotropic models for jet noise applications (Bridges and Podboy 1999).

Considerable effort has also been made to measure the two-point correlation function in jets using a range of techniques such as hot wire anemometry (Morris and Zaman 2010), simultaneous Particle Image Velocimetry (PIV) and Laser Doppler Velocimetry (LDV) (Kerherv *et al.* 2010).

Measurements of the four-dimensional two-point correlation tensor of a fully developed airfoil wake of a NACA 0012 airfoil were performed by Devenport *et al.* (2001). They also developed a simple technique for extrapolating the two-point correlation tensor function from single-point Reynolds stress data, which captures many of the gross features of the correlations.

Similarly, there have been programs to measure two-point statistics in wall bounded flows, including channel flows (Quadrio and Luchini 2003, Ganapathisubramani *et al.* 2005) zero pressure gradient (ZPG) turbulent boundary layers (Favre *et al.* 1957, Tritton 1967, Gavin 2002, Tutkun *et al.* 2009) and turbulent boundary layers subjected to pressure gradients (Harun 2012).

However, there have not been many attempts to model the two-point space-time correlation for boundary layers analytically. Phillips (2000) developed a model of the velocity cross correlation based on channel flow DNS data of Kim *et al.* (1987). The model is a function of spatial separation, a length scale, the Reynolds stresses and mean flow velocity. They concluded that the model should be applicable to turbulent boundary layers as well as for channel flow.

Gavin (2002) proposed another model for ZPG turbulent boundary layers based on hot wire measurements. He modelled the correlation volume as an ellipsoid inclined at an angle θ to the wall. He provided values for the inclination angle and stretching ratio between the major and minor axes of the ellipsoid, based on best fit to his

experimental data. The model requires a convection velocity and the specification of a correlation length.

To the author's best knowledge, there are no models of the two-point velocity correlation for turbulent boundary layers subject to adverse pressure gradients.

The models proposed by Phillips (2000) and Gavin (2002) could potentially be linked to a RANS-CFD solution in order to obtain the necessary flow data, and used with the theory of FW-Hall to calculate the noise radiated to the far field. It remains to be seen if these models are adequate in the presence of pressure gradients.

1.2 Summary

RANS-based TE noise prediction methods can provide a good balance between accuracy and fast turn-over times. To date, RANS-based TE-noise prediction methods have made use of the surface pressure spectrum approach, but no attempt has been made to combine RANS-CFD with the FW-Hall diffraction theory. Such a method would require a model of the velocity two-point correlation in the vicinity of the trailing edge. Models of the velocity two-point correlation have been developed for jet flows and ZPG boundary layers, but it is unclear if these models are suitable in the presence of adverse pressure gradients. The literature on velocity two-point correlations in APG boundary layers is scarce (Harun 2012), making it difficult to validate these models or to develop new ones.

1.3 Aims and objectives

The overall aim of this research is to investigate and develop a trailing edge noise prediction method that combines RANS turbulent flow solutions with statistical models of the turbulent flow field. To achieve this aim, the following specific objectives will be pursued:

1. To implement a RANS-based trailing edge noise prediction methodology.
2. To experimentally investigate the turbulent single and two-point statistics in ZPG and APG boundary layers as well as the near wakes of airfoils.
3. To determine semi-empirical models of boundary layer and near wake turbulent statistics that can be linked to the RANS numerical data.

4. To validate the noise prediction methodology using the new turbulent statistical models to predict noise from a variety of airfoil shapes for the available flow data in the literature.

1.4 Contributions to the field

The main contributions arising from this research are:

1. A new, validated computationally efficient RANS-based TE-noise prediction method, which includes an empirical model for the turbulent velocity cross-spectrum in turbulent boundary layers that was developed from experimental data obtained during this research.

2. A detailed investigation of single-point statistics and two-point statistics for ZPG and APG turbulent boundary layers and the near wake of airfoils, including mean and turbulent velocity profiles, probability density functions (PDF's) of turbulent velocity, turbulent velocity spectra and turbulent velocity coherence function, that provides new insight into the flow physics and noise production mechanisms.

Chapter 2 describes the equipment and configuration used in the experiments, including the wind tunnel, airfoil models, traverse mechanism and CTA anemometer. It provides a brief background on hot wire anemometry, and a detailed error analysis of the experimental measurements.

Chapter 3 presents the results of the experimental investigation of the flow near the trailing edge of two sharped edged struts. It compares the present results to the literature, using a flat plate boundary layer as a validation case, and then compares this case to two other cases at different adverse pressure gradients. Results are presented for mean and RMS velocity profiles, probability density functions, third and fourth order moments, spectral density, two-point correlations and coherence functions.

Chapter 4 develops the noise prediction method RSNM and describes its RANS implementation. It also presents various models for the velocity cross-spectrum, which are incorporated into RSNM. It also develops a cross-spectrum model based on the results of Chapter 3, which is used within the RSNM framework to perform acoustic calculations in Chapter 6. The cross-spectrum is separated in a frequency dependent function and a spatial separation function, and models for each function

are developed and compared to experimental data. Further, this chapter presents a methodology to correct the 2D simulations to account for the real finite span of the airfoil.

Chapter 5 describes the computational approach used to generate the flow information required to perform noise calculations. It includes a description of the Reynolds Average Navier Stokes (RANS) equations and the SST $k-\omega$ turbulence model, followed by a description of the numerical settings and grids used. It also presents a grid refinement study for the three airfoil geometries used in this research, namely a NACA-0012, a DU-96-180 and an FP-12.

Chapter 6 presents the acoustic predictions obtained from RSNM for a NACA 0012 airfoil,a DU-96-180 airfoil and the FP12 airfoil. It compares the predictions to experimental data from the literature at a range of operating conditions. It also presents the validation of the CFD simulations used as input for the noise prediction model.

Finally, conclusions and future work are presented in Chapter 7.

1.5 Publications arising from this thesis

The publications arising from this thesis are as follows:

Doolan, C.J., Albarracin Gonzalez, C., Hansen, C.H. Statistical estimation of turbulent trailing edge noise. In: Proceedings of the 20th International Congress on Acoustics, 2327 August 2010, Sydney, Australia.

Albarracin, C., Doolan, C., Hansen, C., Brooks, L. Turbulent trailing edge noise estimation using a RANS-based statistical noise model. In: Proceedings of Acoustics 2011, 2-4 November, Gold Coast, Australia.

Albarracin, C., Doolan, C., Jones, R., Hansen, C., Brooks, L., Teubner, M. A RANS-based statistical noise model for trailing edge noise. In: Proceeding of the 18th AIAA/CEAS Aeroacoustics Conference, 4-6 June 2012, Colorado Springs, CO, USA.

Albarracin, C.A and Doolan, C.J. Semi-empirical turbulence models suitable for trailing edge noise predictions. Ninth International Symposium in Turbulence and Shear Flow Phenomena (TSFP-9), June 30th-July 3rd, 2015, Melbourne, Australia.

Chapter 2

Experimental methods

This chapter presents the equipment and configuration used in the experiments, including the wind tunnel, airfoil models, traverse mechanism and CTA anemometer. It provides a brief background on hot wire anemometry, describing the limitations of the method and the process of calibration. A detailed error analysis concludes the chapter.

2.1 Experimental setup

Experiments were performed in an open-jet low-speed wind tunnel at the University of Adelaide. The tunnel has a rectangular contraction outlet of dimensions 690 mm × 360 mm. The jet velocity was set at 6.4 m/s and the measured free stream turbulence intensity was $Ti = 0.65\%$.

The models were positioned such that the leading edge coincided with the exit plane of the contraction outlet, and extension plates were fitted to the contraction outlet to ensure the trailing edge of the model was well within the potential core of the jet and measurements were not influenced by the nozzle lip shear layers. A diagram of the experimental setup is shown in Figure 2.1, with a coordinate system centered at the mid-span of the trailing edge and coinciding with the airfoil chord line. x, y, z are the streamwise, wall-normal and spanwise directions respectively. U is the mean velocity in the streamwise direction and u' is its fluctuating component. A picture of the experimental setup is shown in Figure 2.2. A pitot probe was positioned at $\mathbf{x} = (-1200, 84, 0)$ mm. The pitot probe was connected to a 10 Torr. baratron unit, which was in turn connected to the data acquisition system and sampled at 2 kHz

to monitor the free stream velocity.

Two TSI 1210-T1.5 single wire probes with wire length of $L = 1.27\,\text{mm}$ and a wire diameter of $d = 3.81\,\mu\text{m}$ ($L/d \approx 400$) were used, and were operated using an IFA 100 constant temperature anemometer, with an overheat ratio of 1.8. The reference ("fixed") hot wire probe was mounted on a manual traverse with an accuracy of 0.01 mm and was positioned at the center span ($z = 0$) and desired y location before each measurement. The reference probe positions ranged from $y/\delta = 0$ to $y/\delta = 0.8$, where δ is the boundary layer thickness at the TE. The moving hot wire probe was mounted on a TSI 9400 2-axes traverse system, with a positional accuracy of 0.01 mm. The TSI traverse was controlled using the TSI-9400 traverse controller, which was connected to a computer via the RS-232 port. When the moving probe was traversed in the wall-normal direction, the reference probe was always the one closer to the wall. When the moving probe was traversed in the spanwise direction, the reference probe was always located at the mid-span point.

Data were acquired using a 2 bit NI-PXI4472 data acquisition card, at a sample rate of 20 kHz for 8 seconds. A low-pass filter with a cut-off frequency of 8 kHz was applied to the data prior to digitization to avoid aliasing.

2.2 Airfoil models

The models used in the experiment (Figures 2.3(a) and 2.3(b)) were two 1.2 m chord struts of 25 mm thickness. The first one, FP-12, has a circular leading edge and a wedge-shaped trailing edge with an apex angle of 12 degrees. The second strut, FP-12-B, has an elliptical leading edge with an aspect ratio of $x/y = 3.2$ and an asymmetrical wedge-shaped trailing edge with an apex angle of 12 degrees. For both models the trailing edge thickness is 1 mm, and the boundary layer was tripped on both sides by a 0.5 mm thick turbulator strip placed at 10% chord. The Reynolds number based on chord was $Re_c = U_\infty c/\nu = 512,000$.

2.3 Aligning the traverse

The traverse was aligned to the trailing edge by attaching a laser pointer to the probe holder, traversing it in all directions and measuring the drift of the laser from the desired path. This involved an iterative process described below.

Wall-normal alignment. To ensure the vertical alignment of the traverse, the laser was placed at 100 mm above the airfoil and aimed directly at the flat surface of the airfoil, ensuring that the reflected beam came back to the source. The fact that the airfoil was made of clear perspex allowed an extra check of the alignment by ensuring the refracted beam to be perpendicular to the surface (see Figures 2.4(a) and 2.4(b)). Then a sheet of graph paper was fixed to the surface of the airfoil and the laser pointer was traversed vertically 100 mm. If there was a shift in the position of the beam on the graph paper, the traverse was adjusted accordingly and the whole process was repeated until no drift was detectable (see Figures 2.4(c) and 2.4(d)).

Spanwise alignment. The traverse was aligned to the trailing edge by aiming the laser beam vertically to a position 1 mm upstream from the trailing edge. The laser beam was then traversed 100 mm along the trailing edge and the displacement of the beam from the edge was measured. If the distance from the edge drifted, the traverse was realigned and the process was repeated until no drift was detectable.

Streamwise adjustment. When measurements involving different streamwise positions were required, the traverse had to be rotated 90 degrees and realigned. The procedure used was similar to the spanwise alignment procedure.

Alignment error. Considering the width of the laser beam (0.5 mm approx.), the accuracy of the graph paper (1 mm^2 grid), and the fact that the alignment process was performed using the naked eye, it is safe to assume that the minimum drift one could detect would be 0.5 mm. Since the laser was traversed over 100 mm, the resulting alignment error is $e = 0.5\%$.

2.4 Hot wire anemometry

Hot wire anemometry makes use of the heat transfer between a heated element (the wire) and the surrounding fluid. When the heated wire is placed in a moving fluid, heat is transferred to the fluid. The magnitude of the heat transfer is dependent on the flow velocity, due to convection. The constant temperature anemometer (CTA) works by providing a variable current to the wire to keep its temperature constant. By calibrating the anemometer against a set of known velocities, a transfer function can be obtained between the flow velocity and the output voltage E (see Figure 2.4).

To modulate the current through the probe, the CTA uses a feedback circuit based

on the Wheatstone Bridge, as shown in Figure 2.4. As the flow conditions change, the error voltage $e_2 - e_1$ is proportional to the change in wire resistance. These voltages are the input to the amplifier G. The amplifier provides a current i, which is inversely proportional to the change in resistance of the sensing element R_w. By applying this current to the top of the bridge, the resistance of the sensing element is brought back to its original value, and in turn the wire temperature is also restored to its original value.

2.4.1 Frequency response of the anemometer

Before calibration, the frequency response of the anemometer was set by performing a square wave test. The square wave test consists of applying a square wave voltage signal (a perturbation) to the bridge and observing the time the feedback circuit requires to balance the bridge (return to steady state). The probe must be exposed to the highest velocity expected in the experiment during the test, to ensure the response is sufficiently rapid to resolve the fastest fluctuations encountered in the experiment. The signal is monitored with an oscilloscope and the cable trim (either a capacitor or inductor in the bridge) can be adjusted until the correct wave form is obtained in the oscilloscope. The correct wave form is shown in Figure 2.5. The response must be a smooth curve with an undershoot of 15% of its peak amplitude (Bruun 1995). The frequency response of the anemometer can be determined by:

$$f_c = \frac{1}{1.3t_c} \tag{2.1}$$

where t_c is the time required for curve to decay to 3% of its peak amplitude. The frequency response was adjusted before each set of measurements. The frequency response varied for each set of measurements, but was never below 30 kHz, which is sufficient to resolve the highest frequencies encountered in the current experiments, as the signal reached the noise floor below 8 kHz.

2.4.2 Calibration

The probes were calibrated using a TSI calibrator, model 112700 . The calibrator has a circular nozzle that produces a jet of known velocity and very low turbulence intensity. The probes were placed in the potential core of the jet and exposed to a set of known velocities ranging from zero to 10 m/s. A table was constructed with the measured voltage and the known velocities, and a fifth degree polynomial was

fitted through the points to obtain the calibration curve. The probes were calibrated before and after each set of measurements and the calibration curves were compared to each other. Figure 2.6 shows an example of the calibration curves before and after the measurements. The points can be seen to lie on a single curve.

2.5 Error analysis

There are a number of uncertainties present in an experiment. In the case of hot wire anemometry, errors can be introduced through a number of mechanisms, which are discussed in the following paragraphs.

Spatial resolution errors are the result of spatial non-uniformity of the flow along the wire length. This can occur due to a velocity gradient across the wire, such as when the wire is placed perpendicular to the wall in a boundary layer flow, or when the length of the wire is not small compared to the fine scales of the turbulence. For the first case, errors have been estimated to be of the order of -4.3% for $\bar{U}$ and -5.8% for u' for a probe with a wire length-to-diameter ratio of $\ell/d = 400$ and an overheat ratio of 1.8 (Gessner and Moller 1971). These conditions are similar to the present experiments. These errors become negligible if the wire is placed parallel to the wall, as the velocity gradient over the diameter of the wire ($d = 5\mu$m) is negligible. In the present experiments, the wire was placed parallel to the wall for all measurements, except for the spanwise two-point measurements.

A systematic study of the effect of spatial resolution effects was conducted by Ligrani and Bradshaw (1987). They found that the error in u' would be less than 4% for a wire length normalized by the Kolmogorov scale of $\ell/\eta < 10$ and $\ell/d > 200$. If $\eta \geq 100\,\mu$m, which is the case for most turbulent flows, then these conditions are satisfied for standard probes with $\ell = 1.25\,$mm and $d = 4 - 5\,\mu$m, such as the ones used in this work.

The limited spatial resolution has the effect of attenuating the measured spectrum. This effect becomes more severe as η/ℓ increases. Assuming $\eta \geq 100\,\mu$m, then for the probes used in the present experiments $\eta/\ell \approx 0.08$. This implies that the experiments will be affected by spatial averaging for $\kappa_1\ell \geq 0.5$, which corresponds to frequencies above 40 Hz for the present experiments. These effects were studied by Chin *et al.* (2011) by spatially filtering channel flow DNS data to mimic the effect of increasing the wire length. They concluded that the attenuation in $\sqrt{\bar{u}^2}$ was limited to the region near the wall ($y^+ < 300$), and has the effect of attenuating

the near wall peak located at $y^+ = 15$. They proposed a model to account for the "missing" energy, which can be added to the measured spectrum to obtain a "true" spectrum, which has also the effect of recovering the real magnitude of the turbulent kinetic energy peak at $y^+ = 15$.

Wire vibration. Regular vortex shedding from the hot wire filament can induce vibration of the wire, however, these effects are only a problem for velocities over 100 m/s with standard probes. If the wire is bowed due to thermal expansion and exposed to a periodic excitation, such as a Karman-vortex street, the wire can skip into a circular orbit with the same frequency as the Karman-vortex street, which can cause a decrease in the fluid velocity relative to the wire. In broadband turbulence conditions, such as the ones encountered in this research, this effect is not expected to be encountered.

Probe vibrations may also contaminate the results. When the pitch angle β (the angle between the mean velocity vector and the probe stem) is in the range $60° \leq \beta \leq 120°$ the prongs may vibrate due to vortex shedding, causing a periodic change in the wire resistance. Similarly, vortex shedding from the stem can also induce probe vibrations and contaminate the signal. In the present experiments, the pitch angle of the probes was always kept below 30°, and the changes in sensitivity due to pitch angle are taken into account through the calibration process, so these effects can be neglected.

Disturbance of the flow field by the presence of the probe can be a problem for measurements very close to the wall or when the pitch angle is large, which can cause a deflection of the flow around the prongs. For small pitch angles the effects are small and can be accounted for by the calibration process.

Reverse flow can cause errors in the velocity measurements, as the probe cannot discriminate between positive or negative velocity. This will only affect a small number of measurements obtained immediately behind the trailing edge, where some flow recirculation could be present; hence these results are not used.

Calibration errors due to the blockage effect of the probe on the nozzle of the calibrator. This causes a deflection of the flow around the probe. Errors of this type were found by Khan *et al.* (1987) to be about 3%. It is difficult to obtain accurate calibration at velocities below 3 m/s because the pressure differential across the nozzle of the calibrator becomes very small. This was not a problem in this work, as a high precision baratron was used to measure the pressure differential across the nozzle.

Insufficient sampling time can give rise to large statistical uncertainties. the correct selection of the sampling time and sampling frequency are crucial to obtain accurate measurements. This is discussed in more detail in the following section.

2.5.1 Uncertainty specification for measured statistical quantities

The following analysis follows those of Bruun (1995) and Bendat and Piersol (2011). The basic assumption is made that the probability density function (pdf) of the measured signal is Gaussian. This assumption is reasonable in many physical processes, but even when that is not the case, the analysis presented here can be used to obtain an order of magnitude estimate of the experimental uncertainty. Consider a random ergodic process. For a number of statistically independent samples $x(k)$, then the pdf(k) will be centred about the true ensemble average μ_x, and will have a standard deviation σ_x. If the pdf is offset by a quantity b from μ_x, then there is a bias or fixed error that must also be considered in addition to the random error.

The Gaussian pdf is given by:

$$p(z) = \frac{1}{\sqrt{2\pi}} exp(-z^2/2) \tag{2.2}$$

where :

$$z = \frac{x - \mu_x}{\sigma_x} \tag{2.3}$$

is the standardized variable. If $x(k)$ is an estimate of μ_x, then the uncertainty can be calculated as:

$$-z_{\alpha/2} < \frac{x(k) - \mu_x}{\sigma_x} < z_{\alpha/2} \tag{2.4}$$

where $z_{\alpha/2}$ is the value of z for which the probability $P(z_{\alpha/2}) = 1 - \alpha/2$, which means that $x(k)$ will fall between the interval

$$\mu_x - z_{\alpha/2}\sigma_x < x(k) < \mu_x + z_{\alpha/2}\sigma_x \tag{2.5}$$

with a probability of $(1 - \alpha)\%$. For a confidence level of 98%, $(1 - \alpha) = 98\%$, then $z_{\alpha/2} = 2.33$.

2.5.2 Digital signals

When a continuous signal $X(t), 0 \leq t \leq T$ is sampled and converted to a digital signal $X(n), n = 1, 2, ..., N$, the resultant finite time-history record is a discrete representation of the true signal. The number of samples N will be determined by the total sampling time T and the sampling rate f_s.

$$N = fs \times T \tag{2.6}$$

And the time interval between samples is

$$\Delta t = f_s^{-1} = T/N \tag{2.7}$$

the mean value is then defined as:

$$\hat{\bar{X}} = \frac{1}{N} \sum_{n=1}^{N} X(n) \tag{2.8}$$

and $\hat{\bar{X}}$ is an unbiased estimate of the true mean $\bar{X}$. The uncertainty of $\hat{\bar{X}}$ can be estimated using the variance of $\hat{\bar{X}}$. For an unbiased estimate, the mean square error is equal to the variance:

$$\sigma^2[\hat{\bar{X}}] = E[(\hat{\bar{X}} - \bar{X})^2] \approx \frac{2T_I \sigma_x^2}{T} \tag{2.9}$$

where σ_x^2 is the variance of the sample record, $X(t)$, and T_I is the integral time scale, defined as:

$$T_I = \int_0^T \rho_x(\tau) d\tau \tag{2.10}$$

where ρ_x is the autocorrelation coefficient. The number of statistically independent samples can be determined as:

$$N_I = \frac{T}{2T_I} \tag{2.11}$$

2.5.3 Mean velocity

As was discussed in the previous section, the uncertainty for a given statistical quantity can be estimated to a given accuracy if the number of independent samples and the variance of the sample are known. Figure 2.8(b) shows the number of independent samples as a function of wall normal distance, for a sample record of a

single hot wire in the near wake of the FP-12 airfoil 1. The number of independent samples decreases in the outer part of the boundary layer, due to the increase in the integral time scale T_I, which is shown in Figure 2.8(a). This is consistent with the presence of larger flow structures in the outer part of the boundary layer, and smaller structures close to the wall. The local turbulence intensity is given by:

$$T_i = \frac{\sigma_u}{\hat{\bar{u}}} \tag{2.12}$$

and is shown in Figure 2.7. The local turbulence intensity is seen to increase as the wall is approached, due to the decrease in the local mean velocity and the increase in the turbulent kinetic energy. The uncertainty for the measured mean velocity is calculated using

$$\sigma^2[\hat{\bar{u}}] = E[(\hat{\bar{u}} - \bar{u})^2] \approx \frac{2T_I\sigma_u^2}{T} \tag{2.13}$$

and is shown in Figure 2.9(a). The uncertainty is less than 3.5% across the boundary layer.

2.5.4 RMS velocity

The procedure for calculating the uncertainty for $\hat{\overline{u^2}}$ is the same as the one used for the mean velocity. The uncertainty of $\hat{\overline{u^2}}$ is given by its variance:

$$\sigma^2[\hat{\overline{u^2}}] = E[(\hat{\overline{u^2}} - \bar{\overline{u^2}})^2] \approx \frac{2T_I\sigma_u^4}{T} \tag{2.14}$$

By substituting $N_I = T/2T_I$ we obtain

$$\sigma^2[\hat{\overline{u^2}}] \approx \frac{\sigma_u^4}{N_I} \tag{2.15}$$

The normalized RMS error is then

$$\epsilon[\hat{\overline{u^2}}] = \frac{\sigma[\hat{\overline{u^2}}]}{\sigma_u^2} \approx \frac{1}{\sqrt{N_I}} \tag{2.16}$$

The uncertainty for the RMS velocity $(\hat{\overline{u^2}})^{1/2}$ can be calculated from

$$\epsilon[(\hat{\overline{u^2}})^{1/2}] \approx \frac{\epsilon[\hat{\overline{u^2}}]}{2} \tag{2.17}$$

Figure 2.9(b) shows the calculated uncertainty for $(\hat{\overline{u^2}})^{1/2}$ with a 98% confidence level, as a function of distance to the wall y/δ. The uncertainty does not exceed 2.3% across the boundary layer.

2.5.5 Higher order moments

The mth order moment of the fluctuating component of $x(t)$ is defined as

$$\overline{x^m} = \lim_{T\to\infty} \frac{1}{T} \int_0^T x^m(t)dt \tag{2.18}$$

where $m = 1, 2, 3, ...$ is a positive integer. The measured third order moment $\hat{\overline{x^3}}$, is defined as

$$\hat{\overline{x^3}} = \frac{1}{T} \sum_{n=1}^{N} \left(X(n) - \hat{\bar{X}} \right)^3 \tag{2.19}$$

When presented in normalized form it is called the skewness,

$$S = \frac{\hat{\overline{x^3}}}{\sigma_x^3} \tag{2.20}$$

The skewness provides an indication of the lack of statistical symmetry of the signal.

The normalized fourth order moment $\hat{\overline{x^4}}$ is called the kurtosis or flatness factor, and is a measure of the size of the tails of the probability density function. The kurtosis is defined as

$$K = \frac{\hat{\overline{x^4}}}{\sigma_x^4} \tag{2.21}$$

The uncertainty estimates for the skewness and kurtosis are given by $\sigma_x^3(6/N_I)^{1/2}$ and $\sigma_x^4(96/N_I)^{1/2}$, respectively, and are shown in Figure 2.10. They peak at 4% for the skewness and 12% for the kurtosis.

2.5.6 Autocorrelations

A conservative estimate for the variance of the autocorrelation function $\hat{R}_x(\tau)$ is given by

$$\mathrm{var}[\hat{R}_x(\tau)] = \frac{T_I \sigma_x^4}{T} [1 + \rho_x^2(\tau)] \tag{2.22}$$

For $\tau = 0$, the uncertainty in the autocorrelation is the same as for the mean square value.

$$\sigma[\hat{R}_x(\tau = 0)] \approx \sigma[\hat{\overline{x^2}}] \tag{2.23}$$

2.5.7 Cross-correlation

Provided that $\rho_x(\tau) \approx \rho_y(\tau)$, a conservative estimate for the variance of the cross-correlation $\hat{R}_{xy}(\tau)$ is given by

$$\text{var}[\hat{R}_{xy}(\tau)] = \frac{T_I \sigma_x^2 \sigma_y^2}{T}[1 + \rho_{xy}^2(\tau)] \tag{2.24}$$

where $\rho_{xy}^2(\tau) = \hat{R}_{xy}(\tau)/\sigma_x^2\sigma_y^2$ is the cross-correlation coefficient. The error for the cross-correlation will be similar to the error of the auto-correlation function.

2.5.8 Autospectrum

The one-sided autospectral density,$G_x(f)$, can be estimated by

$$\tilde{G}_x(f) = \frac{2}{T}|X(f,T)|^2 \tag{2.25}$$

However, this results in a high random error and spectral leakage. This can be minimized by dividing the time-history record into segments (sub-records) and applying a data window (typically Hanning) to each segment to eliminate discontinuities at the ends of the segments. An estimate of the spectrum $\hat{G}_x(f)$ can then be calculated by an ensemble of estimates from n_d sub-records of length T_d,

$$\hat{G}_x(f) = \frac{2}{n_d T_d} \sum_{j=1}^{n_d} |X(f,T)|^2 \tag{2.26}$$

if the sub-records are statistically independent,then:

$$\text{var}[\hat{G}_x(f)] = \frac{\text{var}[\tilde{G}_x(f)]}{n_d} = \frac{G_x^2(f)}{n_d} \tag{2.27}$$

The uncertainty can then be estimated from

$$\epsilon_r[\hat{G}_x(f)] = \frac{1}{\sqrt{n_d}} \tag{2.28}$$

The uncertainty then depends on the type and number of windows, and on the overlap between windows. The more windows, the smaller the random error becomes, and the smoother the resulting spectrum will be, at the cost of reduced frequency resolution. In the present experiments, data were sampled at 20 kHz for 8 seconds. The spectra were calculated using the Welch method, with a Hanning window of 625 points and a 50% overlap, resulting in a frequency resolution of 5 Hz and $n_d = 511$ segments. Therefore the error is $\epsilon_r[\hat{G}_x(f)] = 4.42\%$. A similar analysis applies to the cross-spectrum, resulting in the same error estimate.

2.5.9 Probability density functions

An estimate of the probability density function is given by:

$$\hat{\bar{p}}(x) = \frac{N_x}{NW} \tag{2.29}$$

where N is the total number of samples, and N_x is the number of points in the interval $x \pm W/2$. The estimate is not unique, as it depends on the width W of the amplitude intervals. The estimate $\hat{\bar{p}}(x)$ is a biased estimate, so the total error is given by:

$$E[(\hat{\bar{p}}(x) - p(x))^2] = \mathrm{var}[\hat{\bar{p}}(x)] + b^2[\hat{\bar{p}}(x)] \tag{2.30}$$

where b is the bias of the estimate. it can be shown that

$$\mathrm{var}[\hat{\bar{p}}(x)] \approx \frac{p(x)}{N_I W} \tag{2.31}$$

where N

$$b[\hat{\bar{p}}(x)] \approx \frac{W^2}{24} p^{''}(x) \tag{2.32}$$

where $p^{''}(x)$ is the second derivative of $p(x)$with respect to x. The normalized mean square error is then:

$$\epsilon^2[\hat{\bar{p}}(x)] = \frac{1}{N_I W p(x)} + \frac{W^4}{24^2}\left[\frac{p^{''}(x)}{p(x)}\right]^2 \tag{2.33}$$

a large value of W is desirable to reduce the random error, but it increases the bias error. In practice, for $W \leq 0.2\sigma_x$ the normalized bias error is less than 1%. For the current experiments, W is selected as corresponding to 321 intervals covering the

amplitude range $\pm 3\sigma_x$, that is $W = 0.1\sigma_x$. Neglecting the bias error, then:

$$\epsilon^2[\hat{\bar{p}}(x)] = \frac{10}{\sigma_x N_I p(x)} \tag{2.34}$$

If $p(x)$ is a normalized Gaussian function, then $p(0) = 1/(2\pi)^2 \approx 0.4$, then the normalized mean square error is:

$$\epsilon^2[\hat{\bar{p}}(0)] = \frac{10(2\pi)^{1/2}}{\sigma_x N_I} \tag{2.35}$$

The resulting error is shown in Figure 2.5.9, and can be seen to remain below 10% in the interval $-0.8 \leq y/\delta \leq 0.8$ and increases to approximately 30% at the edge of the boundary layer.

2.6 Summary

In this chapter the experimental setup and methodology have been described. The principles of operation of constant temperature hot wire anemometry have been revised and the most significant error sources have been identified. Significant effort has been made to minimize the uncertainty in the measurements, including carefully aligning the traverse and frequent calibration of the hot wire probes. A thorough error analysis has been carried out to estimate the experimental uncertainty of all measured statistical quantities. The errors are generally small, but increase as the probes approach the wall. An increase in the uncertainty is also observed at the edge of the boundary layer, due to the larger time scale of the flow in that region, which results in less statistically independent samples. The errors are summarized in Table 2.1.

Table 2.1: Summary of experimental uncertainties.

Quantity	$\hat{\bar{U}}$	$\sqrt{\hat{\bar{u^2}}}$	S_u	K_u	pdf(u)	$G_x(f)$
Maximum Error	3.5 %	2.5%	4%	12%	30%	4.42%

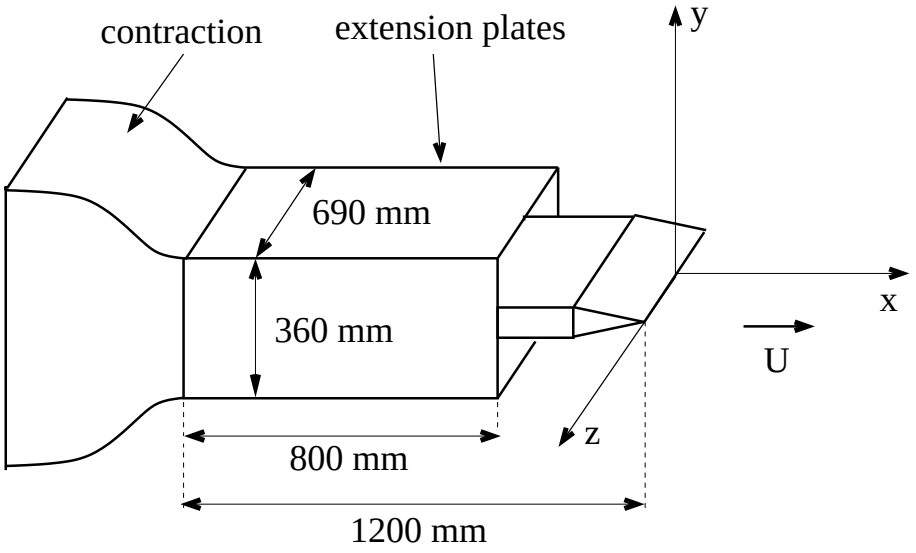

Figure 2.1: Schematic of the wind tunnel contraction with extension plates and model used in the experiments. The coordinate system was centered at the trailing edge of the model at the mid span point.

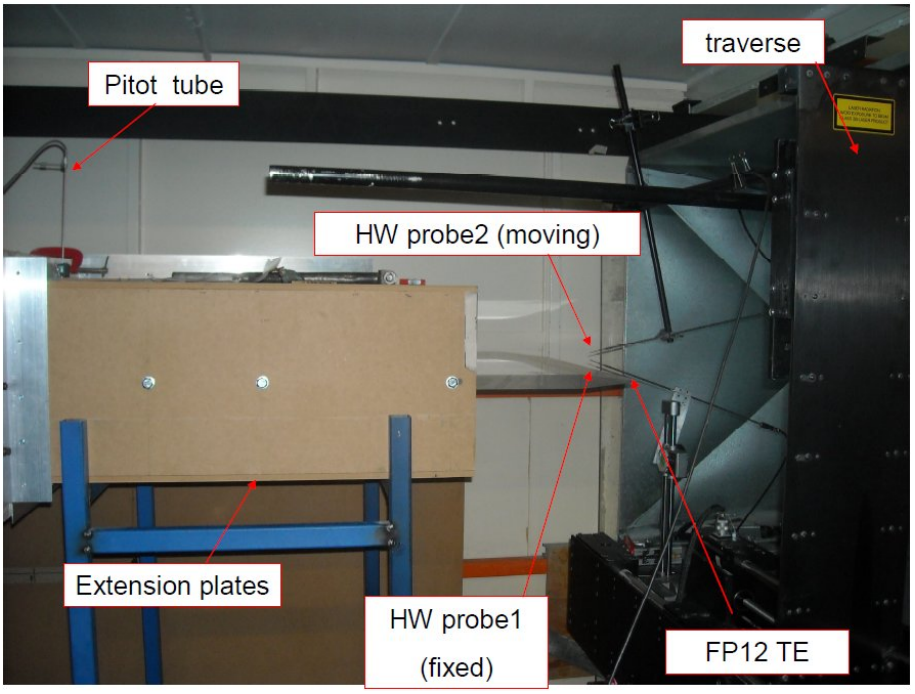

Figure 2.2: Experimental setup.

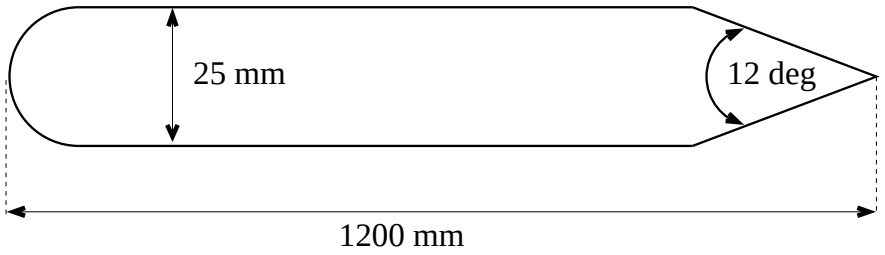

(a) FP-12

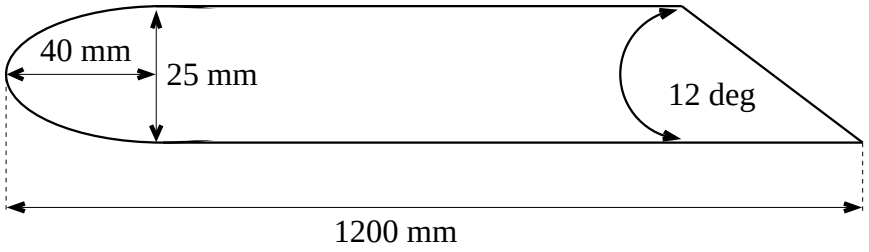

(b) FP-12-B

Figure 2.3: Test cases used in the experiments. The models have a trailing edge of 1 mm thickness.

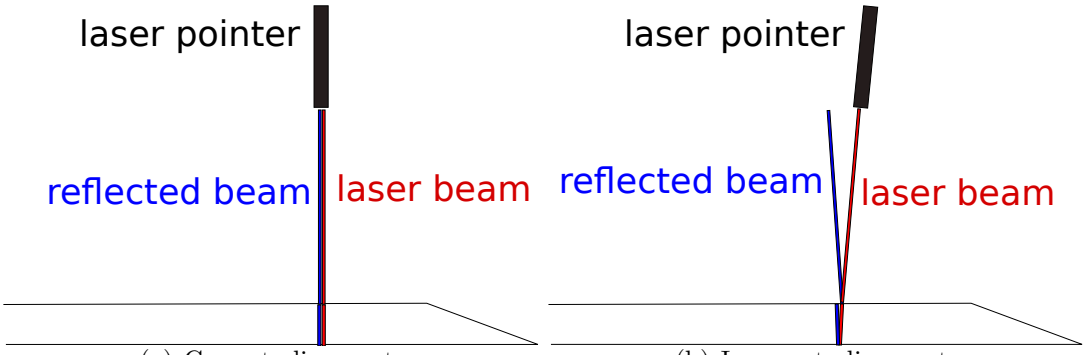

(a) Correct alignment.

(b) Incorrect alignment.

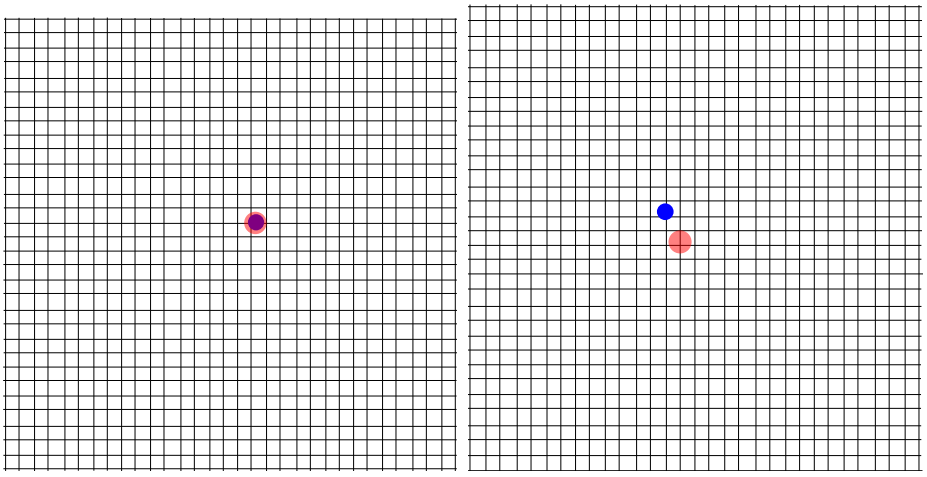

(c) Correct alignment.

(d) Incorrect alignment.

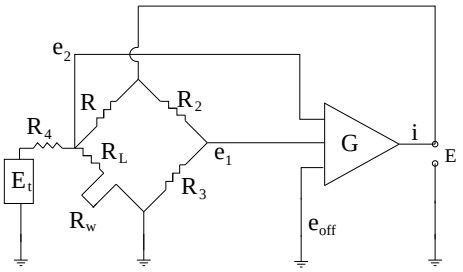

Figure 2.4: The CT anemometer containing a Wheatstone bridge, a feedback amplifier, and an electronic testing subcircuit, adapted from Bruun (1995).

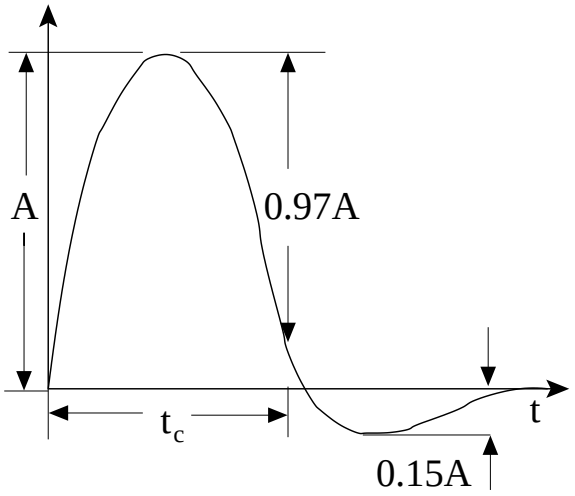

Figure 2.5: Ideal response of the CT anemometer to the square wave test.

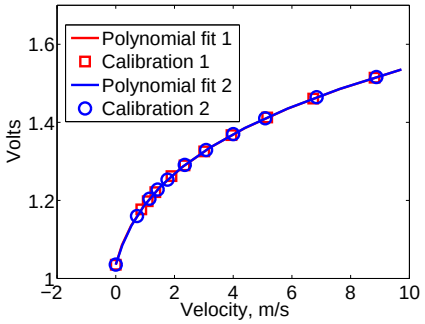

Figure 2.6: Typical calibration curves for before (red) and after (blue) a set of measurements.

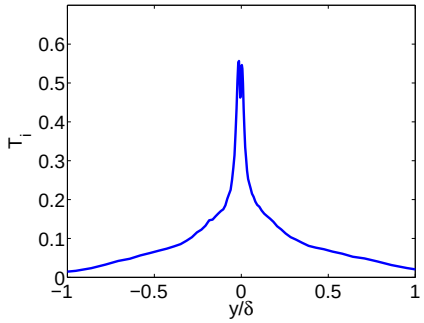

Figure 2.7: Local Turbulence Intensity as a function of normalized distance to the wall.

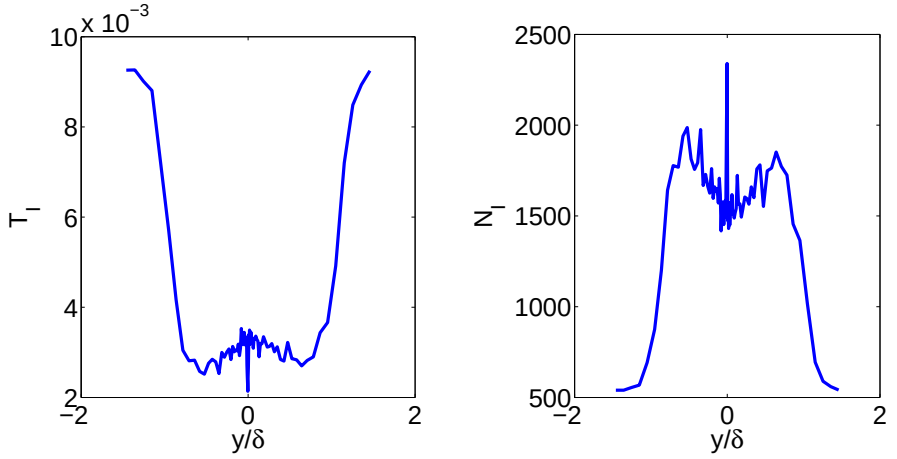

(a) Integral time scale (b) Number of independent samples

Figure 2.8: Integral time scale and number of statistically independent samples for measurements in the near wake of the FP-12.

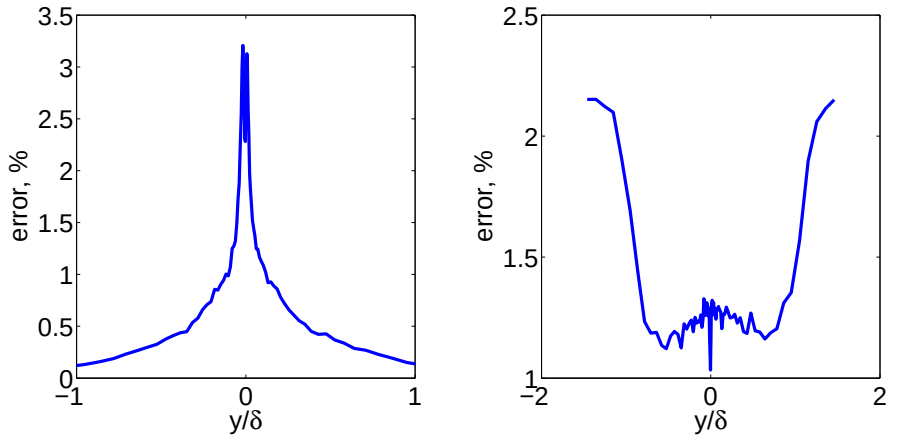

(a) Mean Velocity (b) RMS velocity

Figure 2.9: Normalized error for the mean and RMS velocity.

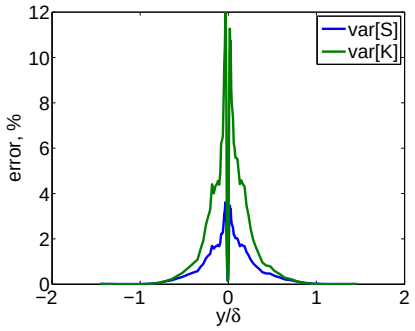

Figure 2.10: Normalized error for the skewness and kurtosis.

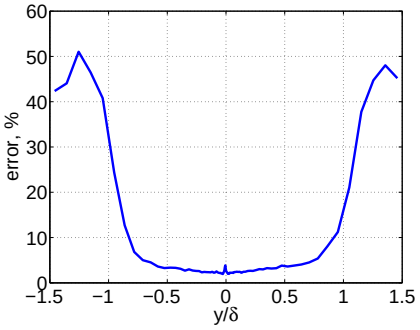

Figure 2.11: Normalized error for the probability density function as a function of normalized distance to the wall.

Chapter 3

Experimental results

Understanding the flow in the vicinity of the trailing edge is crucial for the development of trailing edge noise models, and boundary layer statistics are a means to obtain this understanding. There is a large body of research on boundary layers over flat plates at zero pressure gradient (Osterlund 1999, Ganapathisubramani *et al.* 2005, Favre *et al.* 1957), but much less research on boundary layers in the pressence of adverse and favourable pressure gradients (Harun 2012, Cipolla and Keith 2000). In particular, experimental data for turbulence statistics of boundary layers over airfoils, especially near the trailing edge, are not widely available.

The main aim of this chapter is to investigate the flow near the trailing edge of two sharped edged struts. The struts were described in chapter 2. The different trailing edge configurations provide three different pressure gradients. In the remainder of this chapter, they will be referred to as Case 1 (the flat side FP-12-B), Case 2 (FP-12) and Case 3 (inclined side of FP-12-B). The effects of the pressure gradient on the flow structure are investigated using hot wire anemometry. Case 1 provides a canonical test case which allows the validation of the experimental results against numerical and experimental data from the literature, and also provides a bench mark to which the other cases can be compared.

The parameters investigated include the mean and RMS velocity profiles, probability density functions, third and fourth order moments, spectral density, two-point correlations and coherence function. The insights gained from these experiments will be used to develop a model for the cross-spectrum of turbulent velocity, which is required as an input to RSNM.

3.1 Integral boundary layer parameters

The boundary layer displacement thickness δ^* and momentum thickness θ were calculated from the mean velocity profiles using:

$$\delta^* = \int_0^\delta \left(1 - \frac{U}{U_e}\right) d|y - y_0| \tag{3.1}$$

$$\theta = \int_0^\delta \frac{U}{U_\infty}\left(1 - \frac{U}{U_e}\right) d|y - y_0| \tag{3.2}$$

Where U is the mean flow velocity, U_e is the flow velocity at the edge of the boundary layer and y_0 is point of minimum free stream velocity if the measurements are taken just downstream of the trailing edge, or the position of the airfoil surface if the measurements are taken upstream from the trailing edge. The standard definition of δ as the location where the mean velocity reaches 99% of the free stream velocity is troublesome for flows whith significant streamline curvature, such as flow over airfoils. In this work, δ is defined instead as the location where the turbulent kinetic energy reaches 0.5% of its peak value, or $k = 0.005k_{max}$ This value was chosen because it produced the same value of δ as using the 99% of the free stream velocity for the ZPG case (flat plate). In order to accurately calculate the boundary layer thickness, the experimental data was interpolated by fitting a fifth degree polynomial in the outer region of the boundary layer with a resolution of $dy = 0.01$ mm. Figure 3.1 shows the mean velocity profile and the curve fit used to calculate the boundary layer thickness for Case 1. The calculated boundary layer parameters are shown in Table 3.1. Case 1 presents a very mild pressure gradient, close to zero.

The pressure gradient paramenter β is defined as

$$\beta = \frac{\delta^*}{\tau_w}\frac{dP}{dx} \tag{3.3}$$

where $\tau_w = \rho u_\tau^2$ is wall shear stress. The pressure gradient was obtained from CFD simulations by taking the pressure over the surface of the airfoil between $0.95 \leq$

Table 3.1: Boundary layer parameters for all cases.

case	δ/c	δ^*/δ	θ/δ	H	u_τ	β	R_θ
Case 1	0.026	0.181	0.117	1.55	0.3019	0.13	1.67×10^3
Case 2	0.032	0.208	0.130	1.60	0.2513	0.83	2.21×10^3
Case 3	0.024	0.237	0.139	1.70	0.2458	1.18	1.84×10^3

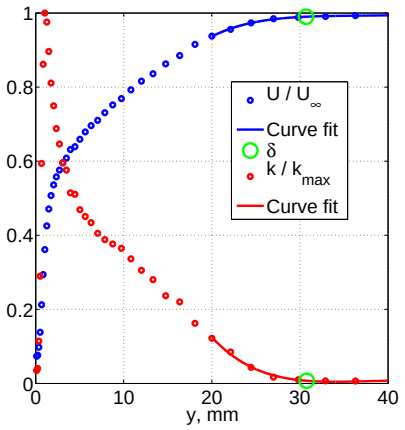

Figure 3.1: Mean Velocity and turbulent kinetic energy profiles and curve fits used to calculate the boundary layer thickness δ,for the ZPG case. $x/c = 1.0008$

$x/c \leq 1$ and calculating the slope by applying a linear fit to the data, as shown in Figure 3.2.

The friction velocity u_τ and the skin friction coefficient C_f were determined from the mean velocity profiles using the Clauser method (Clauser 1954). When viewed as a function of Reynolds number Re_θ, the skin friction coefficient shows reasonable agreement with the values obtained by Coles (1962), Purtell *et al.* (1981) and Spalart (1988), for Case 1, as shown in Figure 3.3(a). For Cases 2 and 3, the agreement deteriorates significantly. The discrepancies are likely due to the difficulty of estimating the friction velocity from the Clauser method for boundary layers at such low Reynolds numbers in the presence of stronger adverse pressure gradients (APG).

The combined effects of the APG and low Reynolds number of the current test cases make the logarithmic region of the boundary layer very small, in fact, one could argue that there is no identifiable logarithmic region, making it difficult to obtain

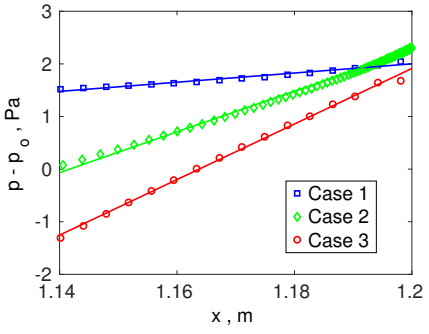

Figure 3.2: Pressure on the surface for all cases obtained from CFD.

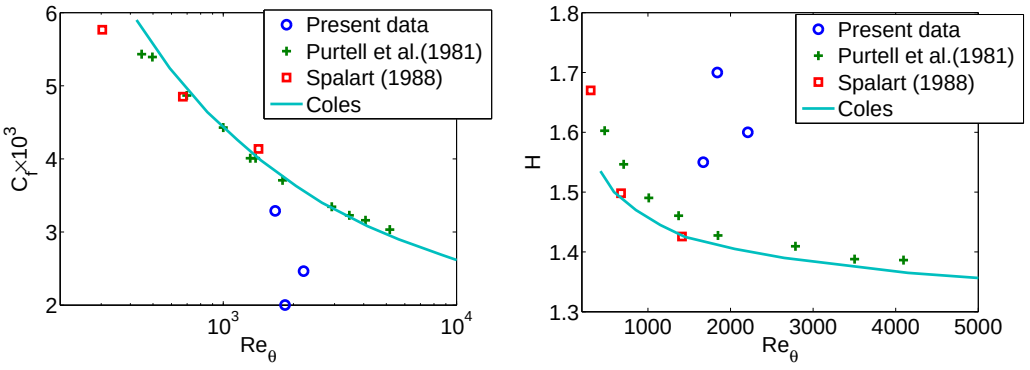

Figure 3.3: Skin friction coefficient and shape factor as a function of Reynolds number. Current data in ascending Re_θ: Case 1, Case 3, Case 2.

the friction velocity using the Clauser method. This confirms the results obtained by Harun (2012), who also reported the lack of a logarithmic region in when an adverse pressure gradient was present. Harun (2012) compared the results obtained with the Clauser method to those obtained using oil film interferometry, and established that estimating u_τ with the Clauser method can result in significant errors in the presence of adverse pressure gradients.

Figure 3.3(b) shows the shape factor $H = \delta^*/\theta$ as a function of Reynolds numbers. The values of H for the present data are higher than what is observed in the experimental data of Purtell *et al.* (1981), in the DNS data of Spalart (1988) and in Coles' law of the wall for similar Reynolds number. A shape factor of $1.3 \leq H \leq 1.5$ corresponds to turbulent flow, and a value of $H = 2.6$ indicates laminar flow. Therefore, the present results of 1.55 to 1.7 indicate that the flow is turbulent and well developed.

3.1.1 Mean and RMS velocity profiles

The mean and RMS velocity profiles, normalized by viscous scales, are plotted in figures 3.4(a) and 3.4(b), respectively, and compared to data from the literature. It can be observed that the data for the ZPG case follows the law of the wall very well between $30 < y^+ < 100$, and also compares well with the DNS data of Spalart (1988) for a turbulent boundary layer of similar Reynolds number. The extent of the log-region for the current data is much smaller than for the data of Klebanoff (1954). This is a consequence of the Reynolds number being lower for the present case ($Re_\delta = 13,300$) than for Klebanoff's data ($Re_\delta = 152,000$).

As figure 3.4(b) shows, when plotted using viscous scaling, the RMS velocity profile

for Case 1 agrees reasonably well with the experimental data of Purtell *et al.* (1981) and with the DNS data of Spalart (1988), both corresponding to zero pressure gradient boundary layers of $Re_\theta = 1,340$ and $Re_\theta = 1,410$, respectively. As the pressure gradient is increased, the data show clear differences with the ZPG cases. The stronger adverse pressure gradient causes a secondary peak at $y^+ = 100$ in the RMS velocity profile for Cases 2 and 3, its amplitude increasing with increased APG. This secondary peak is consistent with the findings of Harun (2012), who obseved that the magnitude of the secondary peak is related to energy associated with the large-scale structures of the flow, which suggest that the dominant energetic motions have shifted from the near-wall region to the outer part of the boundary layer.

3.1.2 Turbulence dissipation

The turbulence dissipation ϵ was calculated from the experimetal data using the following relation (Saddoughi and Veeravalli 1994),

$$\epsilon = 15\nu \int E_{11}(\kappa_1)\kappa_1^2 d\kappa_1 \tag{3.4}$$

where κ_1 is the wavenumber, E_{11} is the measured wavenumber autospectrum of u' and $\nu = 1.5 \times 10^{-5}$ is the kinematic viscosity. The turbulence dissipation ϵ for the three cases is shown in Figure 3.5. There is an almost perfect overlap between Case 1 and Case 2 in the region $30 \leq y^+ \leq 200$, however, Case 3 shows significantly higher levels of dissipation in this region. For $y^+ \leq 30$ the dissipation increases sharply, as expected near the wall. The discrepancies between the three cases can be attributed to the different turbulent kinetic energy levels in this region, as well as the difficulty in obtaining an accurate value of u_τ, which produces a shift in y^+ that will be noticeable only for small y^+ when plotted in log-scale.

3.1.3 Probability density functions

The probability density function provides a statistical characterization of the velocity U. Figure 3.6(a) shows the probability density function of the streamwise velocity fluctuations u' normalized by the local convection velocity U_c at $y^+ \approx 80$. The convection velocity is taken as the mean velocity at the position of the hot-wire probe. It can be observed that the PDFs are nearly Gaussian in this region, which corresponds to the logarithmic region of the boundary layer. Near Gaussian

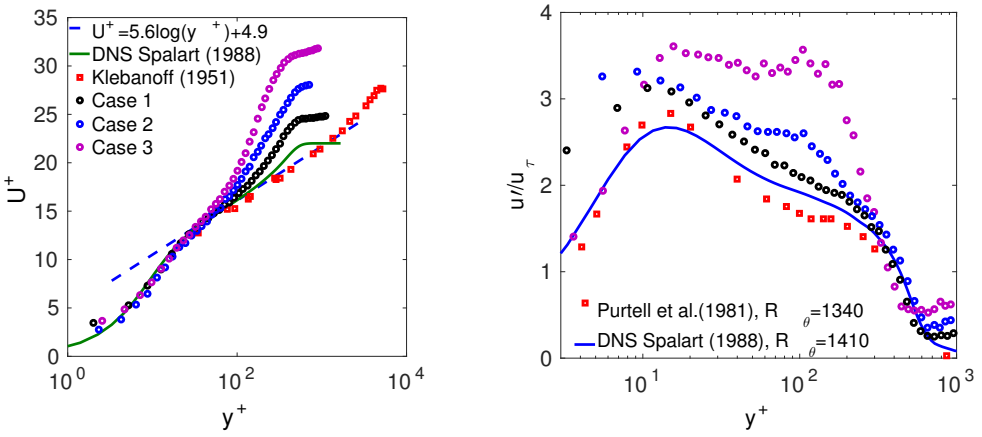

(a) Mean Velocity (b) RMS velocity

Figure 3.4: Mean and RMS velocity profiles in wall units. Measurements taken at $x/c = 1.0008$. Circles in Figure 3.4(b) as in legend of Figure 3.4(a).

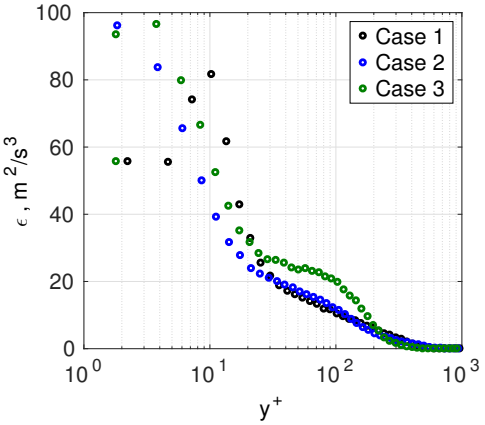

Figure 3.5: Turbulence dissipation as a function of normalized distance to the wall. $x/c = 1.0008$

distributions are expected in this region of the boundary layer, as shown by Lindgren and Johansson (2004). The PDFs are nearly identical for Cases 1 and 2, but a wider PDF is observed for Case 3 , which indicates that stronger velocity fluctuations are more likely in the presence of a stronger adverse pressure gradient, which is consistent with the increased turbulence intensity levels for Case 3 case shown in Figure 3.4(a). In the experiments of Moreau *et al.* (2011), there were no differences in the noise spectra for the three different airfoils tested at $Re_\theta = 500,000$ (significant differences were observed at lower Re_θ). Each airfoil had a different trailing edge bevel angle, which correspond to Cases 1, 2 and 3 in this research. Therefore, the broadening of the PDF observed in the present experiments do not seem to have an effect on the far field noise.

3.1.4 Higher order moments

The skewness is the nondimensional form of the third moment,

$$S = \overline{u^3}/\sigma_u^3 \tag{3.5}$$

and it is an indicator of statistical symmetry in the signal. A value of $S = 0$ means the signal is perfectly symmetrical.

Similarly, the kurtosis, or flatness factor, is the nondimensional form of the fourth order moment,

$$K = \overline{u^4}/\sigma_u^4 \tag{3.6}$$

and it provides an indication of the sharpness of the peak in a signal. A high value of K indicates that much of the variance is the result of infrequent extreme deviations. A value of $K = 3$ is typical of Gaussian distributions.

Figures 3.7 show the skewness and kurtosis as a function of y^+ and y/δ for the three test cases.

Examination of the skewness shows that the signal is slightly negatively skewed up to $y^+ = 200$, and becomes significantly more skewed towards the edge of the boundary layer for all cases. Beyond $y/\delta = 1.2$ the skewness returns to the Gaussian values. This region corresponds to the potential core of the jet of the wind tunnel, where turbulence is expected to be homogeneous.

Similarly, the kurtosis shows nearly Gaussian values between $31 \leq y^+ \leq 200$, and increases rapidly towards the edge of the boundary layer. Beyond $y/\delta = 1.2$ the

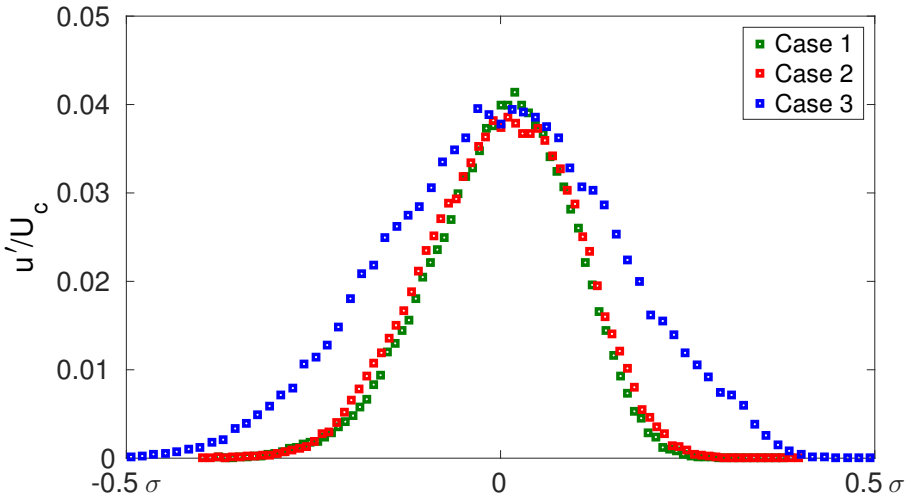

Figure 3.6: Probability density functions of turbulent velocity. $x/c = 1.0008$.

kurtosis returns to the Gaussian values.

Examination of the higher order moments confirms a nearly Gaussian distribution in the logarithmic region of the boundary layer, with the outer part of the boundary layer departing from a Gaussian distribution, and being dominated by relatively infrequent extreme events, which correspond to larger structures or eddies. The large peaks in both the kurtosis and skewness for all cases at $y/\delta \approx 0$ is most likely caused by vortex shedding from the trailing edge.

3.1.5 Integral length scale

The longitudinal integral lengthscale L_{11} can be obtained from the autocorrelation coefficient $f(x)$,which is in turn related to the wave number spectrum $E_{11}(\kappa_1)$.

$$L_{11} = \int_0^\infty f(x)dx = \frac{\pi E_{11}(\kappa_1 = 0)}{2\langle u_1^2 \rangle} \tag{3.7}$$

The integral length scales obtained with this procedure are plotted in non-dimensional form in Figure 3.8(a) as a function of distance from the wall normalized by the boundary layer thickness. The length scale increases as a function of the distance to the wall. The turbulence length scale can be defined in terms of the turbulent kinetic energy $k = 1.5u'^2$ and dissipation ϵ as

$$L = \frac{k^{3/2}}{\epsilon} \tag{3.8}$$

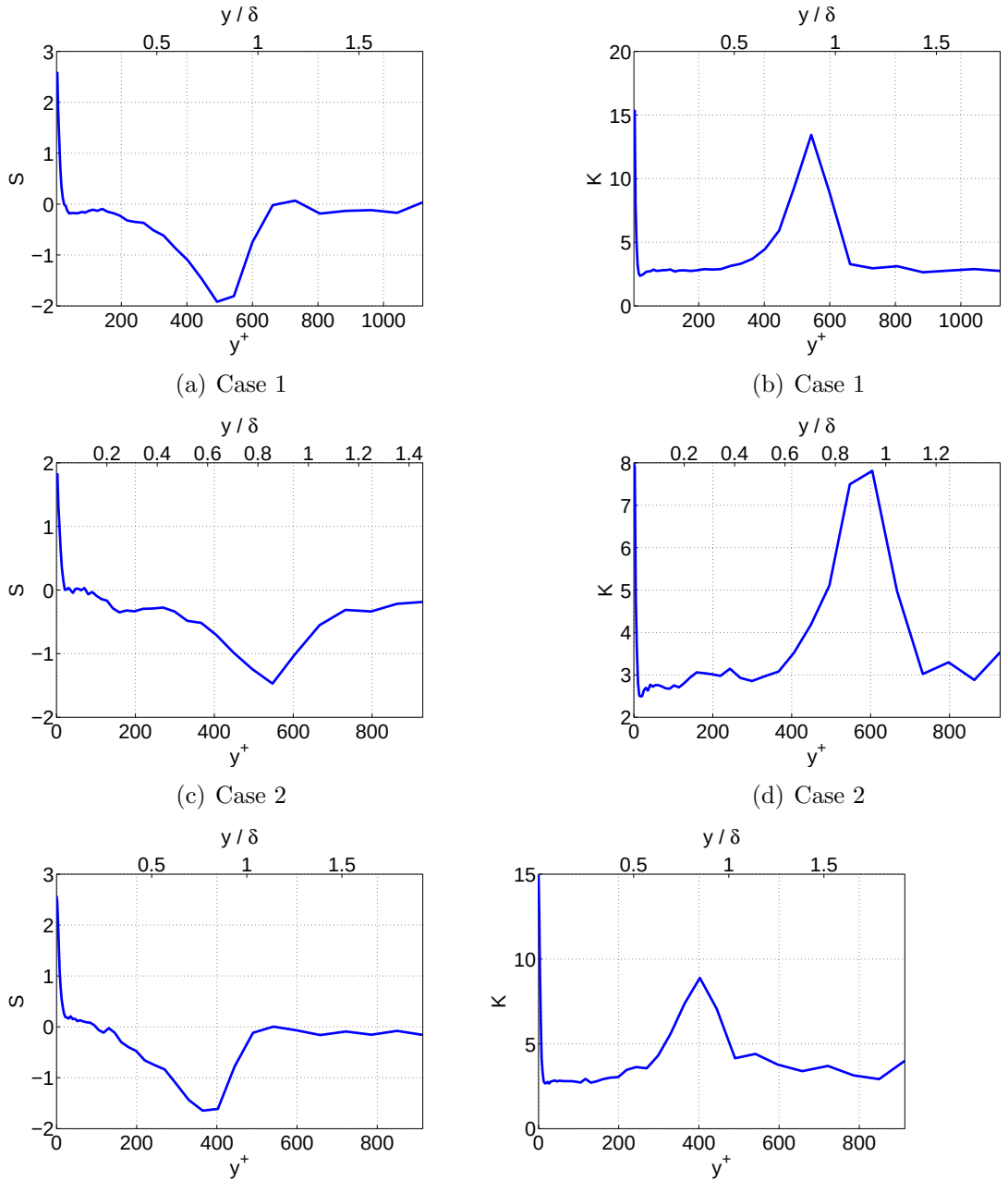

(a) Case 1 (b) Case 1

(c) Case 2 (d) Case 2

(e) Case 3 (f) Case 3

Figure 3.7: Third and fourth order moments of the streamwise velocity measured at $x/c = 1.0008$.

This length scale also increases with distance to the wall, but decreases again past $y/\delta = 0.6$. For Cases 1 and 2, it reaches a plateau between $0.2 \leq y/\delta \leq 0.6$, but this is not observed for Case 3. The stronger adverse pressure gradient produces larger length scales, which indicates the presence of larger structures. From the experiments of Moreau *et al.* (2011) it would appear that the increased length scales due to the greater pressure gradient had no effect on the resulting TE noise.

3.1.6 Autocorrelation function

The autocorrelation function was measured using a single wire and making use of the frozen turbulence hypothesis, where $\Delta x = U_c t$ and U_c is the convection velocity, taken here as the local mean. Figures 3.9(a) to 3.9(c) show the autocorrelation as a function of streamwise separation for Cases 1, 2 and 3, respectively. For Cases 1 and 2, the signals decorrelate well within $\Delta x = 2\delta$. The stronger pressure gradient of Case 3 causes the signals to remain correlated for a longer distance, particularly in the outer part of the boundary layer. This indicates the presence of larger flow structures, which could be related to vortex shedding from the vertex created by the tapered end of the airfoil, which has a steeper angle for Case 3 than for Case 2.

3.1.7 Turbulent velocity two-point correlation

The velocity two-point correlation contains information on the spatial structure of the flow. It is defined as

$$R_{ij} = \langle u_i(\mathbf{x}, t) u_j(\mathbf{x} + \mathbf{r}, t) \rangle \tag{3.9}$$

where u_i is the fluctuating component in the i direction, and $\mathbf{r} = (r_1, r_2, r_3)$ is the spatial separation between probe 1 (stationary) and probe 2 (moving). In these experiments, only the streamwise component of velocity u_1 was measured, and hence all results shown are for

$$R_{11} = \langle u_1(\mathbf{x}, t) u_1(\mathbf{x} + \mathbf{r}, t) \rangle \tag{3.10}$$

where $\mathbf{r} = 0$ corresponds to the autocorrelation for probe 1, and all results are normalized by $R_{11}(r = 0, \mathbf{x}, t)$.

Two-point correlations in the wall normal direction as a function of probe separation are shown in Figures 3.10(a) to 3.10(f), 3.12(a) to 3.12(f), and 3.14(a) to 3.14(f)

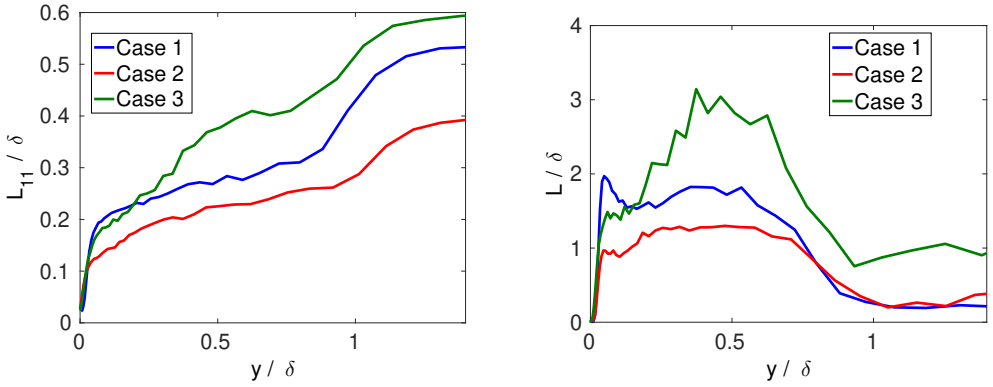

(a) (b)

Figure 3.8: Length scales normalized by boundary layer thickness. Data obtained at $x/c = 1.0008$.

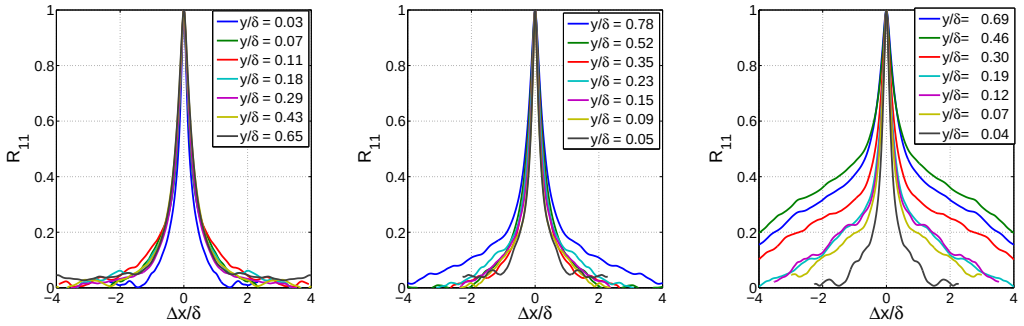

(a) Case 1 (b) Case 2 (c) Case 3

Figure 3.9: Streamwise autocorrelation for various values of y/δ. $x/c = 1.0008$.

for Cases 1, 2 and 3, respectively. Similarly, correlations in the spanwise direction are shown in Figures 3.11(a) to 3.11(e),3.13(a) to 3.13(f) and 3.15(a) to 3.15(f) for Cases 1, 2 and 3, respectively.

The correlation decays much faster closer to the wall than it does away from it, which is consistent with the presence of larger flow structures in the boundary layer as distance from the wall is increased, as shown by the longitudinal length scale plot (Figure 3.8(a)). For the wall normal correlations, a shift in time (time delay) of the peaks is observed, suggesting that the flow structures are inclined at an angle to the wall. The time delay decreases as distance y/δ increases, as the velocity gradient becomes less steep. The time delay is not present in the spanwise correlation, as there is no mean velocity gradient in this direction to stretch the eddies. There is a significant change in the tails of the correlations as the edge of the boundary layer is approached. The Signals remain correlated for a larger distance, which confirms the presence of larger flow structures in the outer part of the boundary layer.

Figures 3.16(a) to 3.16(f) show correlation contours in the x-y (wall normal) and x-z (wall parallel) planes for all cases at $y^+ = 80$. The frozen turbulence hypothesis has been used here to account for the probe separation in the streamwise direction. The correlation contours in the x-y plane are clearly inclined, confirming the inclination of the turbulent structures observed in the two-point correlation plots. This inclination is not present in the contours in the x-z plane. Similar results were observed by Gavin (2002). In his experiments, he describes regions of correlated fluid displaying elliptical iso-contours, elongated in the streamwise direction and with their major axes inclided toward the wall. Figures 3.17(a) to 3.17(e) show the correlation contours for $y/\delta = 0.3$. A similar pattern is observed at this location in the boundary layer, but the correlations are slightly wider and stronger than at $y^+ = 80$, which is consistent the presence of larger flow structures in this region of the boundary layer. The signals remain correlated for larger distances in the wall-normal direction than in the spanwise direction for all cases.

3.1.8 Turbulent velocity auto-spectrum

The autospectral density function, or wavenumber spectrum, $E_{11}(\kappa_1, \mathbf{y_1}, \mathbf{y_1})$ provides a measure of the energy distribution of a signal as a function of wavenumber κ_1. The Kolmogorov hypothesis states that the scaled spectrum $E_{11}(\kappa_1, \mathbf{y_1}, \mathbf{y_1})/(\epsilon\nu^5)^{1/4}$ is a universal function of $\kappa_1\eta$ at sufficiently high Reynolds number, where η is the

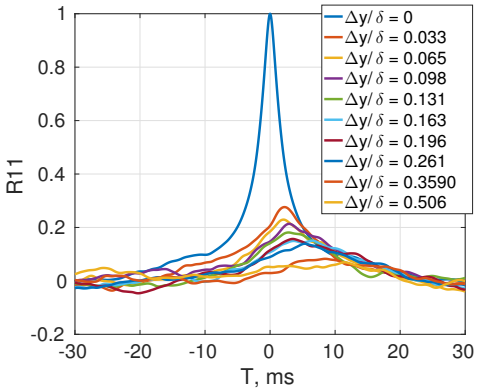

(a) y=1 mm, $y/\delta = 0.0326$.

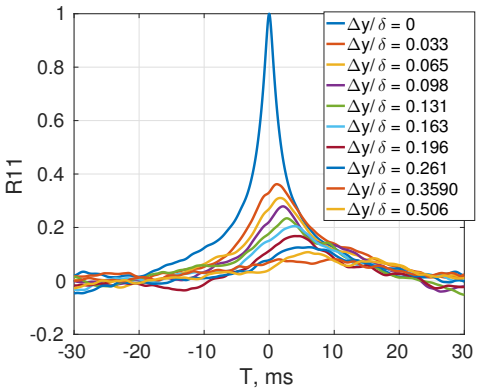

(b) y=2 mm, $y/\delta = 0.0653$.

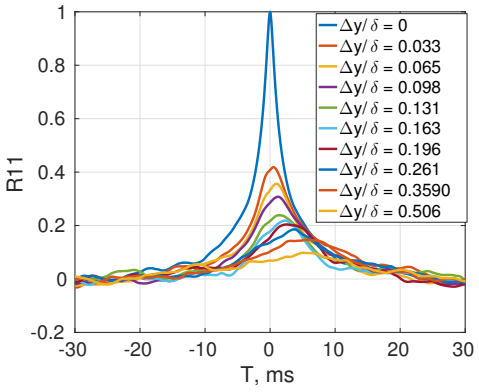

(c) y=4 mm, $y/\delta = 0.1305$.

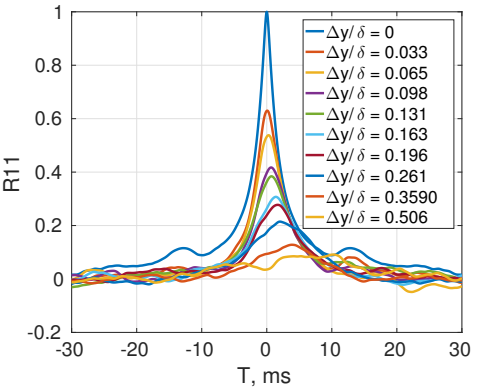

(d) y=8 mm, $y/\delta = 0.2610$.

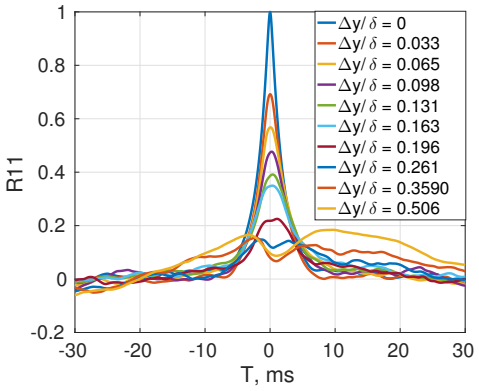

(e) y=16 mm, $y/\delta = 0.5220$.

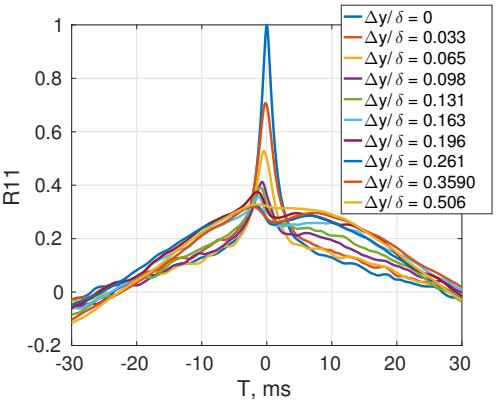

(f) y=24 mm, $y/\delta = 0.7830$.

Figure 3.10: Two-point correlation for different probe separation values in the wall normal direction Case 1. $x/c = 1.0033$.

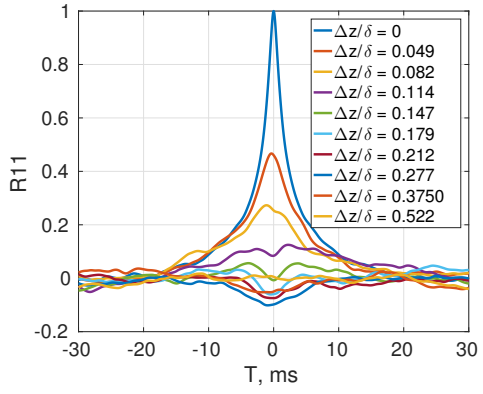

(a) y=2 mm, $y/\delta = 0.0653$.

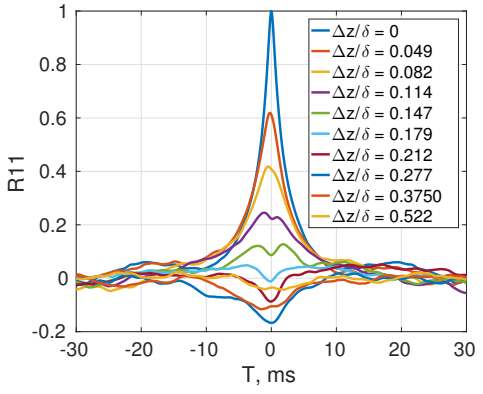

(b) y=4 mm, $y/\delta = 0.1305$.

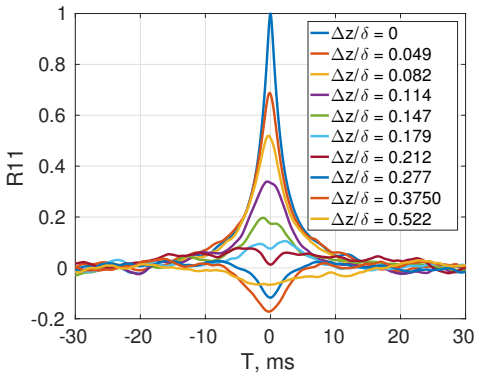

(c) y=8 mm, $y/\delta = 0.2610$.

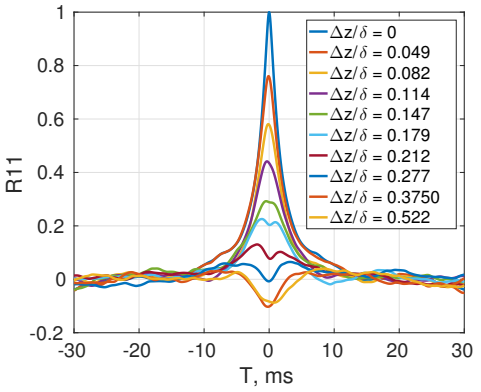

(d) y=16 mm, $y/\delta = 0.5220$.

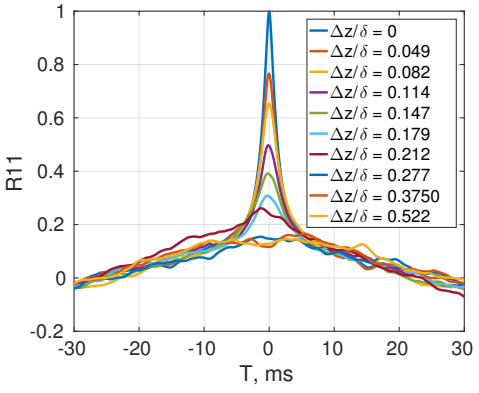

(e) y=24 mm, $y/\delta = 0.7830$.

Figure 3.11: Two-point correlation for different probe separation values in the spanwise direction for Case 1. $x/c = 1.0033$.

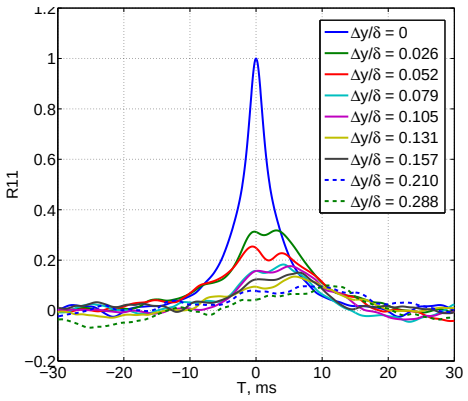

(a) y=0 mm, $y/\delta = 0$.

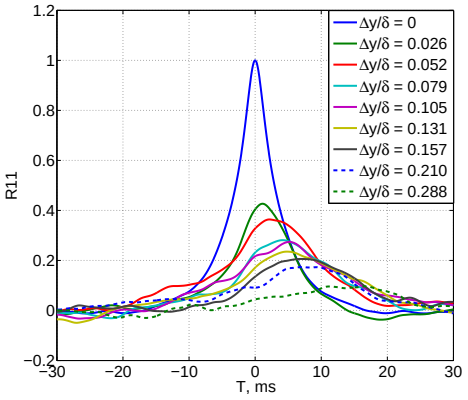

(b) y=0.33 mm, $y/\delta = 0.009$.

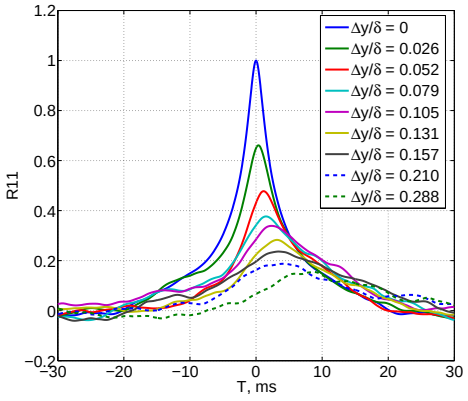

(c) y=1.26 mm, $y/\delta = 0.033$.

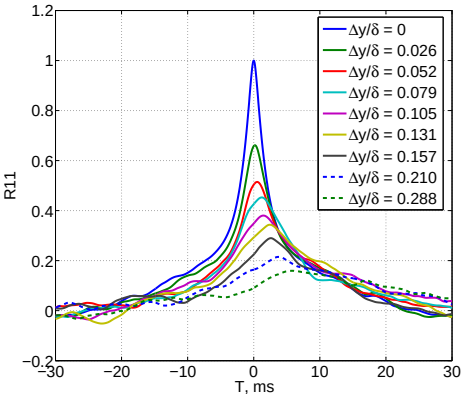

(d) y=2.74 mm, $y/\delta = 0.072$.

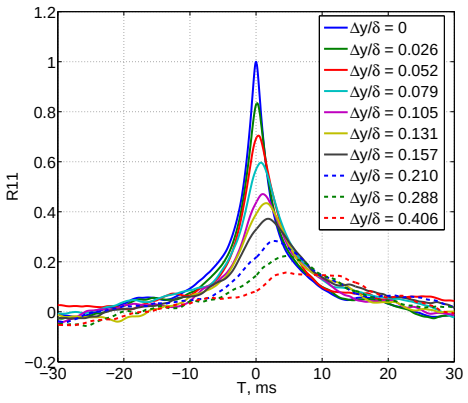

(e) y=8.83 mm, $y/\delta = 0.232$.

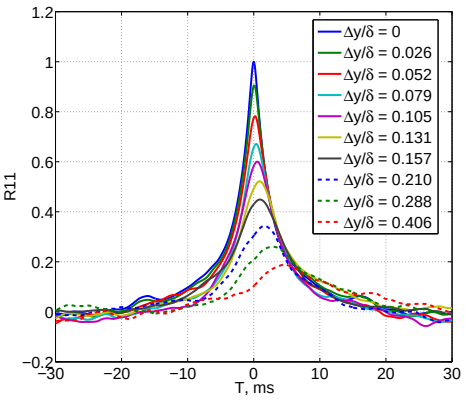

(f) y=14.75 mm, $y/\delta = 0.387$.

Figure 3.12: Two-point correlation for different probe separation values in the wall normal direction for Case 2. $x/c = 1.0033$.

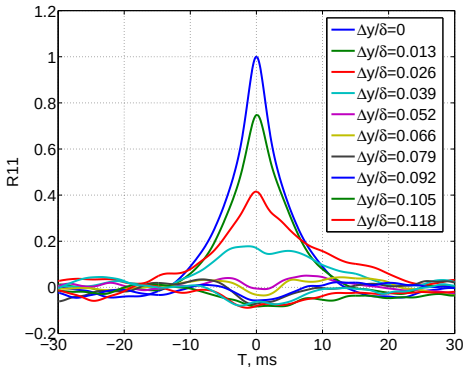

(a) y=0 mm, $y/\delta = 0$.

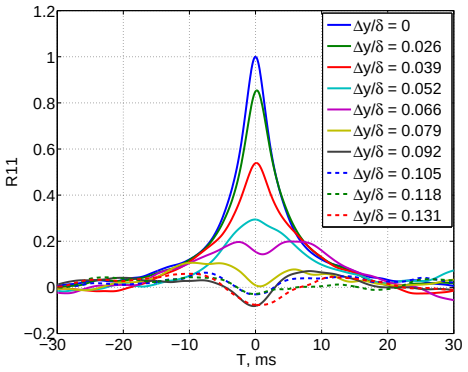

(b) y=0.33 mm, $y/\delta = 0.009$.

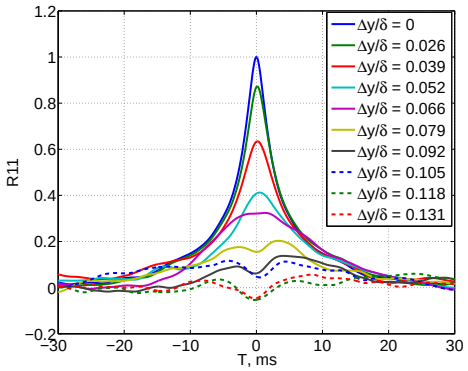

(c) y=1.26 mm, $y/\delta = 0.033$.

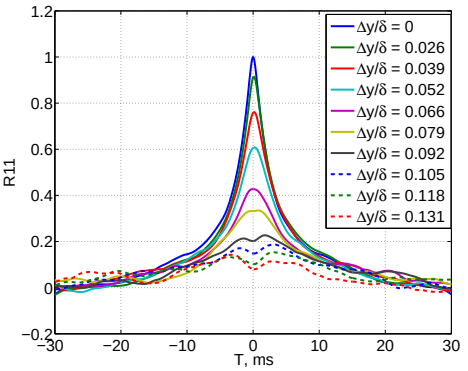

(d) y=2.74 mm, $y/\delta = 0.072$.

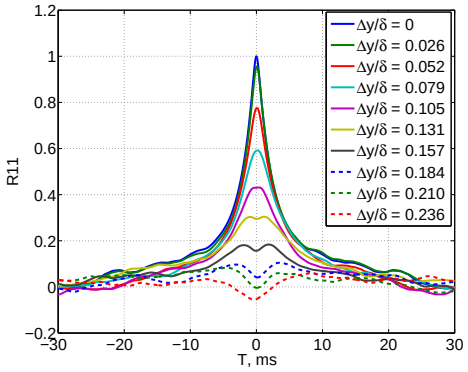

(e) y=8.83 mm, $y/\delta = 0.232$.

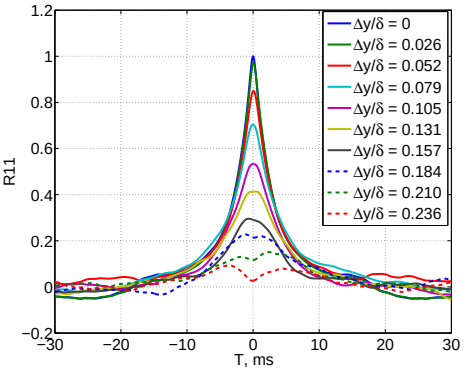

(f) y=14.75 mm, $y/\delta = 0.387$.

Figure 3.13: Two-point correlation for different probe separation values in the spanwise direction for Case 2. $x/c = 1.0033$.

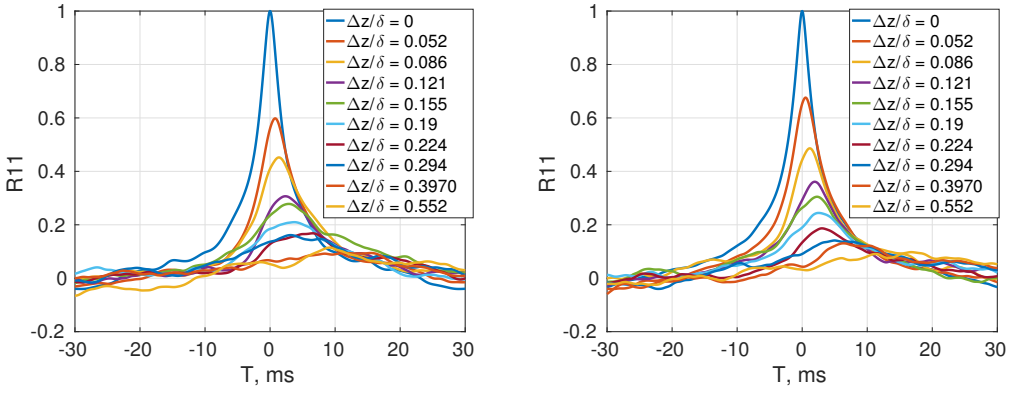

(a) y=1 mm, $y/\delta = 0.0345$. (b) y=2 mm, $y/\delta = 0.0691$.

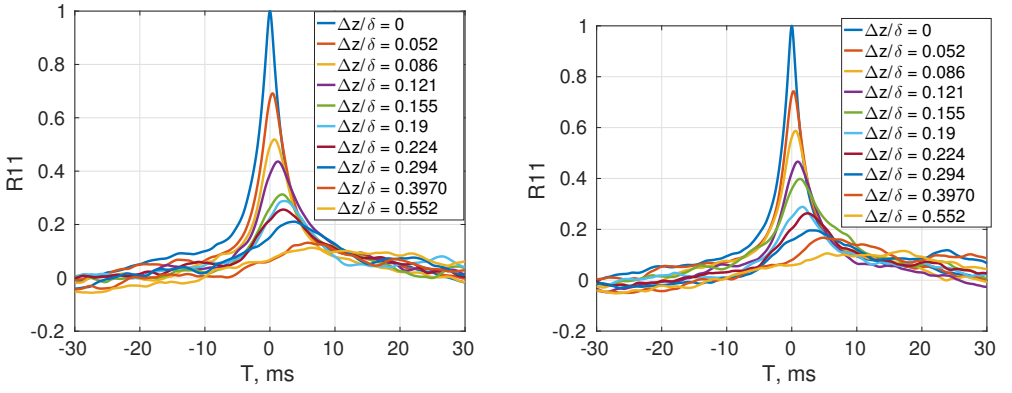

(c) y=4 mm, $y/\delta = 0.1381$. (d) y=8 mm, $y/\delta = 0.2762$.

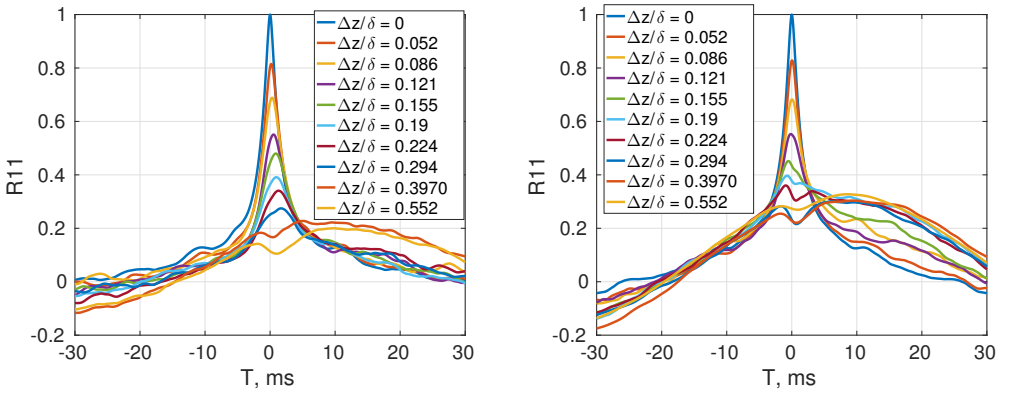

(e) y=16 mm, $y/\delta = 0.5525$. (f) y=24 mm, $y/\delta = 0.8287$.

Figure 3.14: Two-point correlation for different probe separation values in the wall normal direction for Case 3. $x/c = 1.0033$.

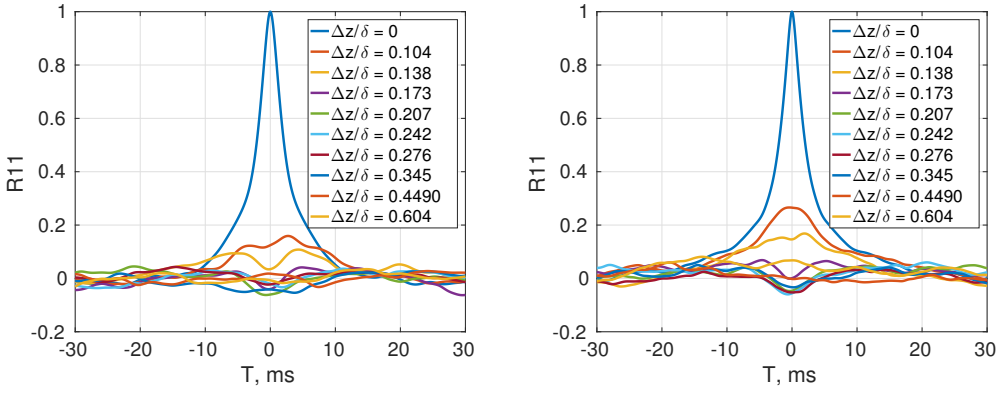

(a) y=1 mm, $y/\delta = 0.0345$.

(b) y=2 mm, $y/\delta = 0.0691$.

(c) y=4 mm, $y/\delta = 0.1381$.

(d) y=8 mm, $y/\delta = 0.2762$.

(e) y=16 mm, $y/\delta = 0.5525$.

(f) y=24 mm, $y/\delta = 0.8287$.

Figure 3.15: Two-point correlation for different probe separation values in the spanwise direction for Case 3. $x/c = 1.0033$.

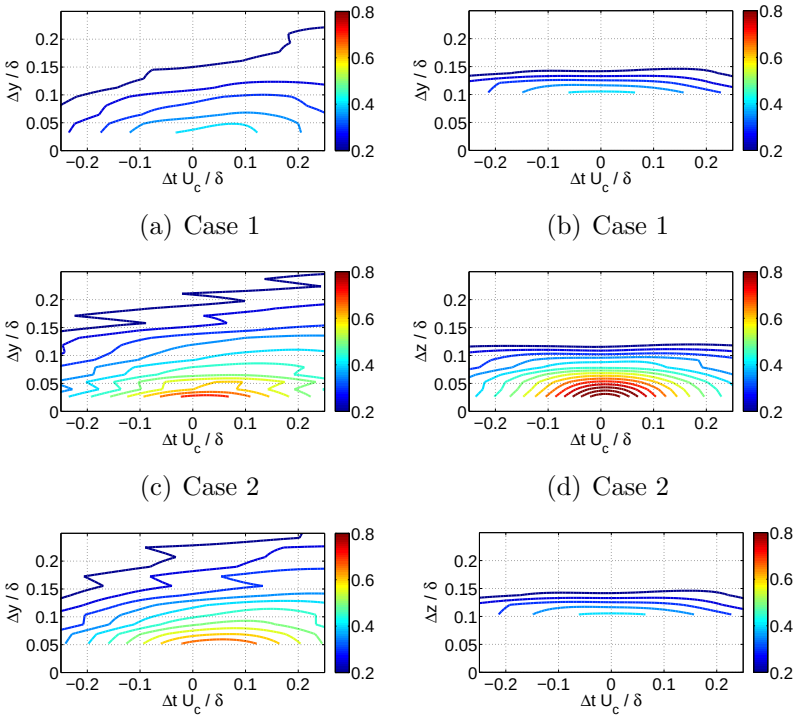

(a) Case 1 (b) Case 1

(c) Case 2 (d) Case 2

(e) Case 3 (f) Case 3

Figure 3.16: Two-point correlation contours at $y^+ \approx 80$. $x/c = 1.0033$.

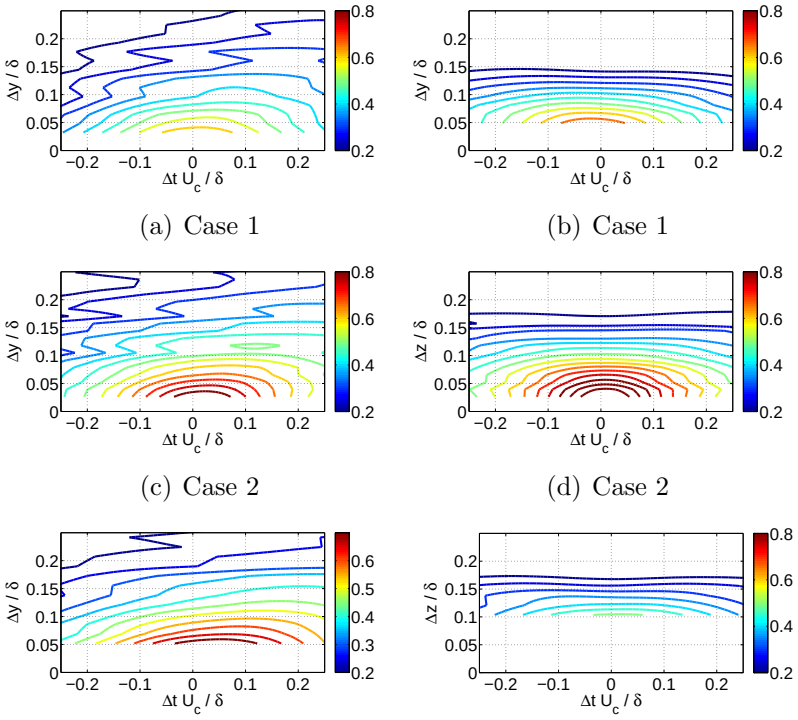

(a) Case 1 (b) Case 1

(c) Case 2 (d) Case 2

(e) Case 3 (f) Case 3

Figure 3.17: Two-point correlation contours at $y/\delta \approx 0.3$. $x/c = 1.0033$.

Kolmogorov scale and ϵ is the turbulence dissipation,

$$\eta = \left(\frac{\nu^3}{\epsilon}\right)^{(1/4)} \tag{3.11}$$

$$\epsilon = 15\nu \int E_{11}(\kappa_1, \mathbf{y_1}, \mathbf{y_1})\kappa_1^2 d\kappa_1 \tag{3.12}$$

The one-dimensional longitudinal velocity spectra at various values of y^+ are plotted with Kolmogorov scaling in Figures 3.18(a) to 3.18(c) and compared to the DNS data of Spalart (1988). When plotted in this manner, the data collapse very well in the range $\kappa_1\eta \geq 0.1$, which is consistent with Kolmogorov's hypothesis. A region of power law behavior is observed between $0.03 \leq \kappa_1\eta \leq 0.1$, however, this region is very small due to the low Reynolds number of the flow. The good collapse of the spectra and the exponential decay observed for $0.1 \leq \kappa_1\eta \leq 1$ implies that the data is well resolved down to wavelengths of the order of the Kolmogorov scale η, and the good agreement with the DNS data of Spalart (1988) provides confidence on the quality of the present data.

3.1.9 Turbulent velocity cross-spectrum

The cross-spectral density function $E_{11}(kappa_1, \mathbf{y_1}, \mathbf{y_2})$ is plotted with Kolmogorov scaling in figure 3.1.9, for a distance to the wall of $y/\delta = 0.23$. This figure is representative of all values of y/δ investigated for both wall-normal and spanwise directions for all test cases, and hence the other cases are omitted. It can be observed that the signal becomes very noisy for $\kappa_1\eta \geq 6 \times 10^{-3}$, indicating that the signals are only correlated in the low frequency range. This is because the structures responsible for the higher frequencies are smaller than the probe separation, causing the signals to decorrelate. The decorrelation begins at lower frequencies as the probe separation increases. To obtain a clearer picture of the correlation of the signals as a function of frequency, the coherence function is investigated.

3.1.10 Coherence function

The coherence function provides a measure of the correlation between signals $u_1(\mathbf{y1})$ and $u_1(\mathbf{y2})$ as a function of frequency. It is defined as,

$$\gamma_{xy}^2 = \frac{|E_{11}(f, u_1(\mathbf{y1}), u_1(\mathbf{y2}))|^2}{|E_{11}(f, u_1(\mathbf{y1}), u_1(\mathbf{y1}))||E_{11}(f, u_1(\mathbf{y2}), u_1(\mathbf{y2}))|} \tag{3.13}$$

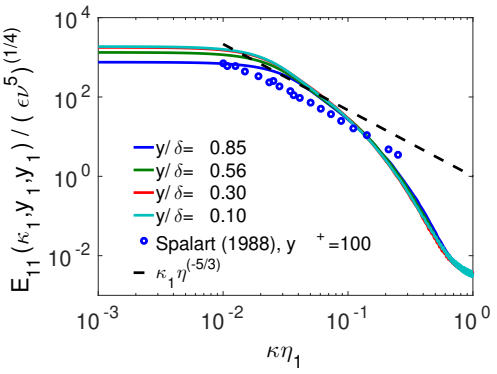

(a) Case 1.

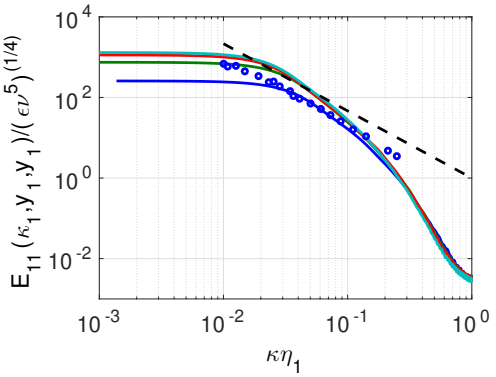

(b) Case 2.

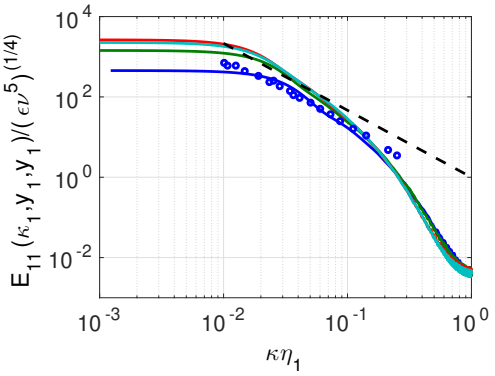

(c) Case 3.

Figure 3.18: One-dimensional longitudinal velocity autospectra normalized by Kolmogorov scales, at various positions in the boundary layer. $x/c = 1.0008$.

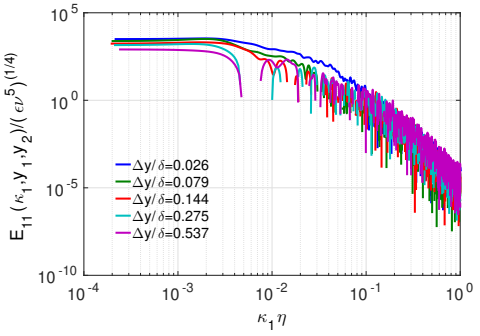

Figure 3.19: Cross-spectral density in the wall-normal direction for Case 2. $y/\delta = 0.23$. $x/c = 1.0033$.

and satisfies for all f,

$$0 \leq \gamma_{xy}^2(f) \leq 1 \tag{3.14}$$

where a value of 0 indicates no correlation and a value of 1 indicates the signals are perfectly correlated.

Figures 3.20(a) and 3.20(b) show the coherence function at $y/\delta = 0.232$ as a function of $\kappa_1\eta$ for various probe separation in the wall-normal and spanwise direction, respectively, for Case 2. The signals are nearly incoherent for a separation of $\Delta y \geq 0.537$, which provides an indication of the size of the average eddy in the wall-normal direction. This was also observed at all other values of y/δ for the two other test cases.

In the spanwise direction, the signals become uncorrelated at smaller distances than for the wall-normal direction, being completely incoherent for $\Delta y \geq 0.275$. This is consistent with what was observed in the two-point correlation contours.

3.2 Summary

In this chapter, an experimental investigation of the flow over two sharp-edged struts has been conducted using hot wire anemometry. Case 1 has been validated against experimental and numerical data from the literature, providing confidence in the experimental technique and equipment used and also providing a bench mark case for comparison with the stronger APG cases.

The parameters investigated include the mean and RMS velocity profiles, probability density functions, third and fourth order moments, spectral density, two-point correlations and coherence function.

It was found that the velocity fluctuations have a Gaussian distribution in the logarithmic region of the boundary layer, but depart from Gaussian in the outer part of the boundary layer.

The longitudinal length scales were found to increase as a function of y/δ, and reach a value in the order of $0.2\delta \leq L_{11} \leq 0.5\delta$ at the edge of the boundary layer, depending on the pressure gradient.

The two-point correlation is also a function of y/δ, with the correlation decreasing faster with probe separation in the spanwise direction than in the wall-normal direction. For all cases, the correlation drops below 0.1 well within one boundary

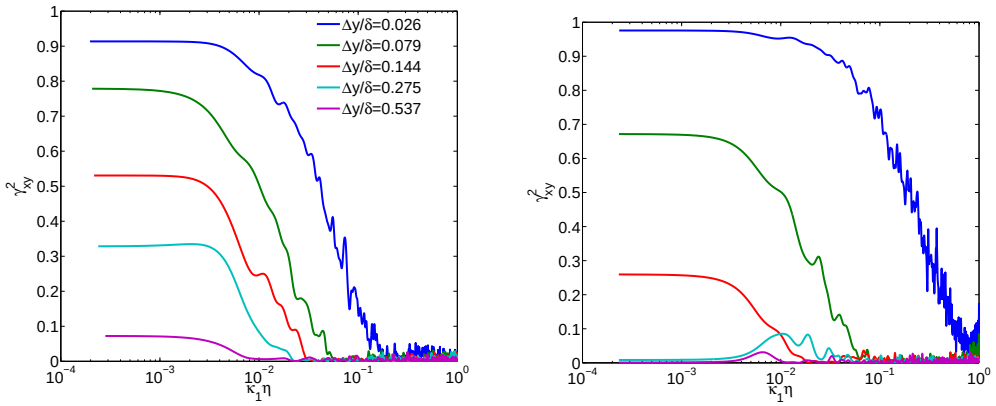

(a) Wall-normal.

(b) Spanwise.

Figure 3.20: Coherence function as a function of $\kappa_1\eta$ for Case 2 at $y/\delta = 0.232$. Measurements taken at $x/c = 1.0033$.

layer thickness. The correlations contours are inclined in the wall-normal direction, but not in the spanwise direction, confirming the observations of Gavin (2002) and supporting his model based on an inclined ellipsoid.

The autospectral density at various values of y/δ collapse into a single curve when plotted with Kolmogorov scaling, and exhibit a power law behavior between $0.03 \leq \kappa_1\eta \leq 0.1$ and a region of exponential decay for $0.1 \leq \kappa_1\eta \leq 1$.

The cross-spectral density exhibits high levels of noise at high $\kappa_1\eta$ for all probe separations $\Delta y/\delta$, which indicates that the signals become incoherent at this high wave numbers. The coherence function confirms this, showing a steep decline for $\kappa_1\eta \geq 10^{-2}$ at all probe separations. The coherence function also confirms that the correlation increases as a function of y/δ, and that the correlation decays faster in the spanwise direction than in the wall normal direction.

The data and insight provided in this experimental investigation can be used as a basis for the development of a cross-spectrum model, which can be used for trailing edge noise prediction with the RSNM method.

Chapter 4

Derivation of the Noise Prediction Method

4.1 Introduction

In this chapter, the derivation of the new RANS-based Statistical Noise Model (RSNM) will be presented. The method uses the theory of Ffowcs Williams and Hall (1970), who used a Green's function approach to calculate the sound intensity in the far field created by a turbulent flow past a sharp trailing edge. The Green's function needs to be tailored to the specific geometry of the problem. For the case of a sharp, straight trailing edge, the rigid half plane Green's function is used. When a tailored Green's function is used, the far field pressure fluctuations can be obtained by a convolution of the source terms with the Green's function. However, the source terms are not known and, as was discussed in Chapter 1, using DNS or LES is often impractical due to the large computational resources required. A more practical approach is to use a model for the source terms based on time averaged RANS data. A derivation of the method is provided below.

4.2 Model derivation

? combined the momentum and continuity equations and rearranged them in a form equivalent to a an inhomogeneous wave equation, that is, and equation that describes the propagation of sound in a uniform medium due to externally applied fluctuating stresses. This is known as Lighthill's acoustic analogy. Lighthill's equation is given

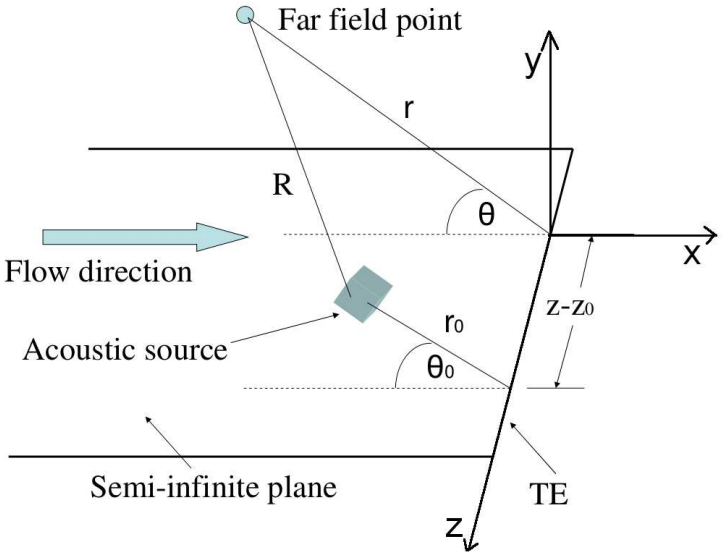

Figure 4.1: The coordinate system, with the origin at the trailing edge, used by Ffowcs Williams and Hall (1970).

by

$$\nabla^2\rho - \frac{1}{c^2}\frac{\partial^2\rho}{\partial t^2} = \frac{1}{c^2}\frac{\partial^2}{\partial x_i \partial x_j}(\rho u_i u_j + p_{ij} - c^2\rho\delta_{ij}), \tag{4.1}$$

where ρ is the fluid density, (u_1, u_2, u_3) is the velocity vector, p_{ij} is the compressive stress tensor and c is the speed of sound in an undisturbed fluid. By neglecting viscous effects ($p_{ij} = p\delta_{ij}$, where p is the isotropic pressure) and assuming that the changes in p are exactly balanced by changes in $c^2\rho$, Lighthill's equation becomes

$$\nabla^2 p - \frac{1}{c^2}\frac{\partial^2 p}{\partial t^2} = -\frac{\partial^2}{\partial x_i \partial x_j}(\rho u_i u_j). \tag{4.2}$$

Defining the Fourier transform f^* of f as

$$f^*(\omega) = \frac{1}{2\pi}\int_{-\infty}^{\infty} f(t)e^{i\omega t}dt, \tag{4.3}$$

Lighthill's equation can be written in frequency space as the inhomogeneous Helmholz equation,

$$\nabla^2 p^* - k_a^2 p^* = -\left[\frac{\partial^2}{\partial x_i \partial x_j}(\rho u_i u_j)\right]^*, \tag{4.4}$$

where $k_a = \omega/c$ is the acoustic wavenumber, and ω is the angular frequency. Ffowcs Williams and Hall (1970) showed that, in the presence of a rigid half-plane,

the solution is given by

$$4\pi p^*(\mathbf{x_o},\omega) = \int (\rho u_i u_j)^* \frac{\partial^2 G}{\partial u_i \partial u_j} dV(\mathbf{y}), \tag{4.5}$$

where $\mathbf{x_o} = (x_1, x_2, x_3)$ is the location of the observer, $\mathbf{y}(r_0, \theta_0, z)$ is the position of the source, u_i are the velocity components with $i = 1, 2, 3$, and G is a Green's function tailored to the boundary conditions of the problem. Changing to cylindrical polar coordinates, Equation 4.5 becomes:

$$\begin{aligned} 4\pi p^*(\mathbf{x},\omega) = \int \Bigg\{ & \rho u_r^2 \frac{\partial^2 G}{\partial r_0^2} + \rho u_z^2 \frac{\partial^2 G}{\partial z_0^2} + \rho u_r u_z \left[\frac{\partial}{\partial r_0}\left(\frac{\partial G}{\partial z_0}\right) + \frac{\partial}{\partial z_0}\left(\frac{\partial G}{\partial r_0}\right)\right] \\ & + \rho u_r u_\theta \left[\frac{\partial}{\partial r_0}\left(\frac{1}{r_0}\frac{\partial G}{\partial z_0}\right) + \frac{2}{r_0}\frac{\partial}{\partial \theta_0}\left(\frac{\partial G}{\partial r_0}\right) - \frac{1}{r_0^2}\frac{\partial G}{\partial \theta_0}\right] \\ & + \rho u_r u_\theta \left[\frac{\partial}{\partial r_0}\left(\frac{1}{r_0}\frac{\partial G}{\partial z_0}\right) + \frac{2}{r_0}\frac{\partial}{\partial \theta_0}\left(\frac{\partial G}{\partial r_0}\right) - \frac{1}{r_0^2}\frac{\partial G}{\partial \theta_0}\right] \\ & + \rho u_{\theta^2} \left(\frac{1}{r_0^2}\frac{\partial^2 G}{\partial \theta^2} + \frac{1}{r_0}\frac{\partial G}{\partial r_0}\right) \Bigg\}^* dV_0 \end{aligned} \tag{4.6}$$

where $\mathbf{x} = (r, \theta, z)$ is the position of the observer, $dV_0 = r_0 dr_0 d\theta_0 dz_0$, and r_0, θ_0 and z_0 are the coordinates of the source point $\mathbf{y}$ in the cylindrical coordinate system of figure 4.1. Ffowcs Williams and Hall (1970) used the Green's function provided by Macdonald (1915),

$$G(r,\theta,\omega) = \frac{e^{-ik_a R}}{R}\left\{1 + \frac{2e^{i\pi/4}}{\sqrt{\pi}}(2k_a r_0 \sin\phi)^{\frac{1}{2}} cos\frac{1}{2}\theta + O(k_a r_0)\right\} \tag{4.7}$$

where R is the distance between the source and the observer, $O(k_a r_0)$ is an error term of the order of $k_a r_0$, r_0 is the distance from the edge to the source and (r, θ) are the cylindrical coordinates of the observer, as shown in Figure 4.1. The angle ϕ is defined as

$$\sin\phi = \frac{r}{\sqrt{r^2 + (z - z_0)^2}}. \tag{4.8}$$

Using the expression for G given by equation 4.7, Equation 4.6 becomes

$$\begin{aligned} -4\pi p^*(\mathbf{x},\omega) = & k_a^2 \frac{2e^{i\pi/4}}{\sqrt{\pi}}(\sin(\phi))^{\frac{1}{2}} \cos(\frac{1}{2}\theta) \\ & \times \int H \times (2k_a r_0)^{-\frac{3}{2}} \frac{e^{-ik_a R}}{R} dV_0, \end{aligned} \tag{4.9}$$

where

$$H = \left\{ \rho u_r^2 \cos(\frac{1}{2}\theta_0) - \rho u_\theta^2 \cos(\frac{1}{2}\theta_0) - 2\rho u_r u_\theta \sin(\frac{1}{2}\theta_0) \right\}^*, \tag{4.10}$$

Following Ffowcs Williams and Hall (1970), the following approximations are made:

$$\begin{aligned} (u_r^2)^* &\approx 2\bar{U}_r u_r'^* \\ (u_\theta^2)^* &\approx 2\bar{U}_\theta u_\theta'^* \\ (u_r u_\theta)^* &\approx \bar{U}_r u_\theta'^* + \bar{U}_\theta u_r'^*, \end{aligned} \tag{4.11}$$

where the overbar denotes the time average and the prime denotes the fluctuating component as in a Reynolds decomposition ($u = \bar{U} + u'$). A further simplification is made by assuming the fluctuating velocity components are related to each other by an anisotropy factor f_a, so that

$$u_\theta'^* = f_a u_r'^*. \tag{4.12}$$

As a starting point, isotropic turbulence is assumed, resulting in $f_a = 1$. All results presented in this thesis use $f_a = 1$. However, this assumption is not necessary and can be relaxed. The contribution of source point $\mathbf{y}$ to the far field pressure becomes

$$\begin{aligned} -4\pi p^*(\mathbf{x},\omega) = k_a^2 \frac{2e^{i\pi/4}}{\sqrt{\pi}} (\sin(\phi))^{\frac{1}{2}} \cos(\frac{1}{2}\theta) \\ \times \int 2\rho_0 u_r'^*(\mathbf{y}) F(\mathbf{y}) (2k_a r_0)^{-\frac{3}{2}} \frac{e^{-ik_a R}}{R} dV(\mathbf{y}), \end{aligned} \tag{4.13}$$

where

$$F(\mathbf{y}) = \left\{ (\bar{U}_r - f_a \bar{U}_\theta) \cos(\frac{1}{2}\theta_0) - (f_a \bar{U}_r + \bar{U}_\theta) \sin(\frac{1}{2}\theta_0) \right\}. \tag{4.14}$$

By making the far field approximation, $R(\mathbf{y_1}) \approx R(\mathbf{y_2}) \approx R$, the power spectral density of the far field pressure can be written as

$$\begin{aligned} S(\mathbf{x},\omega) &= \langle p^*(\mathbf{x},\omega) \hat{p}^*(\mathbf{x},\omega) \rangle \\ &= \int\int \Psi E_{rr} \frac{F(\mathbf{y_1})}{r_0(\mathbf{y_1})^{3/2}} \frac{F(\mathbf{y_2})}{r_0(\mathbf{y_2})^{3/2}} dV(\mathbf{y_1}) dV(\mathbf{y_2}), \end{aligned} \tag{4.15}$$

where $\hat{p}^*$ is the complex conjugate of p^*,

$$\Psi = \frac{\rho_0^2 \omega \sin\phi \cos^2\frac{\theta}{2}}{8\pi^3 c R^2} \tag{4.16}$$

and

$$E_{rr}(\mathbf{y_1}, \mathbf{y_2}, \omega) = \langle u_r'^*(\mathbf{y_1}) \hat{u}_r'^*(\mathbf{y_2}) \rangle \,. \tag{4.17}$$

The only unknown in the power spectral density is the cross-spectrum of the turbulent velocity, $E_{rr}(\mathbf{y_1}, \mathbf{y_2}, \omega)$. A cross-spectrum model is required to estimate the noise spectrum.

4.2.1 Cross-spectrum model

We begin by defining the turbulent velocity cross-correlation function in a fixed reference frame as

$$R_{rr}(\mathbf{y_1}, \xi, \tau) = \langle u_r'(\mathbf{y_1}, t) u_r'(\mathbf{y_2}, t + \tau) \rangle, \tag{4.18}$$

where $\langle\rangle$ is the ensemble average and $\xi = |\mathbf{y_2} - \mathbf{y_1}|$.

We use a Gaussian formulation originally developed for jet noise predictions by Morris and Farassat (2002),

$$R_{rr}(\mathbf{y_1}, \xi, \tau) = A_0 u_s^2 \exp\left(-\frac{|\xi|^2}{\ell_s^2} - \omega_s^2 \tau^2 \right), \tag{4.19}$$

where ℓ_s is a characteristic length scale, ω_s is a characteristic frequency, u_s is a velocity scale that characterises the velocity fluctuations and A_0 is an empirical scalar value that determines the magnitude of the correlation. Converting to a cross-spectrum we have,

$$E_{rr}(\mathbf{y_1}, \xi, \omega) = \int_{-\infty}^{\infty} A_0 u_s^2 \exp\left(-\frac{|\xi|^2}{\ell_s^2} - \omega_s^2 \tau^2 \right) \exp(i\omega\tau) d\tau. \tag{4.20}$$

Using the following property of exponential functions,

$$\int_{-\infty}^{\infty} \exp\left[-(a\tau^2 + b\tau + c) \right] d\tau = \sqrt{\frac{\pi}{a}} \exp\left[\frac{b^2 - 4ac}{4a} \right], \tag{4.21}$$

the turbulent velocity cross-spectrum becomes

$$E_{rr}(\mathbf{y_1}, \xi, \omega) = \frac{A_0 \sqrt{\pi}}{\omega_s} u_s^2 \exp\left(-\frac{|\xi|^2}{\ell_s^2} \right) \exp\left(-\frac{\omega^2}{4\omega_s^2} \right). \tag{4.22}$$

For the remainder of this thesis, 4.22 will be referred to as the baseline model. To link this model to a CFD solution (i.e. RANS calculated turbulence data), the

following relations are used (Morris and Farassat 2002):

$$u_s = \sqrt{2k/3}, \;\; \omega_s = 2\pi/\tau_s, \;\; \tau_s = c_\tau k/\epsilon, \;\; \ell_s = c_\ell k^{3/2}/\epsilon, \tag{4.23}$$

where k and ϵ are the turbulent kinetic energy and the turbulent dissipation, which are calculated at each acoustic source location $\mathbf{y}$, and c_τ and c_ℓ are semi-empirical parameters.

4.3 Alternative cross-spectrum models

As a starting point, consider a cross-spectrum of the form

$$E_r r(\mathbf{y_1}, \mathbf{y_2}, \omega) = A_0 f_1(\mathbf{y_1}, \mathbf{y_2}) f_2(\omega, \mathbf{y_1}, \mathbf{y_2}), \tag{4.24}$$

When written in this form, it is possible to modify the functions f_1 and f_2 to arrive at alternative models.

Consider the coherence function, which provides a measure of the correlation between signals $\hat{u}'^*(\mathbf{y_1}, \omega)$ and $\hat{u}'^*(\mathbf{y_2}, \omega)$ as a function of frequency. It is defined as

$$\gamma^2_{rr}(\mathbf{y_1}, \mathbf{y_2}, \omega) = \frac{|E_{rr}(\mathbf{y_1}, \mathbf{y_2}, \omega)|^2}{|E_{rr}(\mathbf{y_1}, \mathbf{y_1}, \omega)||E_r r(\mathbf{y_2}, \mathbf{y_2}, \omega)|}, \tag{4.25}$$

The coherence function satisfies for all ω,

$$0 \leq \gamma^2_{rr}(\omega) \leq 1. \tag{4.26}$$

For modelling purposes, f_1 can be thought of as the square root of the coherence function at zero frequency,

$$f_1(\mathbf{y_1}, \mathbf{y_2}) = \gamma_{rr}(\mathbf{y_1}, \mathbf{y_2}, \omega = 0) \tag{4.27}$$

while f_2 can be considered as the square root of the product of the autospectra of $u'^*_r(\mathbf{y_1})$ and $u'^*_r(\mathbf{y_2})$,

$$f_2(\mathbf{y_1}, \mathbf{y_2}, \omega) = \sqrt{E_{rr}(\mathbf{y_1}, \mathbf{y_1}, \omega) E_{rr}(\mathbf{y_2}, \mathbf{y_2}, \omega)}. \tag{4.28}$$

This results in a cross-spectrum model of the form

$$|E_{rr}(\mathbf{y_1}, \mathbf{y_2})| \approx \gamma_{rr}(\mathbf{y_1}, \mathbf{y_2}, \omega = 0) \sqrt{E_{rr}(\mathbf{y_1}, \mathbf{y_1}) E_{rr}(\mathbf{y_2}, \mathbf{y_2})} \tag{4.29}$$

Neglecting the frequency dependency of the coherence function will introduce some degree of error into the model. To test this assumption, equation 4.29 is compared to the measured cross-spectrum for Case 2 at $y/\delta = 0.13$. As shown in Figures 4.2(a)and 4.2(b), the assumption works well for small distances $\xi = |\mathbf{y_1} - \mathbf{y_2}|$. However, when ξ is increased, the assumption only works well for frequencies below 100 Hz, and the agreement deteriorates at higher frequencies, where equation 4.29 decays much more slowly than the experimental data. Since most of the energy is contained in the lower frequencies, and the amplitude of the cross-spectrum decays rapidly with increasing ξ, these discrepancies are not expected to have a large effect in the noise prediction capabilities of the model. This assumption will be further examined in Chapter **??**.

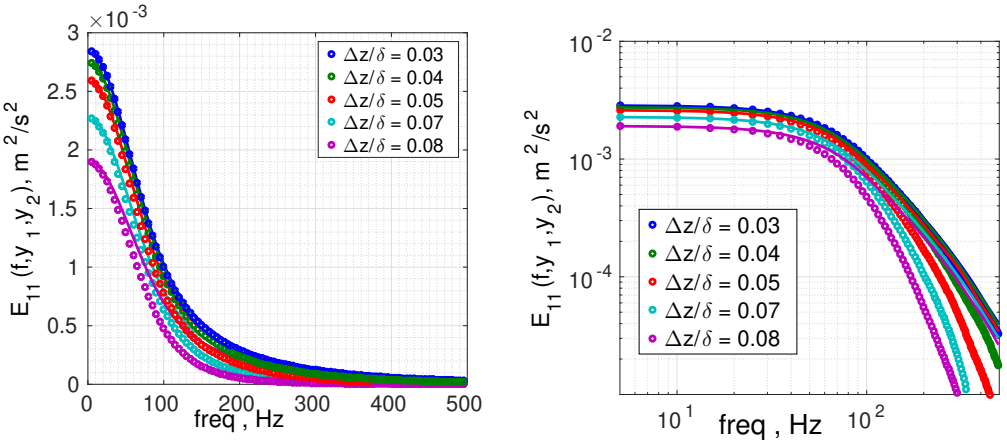

(a) (b)

Figure 4.2: Measured cross-spectrum (circles) and cross-spectrum calculated using equation 4.29 (solid lines) for Case 2 at $y/\delta = 0.13$.

4.4 Spatial coherence models

In this section, two alternative models for the spatial coherence $\gamma^2_{rr}(\mathbf{y_1}, \mathbf{y_2}, \omega = 0)$ are presented, namely, the simplified anisotropic model of Gavin (2002) and an empirical model based on the experimental measurements conducted as part of this research.

4.4.1 Gavin's Simplified Anisotropic Model (SAM)

Gavin's measurements (Gavin 2002) show that a turbulence velocity correlation volume can be modelled as an ellipsoid inclined at an angle θ to the wall. He then proceeds to map the ellipsoid onto a sphere and applies isotropic turbulence theory to close the model. First, the distance between two points in the boundary layer is defined as

$$r = \sqrt{(x_1 - x_2)^2 + (y_1 - y_2)^2 + (z_1 - z_2)^2}. \tag{4.30}$$

Then the coordinate system is rotated into the major/minor-axis coordinate frame of the ellipsoid by applying the following transformation matrix:

$$\zeta = \begin{bmatrix} \cos(\theta) & -\sin(\theta) & 0 \\ \sin(\theta) & \cos(\theta) & 0 \\ 0 & 0 & 1 \end{bmatrix} \begin{bmatrix} (x_2 - x_1) \\ (y_2 - y_1) \\ (z_2 - z_1) \end{bmatrix}. \tag{4.31}$$

Then the major/minor coordinate axes are scaled onto the axes of a sphere by

$$r^\star = \sqrt{\left(\frac{\zeta_1}{\Upsilon_1}\right)^2 + \left(\frac{\zeta_2}{\Upsilon_2}\right)^2 + \left(\frac{\zeta_3}{\Upsilon_3}\right)^2}. \tag{4.32}$$

Using this radius, classical isotropic turbulence theory (Pope 2000) states that

$$\gamma_{ij}(\zeta_1, \zeta_2, \zeta_3) = \frac{r_i^\star r_j^\star}{r^{\star 2}} \left[f(r^\star) - g(r^\star)\right] + \delta_{ij} g(r^\star), \tag{4.33}$$

where $r^\star = \mathbf{e_1} r^\star$ and

$$f(r^\star) = \exp\left(\frac{-r^\star}{\Lambda_f}\right) \qquad g(r^\star) = \left(1 - \frac{r^\star}{2\Lambda_f}\right) f(r^\star). \tag{4.34}$$

The scalar Λ_f is the correlation length. Gavin defined this parameter as $\Lambda_f = 0.35\delta$, where δ is the boundary layer thickness. All SAM model parameters are shown in Table 4.1. Gavin's model is designed for the outer parts of the boundary layer. RSNM requires the correlation function through the entire boundary layer, where Gavin's model does not apply. Peltier and Hambric (2007) extended the model to the inner and intermediate parts of the boundary layer by replacing the global correlation length Λ_f with a local correlation length scale $\ell = k^{(3/2)}/\epsilon$ obtained from RANS.

Since we are only interested in one component of the velocity fluctuations(due to

our asumption of isotropic turbulence, $f_a = 1$, equation 4.33 can be reduced to

$$\gamma_{11}(\zeta_1, \zeta_2, \zeta_3) = f(r^\star). \tag{4.35}$$

4.4.2 Proposed semi-empirical model

A semi-empirical model for $\gamma_{11}(\mathbf{y_1}, \mathbf{y_2}, \omega = 0)$ is presented, based on the experimental measurements conducted during this research.

The fundamental assumption is made that $\gamma_{11}(\mathbf{y_1}, \mathbf{y_2}, \omega = 0)$ can be separated into orthogonal components,

$$\gamma_{11}(\mathbf{y_1}, \mathbf{y_2}, \omega = 0) = \gamma_x(\Delta x)\gamma_y(\Delta y)\gamma_z(\Delta z), \tag{4.36}$$

where the explicit dependency of γ_x, γ_y and γ_z on $(\mathbf{y_1}, \mathbf{y_2}, \omega = 0)$ has been omitted to simplify the notation, and

$$\begin{aligned} \Delta x &= (x_2 - x_1) \\ \Delta y &= (y_2 - y_1) \\ \Delta z &= (z_2 - z_1), \end{aligned} \tag{4.37}$$

and x, y, z are the streamwise, wall normal and spanwise directions, respectively. Based on this assumptions, a model for each component is presented,

Table 4.1: Gavin's SAM model parameters

θ	Υ_1	Υ_2	Υ_3	Λ_f
20	1.000	0.700	0.520	0.35δ

$$\begin{aligned}\gamma_x^2 &= \exp\left(\frac{-\Delta x}{2L_x}\right)\\ \gamma_y^2 &= \exp\left(\frac{-\Delta y}{2L_y}\right)\\ \gamma_z^2 &= \exp\left(\frac{-\Delta z^2}{2L_z^2}\right),\end{aligned} \tag{4.38}$$

where

$$\begin{aligned}L_x &= c_{\ell_x} k^{3/2}/\epsilon\\ L_y &= c_{\ell_y} k^{3/2}/\epsilon\\ L_z &= c_{\ell_z} k^{3/2}/\epsilon.\end{aligned} \tag{4.39}$$

The empirical coefficients c_{ℓ_x} c_{ℓ_y} and c_{ℓ_z} are calculated and tabulated in the following sections.

4.4.2.1 Dependency on spatial separation in the wall-normal direction.

Figure 4.3(a) shows $\gamma_y^2(\Delta y)$ and an exponential curve fitted to the data by a least squares approach for Case 2. The wall-normal distance of the reference probe is $y_1/\delta = 0.39$. The same procedure was employed for a range of fixed probe positions y_1/δ. The data is well represented by:

$$\gamma_y^2 = \exp\left(-\frac{\Delta y}{L_y}\right) \tag{4.40}$$

where the $L_y = c_{\ell_y} k^{3/2}/\epsilon$ is a length scale in the wall normal direction and c_{ℓ_y} is an empirical length scale coefficient. The length scale coefficient c_{ℓ_y} is calculated for each position in the boundary layer and shown in Figure 4.3(b), and a function of the form

$$c_{\ell_y} = m\frac{|\Delta y|}{\delta} + n \tag{4.41}$$

has been fitted to the data.

The same procedure was applied Cases 1 and 3, and the results for a similar value of y/δ are shown in Figures 4.4(a) and 4.4(b) for Case 1, and 4.5(a) to 4.5(b) for

Case 3. The resulting empirical coefficients m and n for each case are summarized in table 4.2.

Results at other y_1/δ positions are provided in section A, Figures A.1(a) to A.1(k); A.2(a) to A.2(e); and A.3(a) to A.3(e) for Cases 2, 1 and 3, respectively.

4.4.2.2 Dependency on spatial separation in the spanwise direction.

With a similar process as for the wall-normal case, the spanwise coherence was measured at various distances from the wall, ranging from $y/\delta = 0$ to $y/\delta = 0.8$, and a curve fitting procedure was employed to determine the functional dependency of the coherence function on spatial separation. It was found that the data are well represented by a Gaussian function of spatial separation, given by:

$$\gamma_z^2 = \exp\left(-\frac{\Delta z^2}{L_z^2}\right) \tag{4.42}$$

where

$$L_z = \frac{c_{\ell_z} k^{3/2}}{\epsilon} \tag{4.43}$$

where c_{ℓ_z} is an empirical parameter, which appears to be a function of distance to the wall.

Figures 4.6(a), 4.7(a) and 4.8(a) show the measured spanwise coherence function and the Gaussian curve fit at $y/\delta = 0.39$ for Cases 2, 1 and 3, respectively. The Gaussian behavior of the spanwise coherence function is evident. The empirical parameter c_{ℓ_z} is shown in Figures 4.6(b), 4.7(b) and 4.8(b). Similar results were obtained at other positions in the boundary layer for all cases, and are shown in Appendix A.

4.4.2.3 Dependency on spatial separation in the streamwise direction.

Due to probe interference effects, $\gamma_x(\Delta x)$ could not be measured directly, but it was estimated from the autocorrelation function R_{11},

$$\gamma_x(\mathbf{y}, \Delta x) \approx R_{11}(\Delta x) \tag{4.44}$$

Taylor's hypothesis of frozen turbulence is used here to estimate R_{11} as

$$R_{11}(\Delta x) \approx R_{11}(U_c \tau) \tag{4.45}$$

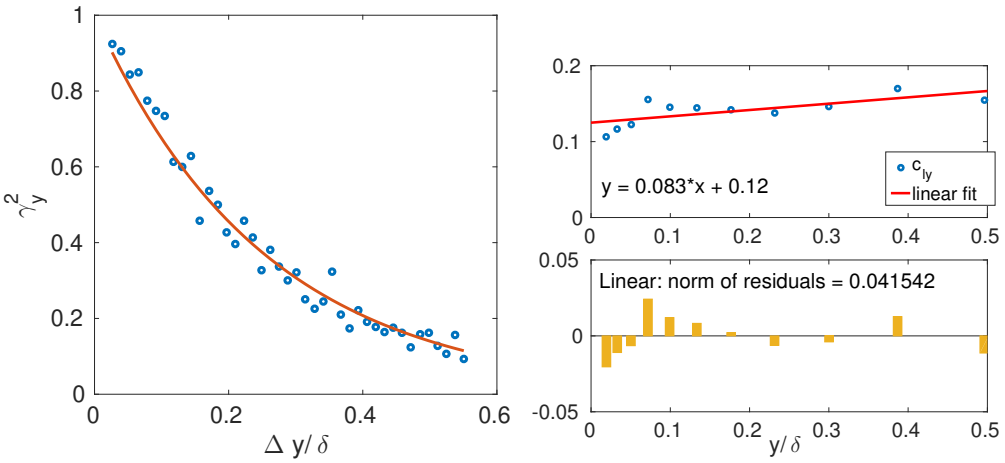

(a) Wall-normal coherence (b) length scale coefficient c_{ℓ_y}

Figure 4.3: a)Wall-normal coherence at $y/\delta = 0.39$. b) length scale coefficient c_{ℓ_y} as function of distance to the wall. Data taken at 1 mm downstream of the TE for Case 2. Results for other values of y/δ, and their corresponding exponential fits are shown in Figures A.1(a) to A.1(k).

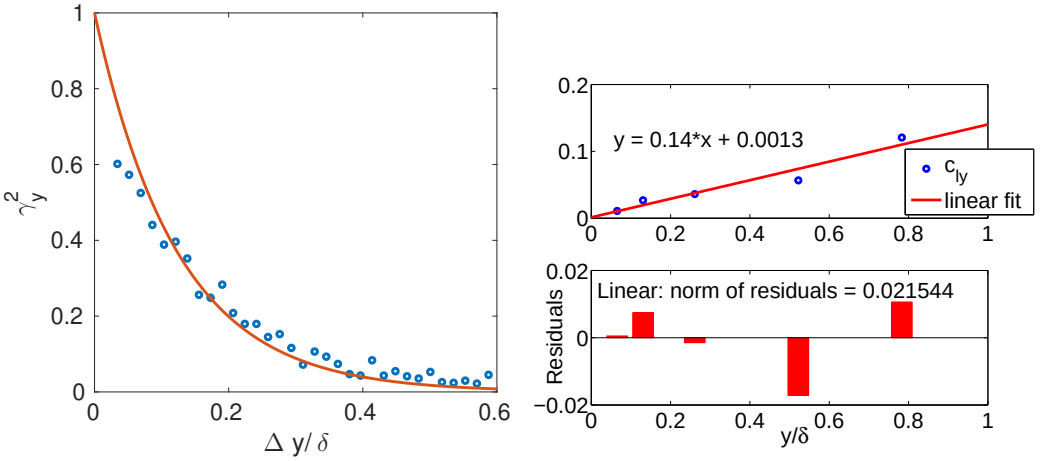

(a) Wall-normal coherence (b) length scale coefficient c_{ℓ_y}

Figure 4.4: a)Wall-normal coherence at $y/\delta = 0.55$. b) length scale coefficient c_{ℓ_y} as function of distance to the wall. Data taken at 1 mm downstream of the TE for Case 1. Results for other values of y/δ, and their corresponding exponential fits are shown in Figures A.2(a) to A.2(e).

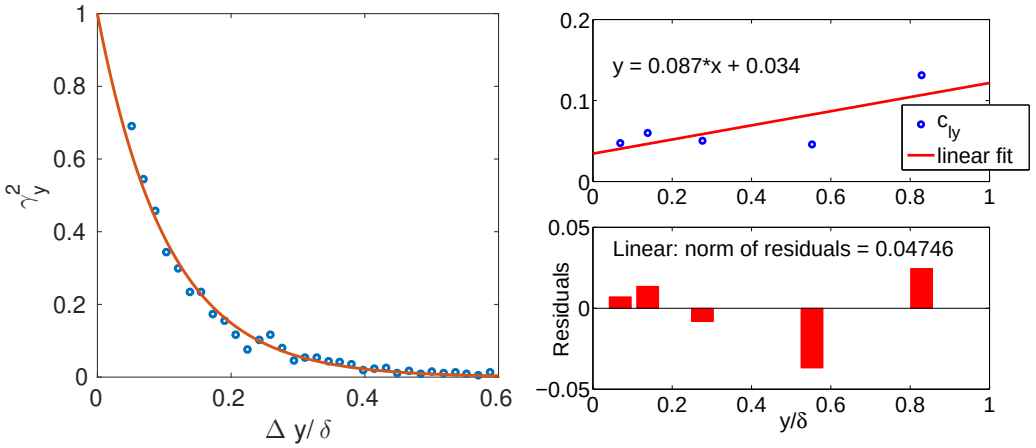

(a) Wall-normal coherence (b) length scale coefficient c_{ℓ_y}

Figure 4.5: a)Wall-normal coherence at $y/\delta = 0.39$. b) length scale coefficient c_{ℓ_y} as function of distance to the wall. Data taken at 1 mm downstream of the TE for Case 3. Results for other values of y/δ are shown in Figures A.3(a) to A.3(e).

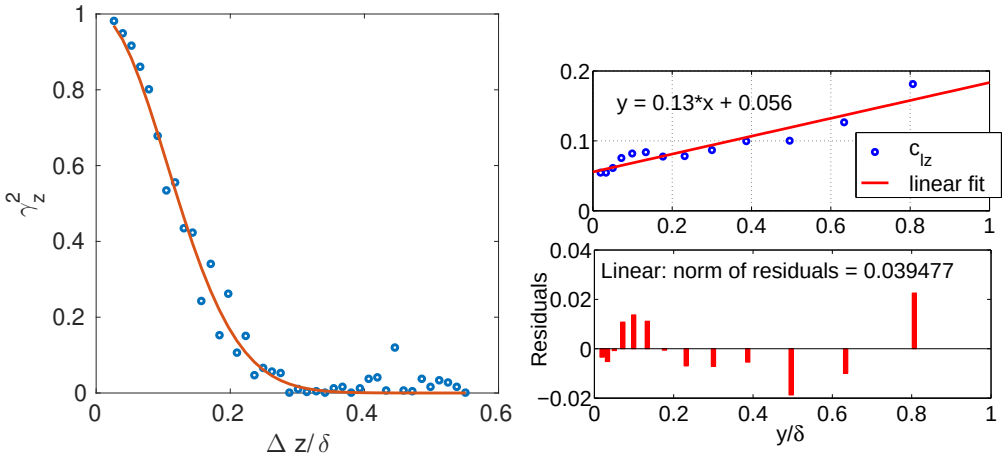

(a) Spanwise coherence (b) Empirical parameter c_{ℓ_z}

Figure 4.6: a) Spanwise coherence for at $y/\delta = 0.39$. b) Empirical parameter c_{ℓ_z}, linear fit and residuals. Data taken at 1 mm downstream of the TE for Case 2.

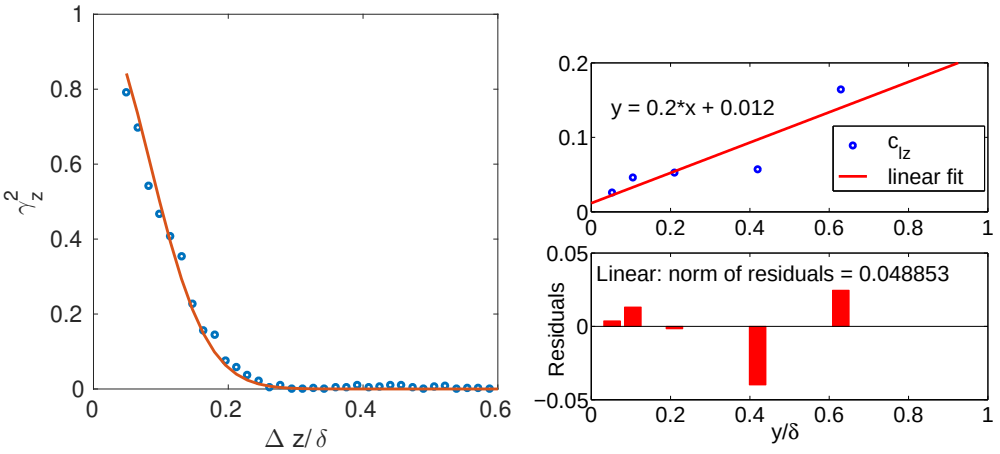

(a) Spanwise coherence (b) Empirical parameter c_{ℓ_z}

Figure 4.7: a) Spanwise coherence for $y/\delta = 0.52$. b) Empirical parameter c_{ℓ_z}, linear fit and residuals. Data taken at 1 mm downstream of the TE for Case 1.

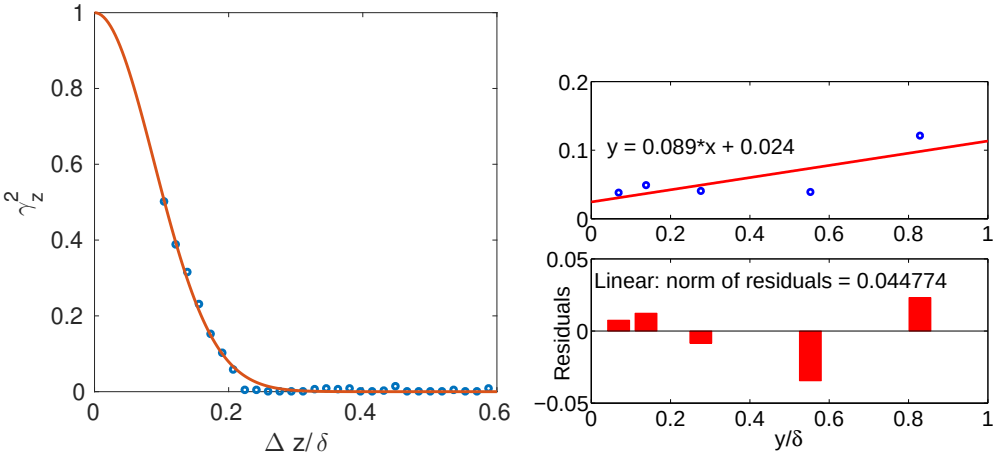

(a) Spanwise coherence (b) Empirical parameter c_{ℓ_z}

Figure 4.8: a) Spanwise coherence for $y/\delta = 0.55$. b) Empirical parameter c_{ℓ_z}, linear fit and residuals as a function of y/δ. Data taken at 1 mm downstream of the TE for Case 3.

where U_c is the local mean velocity and τ is time.

Using the same curve fitting procedure as for the wall-normal and spanwise cases, it was determined that the streamwise coherence data is well represented by an exponential function of streamwise separation Δx, with a decay rate that depends on y/δ, given by

$$\gamma_x^2 = \exp\left(-\frac{\Delta x}{L_x}\right) \tag{4.46}$$

where $L_x = c_{\ell_x} k^{3/2}/\epsilon$ is a length scale and c_{ℓ_x} is an empirical coefficient, which is a function of distance to the wall.

Figure 4.9(a) shows equation 4.46 and experimental data for Case 2 at $y/\delta = 0.39$. The agreement is good.

Figure 4.9(b) shows the empirical coefficient c_{ℓ_x} and a linear curve fit applied for data in the range $0.1 \leq y/\delta \leq 0.7$. In this range, the coefficient grows as a linear function of distance to the wall. For points closer to the wall, c_{ℓ_x} starts to deviate from the linear trend, as well as for points above $y/\delta > 0.7$.

For Case 1, c_{ℓ_x} presents a plateau in the range $0.1 \leq y/\delta \leq 0.7$, with a value of $c_{\ell_x} = 0.12 \pm 0.01$, as shown in Figure 4.10(b). The coefficient c_{ℓ_x} decreases as distance to the wall is decreased below $y/\delta \leq /0.1$, and increases rapidly for $y/\delta \geq 0.7$.

For Case 3, c_{ℓ_x} also presents a plateau in the range $0.1 \leq y/\delta \leq 0.3$, with a value of $c_{\ell_x} = 0.11 \pm 0.004$, as shown in Figure 4.11(b). The coefficient c_{ℓ_x} decreases as distance to the wall is decreased below $y/\delta \leq /0.1$, and increases rapidly for $y/\delta \geq 0.4$. The exponential fit given by equation 4.46 becomes poor outside the range $0.1 \leq y/\delta \leq 0.3$, particularly in the outer part of the boundary layer.

4.5 Autospectrum models

In this section, alternative models for the function f_2 are presented. As stated previously, the function f_2 is related to the autospectra of the turbulent velocity at

Table 4.2: Curve fit parameters for spatial component of coherence function

	c_{ℓ_x}		c_{ℓ_y}		c_{ℓ_z}	
	m	n	m	n	m	n
Case 1	0	0.12	0.14	0.0013	0.2	0.012
Case 2	0.067	0.11	0.083	0.12	0.13	0.056
Case 3	0	0.11	0.087	0.034	0.089	0.024

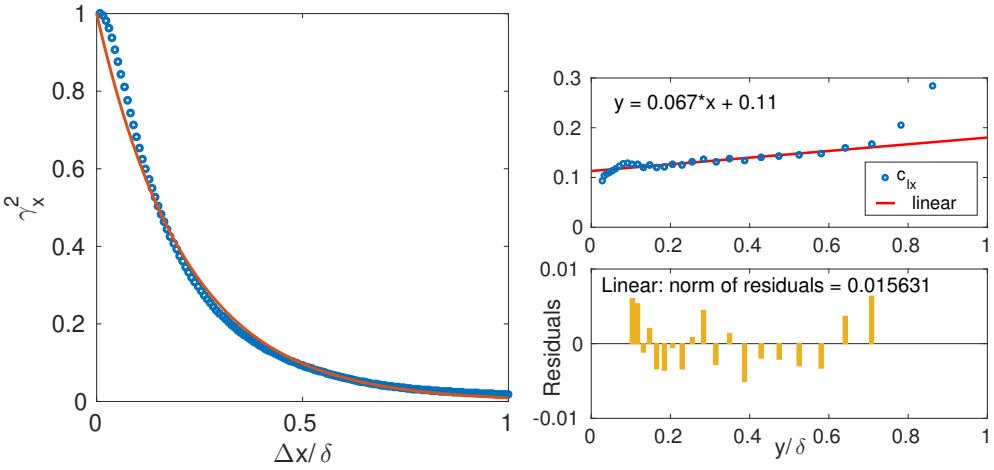

(a) (b)

Figure 4.9: a) Streamwise autocorrelation for Case 2, at $y/\delta = 0.39$. Symbols: experimental data, Solid line: curve fit. b) Empirical parameter c_{ℓ_x}, linear fit and residuals as a function of distance to the wall.

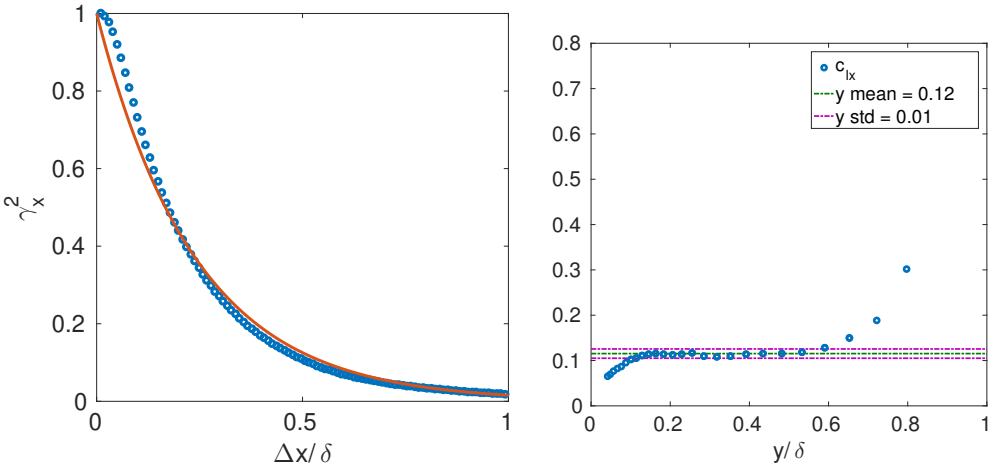

(a) (b)

Figure 4.10: a) Streamwise autocorrelation for Case 1, at $y/\delta = 0.39$. Symbols: experimental data, Solid line: curve fit. b) Empirical parameter c_{ℓ_x} as a function of distance to the wall.

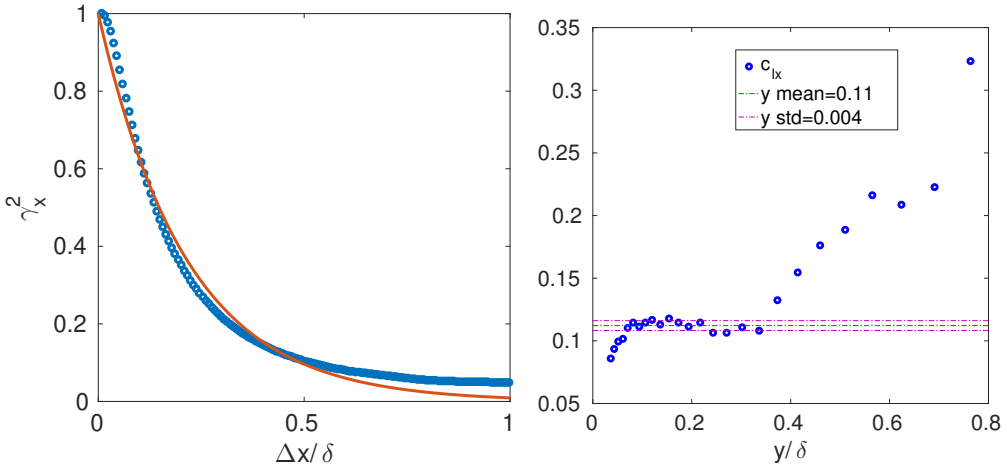

(a) (b)

Figure 4.11: a) Streamwise autocorrelation for Case 3, at $y/\delta = 0.17$. Symbols: experimental data, Solid line: curve fit. b) Empirical parameter c_{ℓ_x} as a function of distance to the wall.

points $\mathbf{y_1}$ and $\mathbf{y_2}$. In the literature, both models and measurements of the autospectrum are often presented in wavenumber space, and they are typically presented in cartesian coordinates. For consistency with the literature, we will adhere to these conventions. Because of the assumption of isotropic turbulence ($f_a = 1$), E_{rr} is related to E_{11} by a factor of $(cos(\theta) - sin(\theta))^2$. We therefore switch our attention to finding a model for $E_{11}(\mathbf{y_1}, \mathbf{y_2}, \kappa_1)$, where $\kappa_1 = \omega/U_c$ is the wavenumber in the streamwise direction and U_c is the local convection velocity.

4.5.1 Gaussian spectrum

The Gaussian model proposed by Morris and Farassat (2002) can be written in terms of wave number as

$$E_{11}(\kappa_1, \mathbf{y_1}) = A_1 \frac{\sqrt{\pi}}{\omega_s} u_s^2 \exp\left(-\frac{\kappa_1^2 U_c^2}{4\omega_s^2}\right), \tag{4.47}$$

where A_1 is an empirical amplitude parameter. The coefficients A_1 and c_τ are determined by enforcing the condition

$$\int_0^\infty E_{11}(\kappa_1, \mathbf{y_1}) d\kappa_1 = \langle {u_1'}^2(\mathbf{y_1}) \rangle. \tag{4.48}$$

or alternatively, the model longitudinal spectrum can be fitted to experimental longitudinal spectrum data using a least squares approach. Since k and ϵ can be obtained

for RANS CFD, the former approach is preferred and used here.

Figures 4.13(a) and 4.13(b) show the turbulent kinetic energy k and dissipation ϵ, respectively. These figures compare the experimental values of k and ϵ for Case 2 and those obtained by integrating the model spectrum. The model is shown to produce the correct values for both quantities. Similar results were obtained for Cases 1 and 3 (see Appendix A).

Figure 4.12 shows the model longitudinal spectrum compared to the experimental data for Case 2 at various distances to the wall. The agreement is good at low wavenumbers, however, for $\kappa \geq 1000$, the model spectrum decays too fast. Similar results were obtained for Cases 1 and 3 (see Appendix A). The effects of this mismatch at high wavenumbers is not expected to have much impact on the noise prediction capabilities of the model, since most of the energy is contained at the lower wavenumbers. Furthermore, it was shown that neglecting the frequency component of the coherence function in the cross spectrum model results in a decay rate that is too slow. This could be compensated by the fast decay observed in the autospectrum model. The effects on the final noise prediction will be investigated in Chapter 6.

4.5.2 Pope's model spectrum

A model energy spectrum function $E(\kappa)$ proposed by Pope (2000) is

$$E(\kappa) = C_1 \epsilon^{2/3} \kappa_1^{-5/3} f_L(\kappa_1 L) f_\eta(\kappa_1 \eta), \tag{4.49}$$

where $C_1 = 1.5$ and $L = k^{3/2}/\epsilon$ is a length scale. The non-dimensional functions f_L and f_η determine the shape of the energy containing range and the dissipation range, respectively. The function f_L is given by

$$f_L(\kappa_1 L) = \left(\frac{\kappa_1 L}{[(\kappa_1 L)^2 + C_L]^{1/2}} \right)^{5/3+p_0}, \tag{4.50}$$

where p_0 is taken to be 2, and C_L is a positive constant. The function f_η is defined as

$$f_\eta(\kappa_1 \eta) = \exp\left(-\beta \left[(\kappa\eta)^4 + C_\eta^4 \right]^{(1/4)} - C_\eta \right). \tag{4.51}$$

To obtain the longitudinal spectrum we can integrate the energy spectrum us-

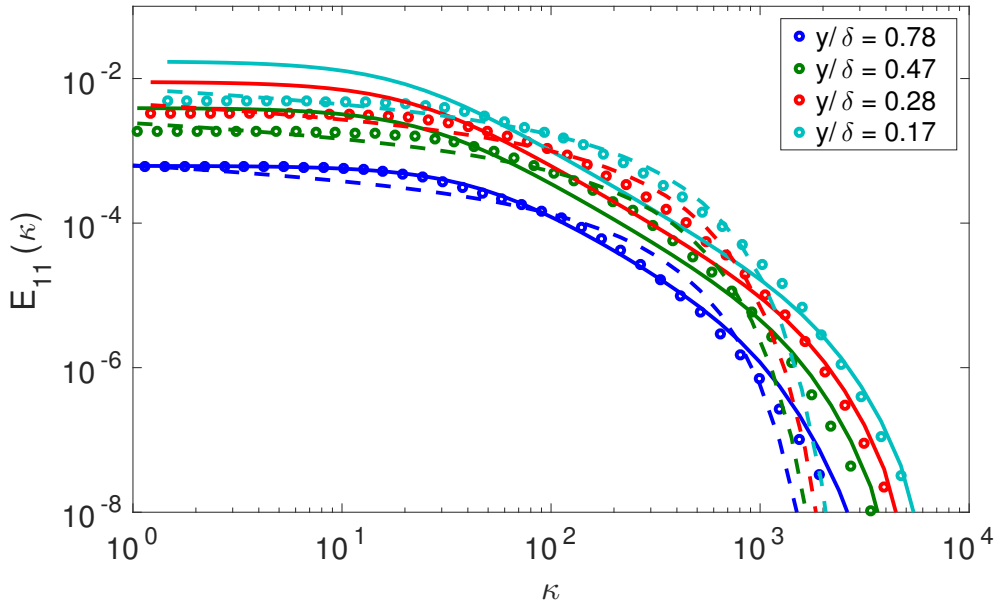

Figure 4.12: Longitudinal autospectrum as a function of wavenumber at selected points in the boundary layer for Case 2. Symbols: experimental data, dashed lines: Morris and Farassat model, solid lines: Pope's model.

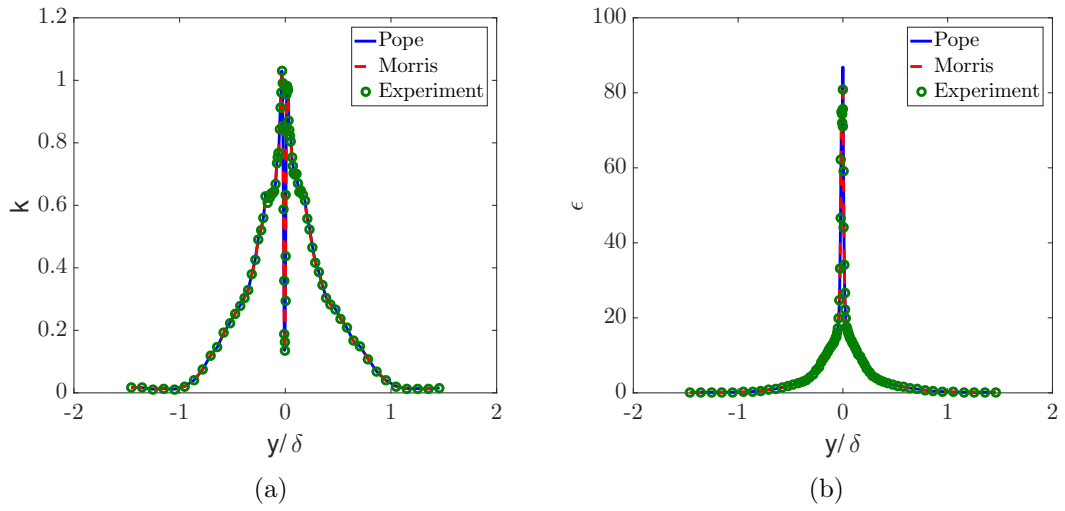

Figure 4.13: Turbulent kinetic energy and dissipation at selected points in the boundary layer for Case 2. Symbols: experimental data, dashed lines: Morris and Farassat model, solid lines: Pope's model.

ing

$$E_{11}(\kappa_1) = \int_{\kappa_1}^{\infty} \frac{E(\kappa)}{\kappa} \left(1 - \frac{\kappa_1^2}{\kappa^2}\right) d\kappa. \tag{4.52}$$

The coefficients C_L and C_η are determined by the requirement that $E(\kappa)$ and $2\nu\kappa^2 E(\kappa)$ integrate to k and ϵ, respectively. Alternatively, they can be determined from the one-dimensional spectrum using equation 4.48.

The longitudinal autospectrum $E_{11}(\kappa_1)$ calculated from Pope's model spectrum is shown in Figure 4.12 at selected locations in the boundary layer for Case 2 and compared to the Gaussian model and experimental data. The model provides a very good fit for $y/\delta = 0.78$, but the agreement deteriorates as the wall is approached. For $y/\delta \leq 0.5$, the model over predicts the spectra at $\kappa \leq 40$, and under predicts the spectra for $40\kappa \leq y/\delta \leq 1000$, but it follows the experimental data well for $1000 \leq y/\delta$. The model predicts the correct values for k and ϵ, as is shown in Figures 4.13(a) and 4.13(b).

4.6 RANS implementation

In order to calculate the power spectral density of the acoustic pressure in the far field, the chosen cross-spectrum model is substituted into Eq. 4.15, and the double integral is replaced by a double summation,

$$S(\mathbf{x}, \omega) = \sum \sum \Psi\Phi \frac{F(\mathbf{y_1})}{r_o^{3/2}(\mathbf{y_1})} \frac{F(\mathbf{y_2})}{r_o^{3/2}(\mathbf{y_2})} dV(\mathbf{y_1}) dV(\mathbf{y_2}). \tag{4.53}$$

This is a simple rectangle rule implementation to evaluate the double volume integral in 4.15, which can handle the weak (integrable) singularity at the trailing edge. Eq 4.53 can be evaluated on the same grid used to compute the RANS solution, or interpolated onto a superimposed acoustic grid, with the required parameters sampled at the cell centres. The power spectral density $S(\mathbf{x}, \omega)$ is proportional to the volume of the source elements $dV(\mathbf{y_1})$ and $dV(\mathbf{y_2})$. If a 3D RANS simulation is performed, the volume of each source element can be determined by means of a grid independence study, that is, refining the grid spacing until $S(\mathbf{x}, \omega)$ converges.

However, it is often more practical to perform a 2D RANS simulation to evaluate a new airfoil shape. In this case,

$$dA = r_0 dr_0 d\theta_0 = dV/dz. \tag{4.54}$$

To obtain dV, a suitable spanwise cell length dz has to be chosen, and a correction for the number of cells along the span must be applied.

4.6.1 Correction for finite span

Consider an airfoil of span L, as shown in Figure 4.14.

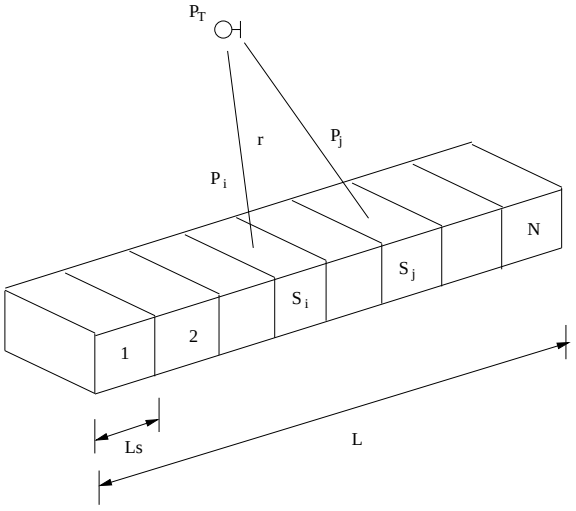

Figure 4.14: Schematic of a long-span body divided by N subsections, adapted from Seo and Moon (2007)

If the span is divided into strips of spanwise length L_s, and each strip is considered an independent source (the spanwise coherence length ℓ_{sz} is less than the spanwise length of the cell, or $\ell_{sz} \leq L_s$), such that

$$|p_1|^2 = |p_2|^2 = ... = |p_N|^2 = |p_s|^2, \tag{4.55}$$

then the total acoustic pressure at a far field point due to the contribution of each strip is given by

$$|p_L|^2 = |p_1|^2 + |p_2|^2 + ... + |p_N|^2 = N|p_s|^2, \tag{4.56}$$

where $N = L/L_s$. This results in a correction of $SPL_c = 10log(N)$ to be added to the noise due to the simulated strip SPL_s (Kato *et al.* 1993). If the coherence length is greater than the span of the airfoil ($\ell_{sz} > L$), then the correction factor is $SPL_c = 20log(N)$. Although this two asymptotic values are correct, Seo and Moon (2007) found this correction to be rather ad-hoc when $L_s \leq \ell_{sz} \leq L$. Seo and Moon

(2007) provide a more accurate correction factor for three possible cases:

$$SPL_c = \begin{cases} 10log(N) & \text{if } \ell_{sz}/L_s \leq 1/\sqrt{\pi}, \\ 10log(\ell_{sz}/L_s) + 10log(\sqrt{\pi}N) & \text{if } 1/\sqrt{\pi} < \ell_{sz}/L_s < N/\sqrt{\pi}, \\ 20log(N) & \text{if } \ell_{sz}/L_s > N/\sqrt{\pi}. \end{cases} \tag{4.57}$$

To apply this, $|p_s|^2$ must be accurately calculated, and an estimation of ℓ_{sz} is required.

4.6.1.1 Calculating the noise from a single strip

Equation 4.15 shows that the noise at the observer position is proportional to the volume of the acoustic source elements, which can be (but need not be) assumed to be uniform,

$$S(\mathbf{x}, \omega) \propto dV_1 dV_2 = dV^2. \tag{4.58}$$

Using a Cartesian coordinate system with x,y,z being the streamwise, cross-flow and spanwise directions, respectively, the cell volume becomes,

$$dV = dxdydz. \tag{4.59}$$

dx and dy can be determined by a grid independence study while assuming $dz = 1$ to obtain a PSD per unit length, S_1. This value has to be corrected to account for the actual size of each cell in the spanwise direction. In the derivation of RSNM, the assumption was made that points within a cell are perfectly correlated to each other. This assumption holds only if the cells are small enough, that is,

$$\begin{aligned} dx &<< \ell_{sx} \\ dy &<< \ell_{sy} \\ dz &<< \ell_{sz}, \end{aligned} \tag{4.60}$$

where ℓ_{sx}, ℓ_{sy}, and ℓ_{sz} are the coherence lengths in the x, y and z directions, respectively. An assumption regarding the value of $dz = L_s$ has to be made in order to calculate the noise radiated by a single strip S_s. In order to use equation 4.57, the following assumption is made:

$$\frac{1}{2} = \frac{\ell_{sz}}{L_s}. \tag{4.61}$$

There are two drawbacks that arise from this assumption. Firstly, ℓ_{sz} is assumed to be constant, when in reality it is a function of frequency. For modelling purposes it is desirable to have the spectral shape controlled by the shape of the autospectrum, and not by the spatial coherence function. The effect on the noise predictions capabilities of RSNM of neglecting the frequency dependence of ℓ_{sz} will be evaluated in Chapters 7, 8 and 9. Secondly, Equation 4.61 conflicts with $dz << \ell_{sz}$. This requires a further correction, for the fact that the points inside the cell will not be perfectly correlated. A solution is to find the average coherence for points inside the cell.

Consider two points within a cell, z_1 and z_2, with z_1 located at the centre of the cell, and z_2 located randomly within the cell. The cell has a spanwise extent of $[0\ L_s]$. The probability density function of the location of z_2 within the cell is given by

$$f_{z_2} = \begin{cases} \frac{1}{L_s} & \text{if } z_2 \in [0\ L_s] \\ 0 & \text{if } z_2 \notin [0\ L_s]. \end{cases} \tag{4.62}$$

Assuming a Gaussian form for for the spanwise coherence

$$\gamma_{z_1 z_2} = \exp\left(-\frac{\Delta z^2}{\ell_{sz}^2}\right) = \exp\left(-\frac{(\frac{L_s}{2} - z_2)^2}{\ell_{sz}^2}\right). \tag{4.63}$$

The average correlation within the cell is then

$$\begin{aligned} \langle \gamma_{z_1 z_2} \rangle &= \int_{-\infty}^{\infty} \gamma_{z_1 z_2} f_{z_2}\, dz_2 \\ &= \int_{-\infty}^{\infty} \exp\left(-\frac{(\frac{L_s}{2} - z_2)^2}{\ell_{sz}^2}\right) \frac{1}{L_s}\, dz_2 \\ &= \int_{0}^{L_s} \exp\left(-\frac{(\frac{L_s}{2} - z_2)^2}{\ell_{sz}^2}\right) \frac{1}{L_s}\, dz_2 \\ &= \frac{\ell_{sz}\sqrt{\pi}}{L_s} \mathrm{erf}\left(\frac{L_s/2}{\ell_{sz}}\right). \end{aligned} \tag{4.64}$$

With our assumption of $L_s = 2\ell_{sz}$, then

$$\langle \gamma_{z_1 z_2} \rangle = \frac{\sqrt{\pi}}{2} \mathrm{erf}\,(1) = 0.7468. \tag{4.65}$$

Now the noise due to a single strip of span $L_s = 2\ell_{sz}$ can be calculated as

$$\begin{aligned} S_s(\mathbf{x}, \omega) &= 0.7468 \times 2\ell_{sz} \times S_1 \\ &= 0.7468 \times L_s \times S_1 \end{aligned} \tag{4.66}$$

where S_1 is the power spectral density per unit span. This result allows us to use the correction of Seo and Moon (2007) given in equation 4.57, so the total noise due to the full span airfoil will be

$$\begin{aligned} S_L(\mathbf{x}, \omega) &= N \times S_s \\ &= \frac{L}{L_s} \times 0.7468 \times L_s \times S_1 \\ &= L \times 0.7468 \times S_1. \end{aligned} \tag{4.67}$$

The total noise is proportional to the span of the airfoil.

4.7 Summary

In this chapter, the derivation of a noise prediction method based on the theory of Ffowcs Williams and Hall (1970) was presented. The method requires a model for the cross-spectrum of the turbulent velocity fluctuations. A model for the cross-spectrum was derived from a cross-correlation function based on the work of Morris and Farassat (2002). The model can be separated into two functions, which are related to the coherence function at zero frequency and the autospectrum, respectively. Two alternative models for the coherence were provided, namely the SAS model of Gavin (2002) and a semi-empirical model based on the experimental data collected during this research. The semi-empirical coherence model neglects the frequency dependency of the coherence by onsidering only the amplitude of the coherence function at zero frequency. It assumes that the coherence function can be separated into orthogonal components. It was found that this function has an exponential form in the streamwise and wall-normal directions, and a Gaussian form in the spanwise direction. The decay rates are a function of distance to the wall, and

are also affected by the pressure gradient. Empirical coefficients were found for the decay rates in each direction, for each of the three cases studied.

Alternative models for the autospectrum were also provided, namely the Model Spectrum of Pope, and a simplified Gaussian model. It was found that the Gaussian model provides a good fit to the data at low and medium frequencies , but decays too quickly at higher frequencies. Pope's model provides excellent fit at high frequencies, but overpredicts the spectrum at low frequency. Both models provide the correct values of turbulent kinetic energy and dissipation.

The success of the models developed in this chapter will be determined by their ability to provide accurate noise predictions when implemented in the RSNM framework. This is the subject of the following chapters.

Finally, a methodology to correct the 2D simulations to account for the real finite span was presented.

Chapter 5

Numerical investigation

This chapter describes the computational approach used to generate the flow information required to perform noise calculations. It includes a description of the Reynolds Average Navier Stokes (RANS) equations and the SST $k-\omega$ turbulence model, followed by a description of the numerical settings and grids used.

A grid refinement study is presented for three airfoil geometries (a NACA-0012, a DU-96-180 and the custom FP-12), and the solutions present sufficient levels of grid independence. The CFD results are also compared against experimental data of Brooks *et al.* (1989), Devenport *et al.* (2010) and Moreau *et al.* (2011) as a preliminary validation.

5.1 RANS

For incompressible flow in Cartesian coordinates, the continuity and Navier Stokes equations are

$$\nabla \cdot \mathbf{u} = 0 \tag{5.1}$$

$$\frac{\partial u_i}{\partial t} + \nabla \cdot (u_i \mathbf{u}) = -\frac{1}{\rho}\frac{\partial p}{\partial x_i} + \nu \nabla \cdot (\nabla u_i) \tag{5.2}$$

Using Reynolds decomposition, the velocity and pressure become $\mathbf{u} = \mathbf{U} + \mathbf{u}'$ and $p = P + p'$, where the upper case letters represent the mean value and the prime represents the fluctuation about the mean.

Replacing the decomposed variables in the equations and taking the time average we obtain

$$\nabla \cdot \mathbf{U} = 0 \tag{5.3}$$

$$\frac{\partial U_i}{\partial t} + \nabla \cdot (U_i \mathbf{U}) + \nabla \cdot (\overline{u_i' \mathbf{u}'}) = -\frac{1}{\rho}\frac{\partial P}{\partial x_i} + \nu \nabla \cdot (\nabla U_i) \tag{5.4}$$

Note that an extra term $\nabla \cdot (\overline{u_i' \mathbf{u}'})$ has arisen in the momentum equation due to the time averaging process. It is customary to move this term to the right hand side of the equation, in order to clarify its role as representing additional turbulent stresses associated with the mean velocities. Expanding this term for clarity yields:

$$\frac{\partial U_i}{\partial t} + \nabla \cdot (U_i \mathbf{U}) = -\frac{1}{\rho}\frac{\partial P}{\partial x_i} + \nu \nabla \cdot (\nabla U_i) + \frac{1}{\rho}\left[\frac{\partial (-\rho \overline{u_i' \mathbf{u}'})}{\partial x_i}\right] \tag{5.5}$$

As a result of the Reynolds decomposition, six additional terms of the form $\rho(\overline{u_i' \mathbf{u}'})$ have appeared, which are known as the Reynolds stresses, and they are of fundamental importance for aerodynamic noise calculations. As there are more unknowns than equations, a turbulence model is required for closure. There are a number of turbulence models described in the literature, ranging from the simple mixing length model of Prandtl, to the more complex Reynolds stress model (RSM) (Launder *et al.* 1975). For a thorough review on the available turbulence models, the reader is referred to Versteeg and Malalasekera (2007). The choice of turbulence model depends on the application and the computational resources available. For this research, the SST $k-\omega$ model (Menter 1992a) has been chosen, as it has been shown to perform well for boundary layers in both zero pressure gradients and in adverse pressure gradients (Menter 1992b). Further,the SST $k-\omega$ model has been successfully used to provide RANS flow data for trailing edge noise calculations using the fluctuating surface pressure approach (Kamruzzaman *et al.* 2008).

5.2 The SST $k-\omega$ turbulence model

The SST $k-\omega$ turbulence model combines the $k-\epsilon$ and $k-\omega$ turbulence models by means of a blending function, retaining the good near-wall performance of the $k-\omega$ model, and the robustness of the $k-\epsilon$ model away from the wall. The model's equations are presented here as shown in Menter *et al.* (2003)

$$\frac{\partial(\rho k)}{\partial t} + \nabla \cdot (\rho k \mathbf{U}) = \nabla \cdot \left[\left(\mu + \frac{\mu_t}{\sigma_k} \right) \nabla k \right] + P_k - \beta^* \rho k \omega \tag{5.6}$$

$$\begin{aligned} \frac{\partial(\rho\omega)}{\partial t} + \nabla \cdot (\rho\omega \mathbf{U}) = \nabla \cdot \left[(\mu + \sigma_{\omega 1}\mu_t) \nabla\omega \right] + \alpha_2 \rho S^2 - \beta_2 \rho \omega^2 \\ + 2(1 - F_1)\rho\sigma_{\omega 2} \frac{1}{\omega} \frac{\partial k}{\partial x_i} \frac{\partial \omega}{\partial x_i} \end{aligned} \tag{5.7}$$

where the blending function F_1 is:

$$F_1 = \tanh \left\{ \left\{ min \left[max \left(\frac{\sqrt{(}k)}{\beta^* \omega y}, \frac{500\nu}{y^2 \omega} \right), \frac{4\rho\sigma_{\omega 2} k}{CD_{k\omega} y^2} \right] \right\}^4 \right\} \tag{5.8}$$

with

$$CD_{k\omega} = max \left(2\rho\sigma_{\omega 2} \frac{1}{\omega} \frac{\partial k}{\partial x_i} \frac{\partial \omega}{\partial x_i}, 10^{-10} \right) \tag{5.9}$$

and y is the distance to the wall. $F_1 = 0$ away from the surface ($k - \epsilon$ model) and changes to $F_1 = 1$ inside the boundary layer ($k - \omega$ model). The eddy viscosity is defined as:

$$\nu_t = \frac{a_1 k}{max(a_1 \omega, SF_2)} \tag{5.10}$$

Where S is the invariant of the strain rate and F_2 is another blending function given by:

$$F_2 = \tanh \left[\left[max \left(\frac{2\sqrt{k}}{\beta^* \omega y}, \frac{500\nu}{y^2 \omega} \right) \right]^2 \right] \tag{5.11}$$

to prevent the build-up of turbulence in stagnation regions, a production limiter is used, given by:

$$P_k = \mu_t \frac{\partial U_i}{\partial x_j} \left(\frac{\partial U_i}{\partial x_j} + \frac{\partial U_j}{\partial x_i} \right) \;\rightarrow\; \tilde{P}_k = min(P_k, 10\beta^* \rho k \omega) \tag{5.12}$$

The model constants are computed by a blend of the $k-\omega$ and $k-\epsilon$ constants using the blending functions, for example $\alpha = \alpha_1 F + \alpha_2(1 - F)$. The model constants are shown in table 5.1

5.3 Numerical schemes

All the RANS-CFD calculations were performed using the Semi-Implicit Method for Pressure Linked Equations (SIMPLE) algorithm and the SST $k - \omega$ turbulence model within the OpenFOAM CFD package. The discretization scheme for the

Table 5.1: SST $k-\omega$ model constants

α_1	α_2	σ_{k1}	σ_{k2}	$\sigma_{\omega1}$	$\sigma_{\omega2}$	β_1	β_2	β^*
5/9	0.44	0.85	1	0.5	0.856	3/40	0,083	0.09

gradient, divergence and Laplacian terms was set to *Gauss*, which uses Gaussian finite volume integration. Gaussian integration is based on summing values on cell faces, which must be interpolated from cell centres. This was done using second order central difference interpolation for all variables except k and ω, for which first order upwind difference interpolation was used, as second order schemes caused numerical instabilities. After the solution had reached a significant level of convergence (10^{-3} for pressure and 10^{-5} for all other variables), interpolation schemes for k and ω were changed to second order central difference interpolation, and the simulation was run until residuals reached values below 10^{-6} for pressure and 10^{-7} for k, ω, U_x, and U_y. Therefore all numerical schemes were second order.

To aid the convergence process and avoid numerical instabilities, relaxation factors were set to 0.7 for all variables except pressure, for which the relaxation factor was set to 0.3, and an inviscid flow simulation was preformed using the *potentialFoam* utility to provide a starting condition for the flow field.

5.4 Boundary conditions

To define the boundary conditions for the turbulent kinetic energy k and dissipation ω, the following was used,

$$k = \frac{3}{2}\left(\frac{U_\infty Ti}{100}\right) \tag{5.13}$$

$$\omega = C_\mu \frac{k}{\nu}\left(\frac{\mu_t}{\mu}\right)^{-1} \tag{5.14}$$

where Ti is the turbulence intensity, U_∞ is the free stream velocity, ν is the kinematic viscosity, μ_t is the eddy viscosity, μ is the dynamic molecular viscosity and $C_\mu = 0.09$. An eddy viscosity ratio of $(\mu/\mu_t) = 1$ is assumed. A sensitivity analysis to the value of the eddy viscosity ratio was performed, testing values between $0.1 \leq (\mu/\mu_t) \leq 1000$. No changes were observed in the resulting boundary layer properties, suggesting the domain boundaries were sufficiently distant from the airfoil to converge to boundary-independent levels before reaching the airfoil. The inlet turbulence intensity was set at $Ti = 0.05\%$, to match the experimental conditions of Brooks *et al.* (1989), and was used for all simulations, as k also seems to reach

boundary-independent levels long before it reaches the airfoil. On the airfoil surface, a continuous wall function was applied to the eddy viscosity μ_t, the turbulent kinetic energy k and dissipation ω. A summary of the boundary conditions is shown in Table 5.2.

5.5 Selected airfoils

Three airfoils were selected for this research, namely a NACA 0012, a DU-96-180 and the custom FP-12, which is a flat strut with a beveled trailing edge. These airfoils were chosen because of the availability of flow and noise data that can be used for validation. The NACA 0012 airfoil is the most commonly used airfoil in the literature, and there is a large body of experimental and numerical data available for comparison and validation at a wide range of Reynolds numbers.

The DU 96-180 is less common, but there is flow and noise data available fromDevenport *et al.* (2010) and from the BANCII workshop (Herr and Kamruzzaman 2013), and it is also not a proprietary airfoil, so the exact geometry is readily available.

The FP-12 was chosen because of the availability of flow and noise data at the school of Mechanical Engineering of the University of Adelaide, and because further data could be obtained for this airfoil with the facilities and equipment available at the University. The long and thin FP-12 allowed for a relatively high Reynolds number ($Re_c = 500,000$) to be achieved at the wind tunnel maximum flow speed, whereas most other airfoils would have caused significant blockage effects long before reaching this Reynolds number. A more detailed description of the FP-12 is given in Chapter 2

Table 5.2: Computational fluid dynamic boundary conditions.

Field	Inlet	Outlet	Airfoil
U	Fixed Value	Zero Gradient	Fixed Value
p	Zero Gradient	Fixed Value	Zero Gradient
k	Fixed Value	Zero Gradient	omegaWallFunction
ω	Fixed Value	Zero Gradient	omegaWallFunction

5.6 The computational grids

The computational grids were structured, multi-block C-type meshes. The CFD domain boundaries were located ten chord-lengths upstream of the leading edge, ten chord-lengths above and below the upper and lower surfaces and twenty chord-lengths downstream of the trailing edge, as shown in Fig. 5.1. These mesh dimensions were chosen so that the boundaries were sufficiently far away from the airfoil to minimize the solution dependency on the chosen boundary conditions at the inlet, and to allow the zero gradient boundary condition to be valid at the outlet.

In all meshes, cell grading was used to provide an adequate number of cells within the boundary layer with a cell aspect ratio of one at the trailing edge. This resulted in 798 cells on the surface of the DU-96 airfoil, 454 cells on the surface of the FP12 airfoil, 679 cells on the surface of the NACA-0012 airfoil used in the cases from Brooks *et al.* (1989), and 958 cells on the surface of the NACA-0012 used in the cases from Devenport *et al.* (2010). The grid properties for the highest Reynolds number cases for studied for each airfoil are shown in Table 5.3. It can be seen that the maximum $y+$ values are well above the recommended values of $y+ < 5$ for integration to the wall, so the use of wall functions is justified. Enlarged views of the meshes used are show in Figures 5.2(a), 5.2(b) and 5.2(c). The justification for choosing these meshes is given in Section 5.7.

5.7 Verification of CFD results

In this section, the quality of the CFD results is evaluated. This is done by performing a grid refinement study and then by comparing the results to experimental data from selected cases in the literature. A grid refinement study is a procedure to quantify the discretization error for target quantities of interest in the flow, where the aim is to achieve a reduction of discretization error in two or three successive levels of grid refinement. The grid refinement study made use of the grid conver-

Table 5.3: Grid properties

Airfoil	Surface cells	Total cells	min $y+$	max $y+$	av. $y+$
NACA-0012 (Brooks)	798	112,998	11.3	29.6	18.3
NACA-0012 (Devenport)	958	215,400	23.1	56.7	35.1
DU-96	798	346,580	3.9	38.6	14.6
FP12	454	187,850	0.0024	0.0702	0.0088

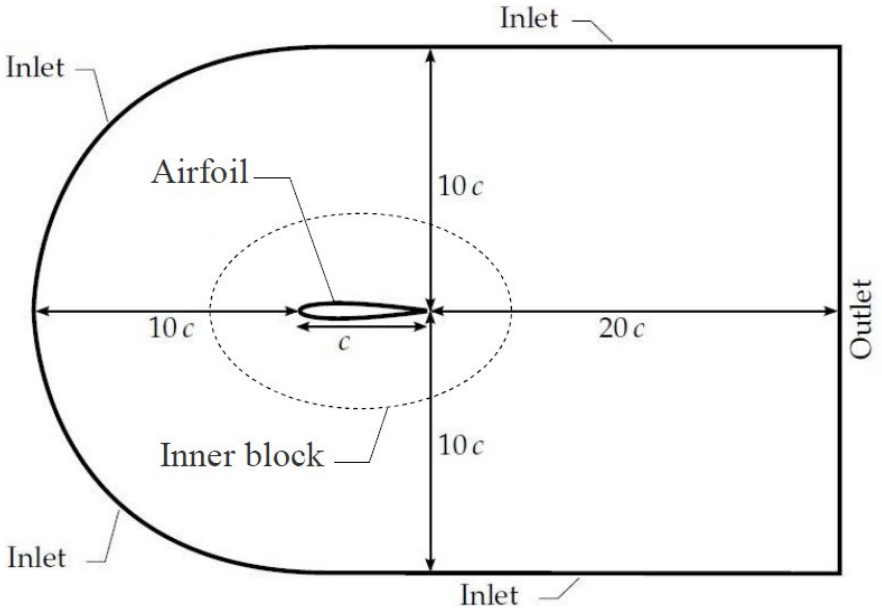

Figure 5.1: Schematic of the CFD simulation domain, adapted from Jones (2013)

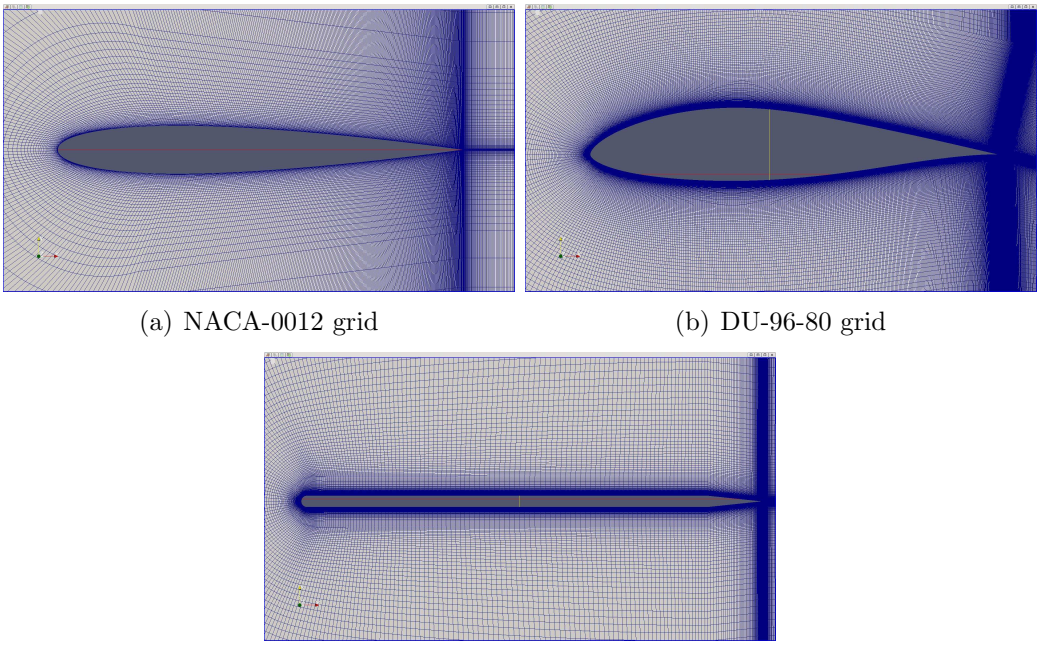

(a) NACA-0012 grid

(b) DU-96-80 grid

(c) FP-12 grid

Figure 5.2: The computational grids used for all CFD calculations.

gence index or GCI of Roache (1998). The GCI method requires the calculation of an error term for the target quantity f

$$\epsilon_{i+1,i} = \frac{|f_{i+1} - f_i|}{f_i} \tag{5.15}$$

where $i = 1, 2, 3$, and $i = 1$ corresponds to the mesh with the highest resolution. The grid convergence index is defined as

$$GCI(\%) = 100 \times Fs \frac{\epsilon_{i+1,i}}{r^p - 1} \tag{5.16}$$

where $Fs = 1.25$ is a safety factor, $r = h_i/h_{i-1}$ is the ratio of cell size for mesh i and mesh $i - 1$ and p is the order of convergence that can be calculated as

$$p = \ln\left(\frac{|f_{i+2} - f_{i+1}|}{|f_{i+1} - f_i|}\right) / \ln(r) \tag{5.17}$$

An estimate of the exact value f_e (the asymptotic value for a grid of infinite resolution) can be calculated as

$$f_e = f_i + \frac{(f_i - f_{i+1})}{r^p - 1} \tag{5.18}$$

The possible convergence conditions are

1. Monotonic Convergence, $0 < R < 1$.
2. Oscillatory convergence, $R < 0$.
3. Divergence, $R > 1$.

Where R is the convergence ratio, defined as,

$$R = \frac{f_{i+1} - f_i}{f_{i+2} - f_{i+1}} \tag{5.19}$$

Three different refinement levels were used for this study, as recommended by Wilcox (2006), where each refinement step consisted in a doubling of the number of cells (or halving of the cell area) of the previous step, which results in a refinement ratio of $r = \sqrt{2}$. For the DU 96-180 case and the FP-12 case, this doubling of cells was conducted in an inner block containing all cells within a distance of approximately $d = c/4$ from the airfoil surface, and the mesh grading was adjusted in the outer block to ensure a smooth transition between the blocks.

The target quantities for the grid refinement study where the boundary layer dis-

placement thickness δ^*, the boundary layer momentum thickness θ, and the drag coefficient C_d. In order to calculate δ^* and θ, the boundary layer thickness is required. The standard definition of the boundary layer thickness is distance from the solid surface at which the velocity reaches 99% of the free stream velocity, but this definition results in artificially large values for the boundary layer thickness over most airfoils, due to flow curvature effects (Devenport *et al.* 2010). Therefore, in this work an alternative method is used to calculate the boundary layer thickness based on the turbulence kinetic energy profiles. The edge of the boundary layer was defined as the point where turbulence kinetic energy has a value of 0.5% of its peak value, or $k = 0.005k_{max}$. Then the displacement thickness and momentum thickness can be evaluated using the standard definitions,

$$\delta^* = \int_0^\delta \left(1 - \frac{U}{U_e}\right) d|y - y_0| \tag{5.20}$$

$$\theta = \int_0^\delta \frac{U}{U_\infty}\left(1 - \frac{U}{U_e}\right) d|y - y_0| \tag{5.21}$$

Where U is the mean flow velocity, U_e is the flow velocity at the edge of the boundary layer and y_0 is point of minimum free stream velocity if the measurements are taken just downstream of the trailing edge, or the position of the airfoil surface if the measurements are taken upstream from the trailing edge.

5.7.1 NACA-0012 airfoil

For the NACA-0012 airfoil, the grid refinement study was conducted for a chord of $c = 30.48$ cm, at an angle of attack of $AoA = 0$ degrees and a Reynolds number based on chord of $Re_c = 1,5 \times 10^6$. This was the highest Reynolds number of the Brooks *et al.* (1989) cases studied, and would therefore require the highest mesh resolution for this set of experimental data. The displacement thickness δ^* and momentum thickness θ were calculated at 1.3 mm downstream of the trailing edge to match the measurements of Brooks *et al.* (1989). Table 5.7 shows the results of the grid convergence study. Notice that an order of convergence of $p > 2$ would exceed the order of the numerical schemes. If this occurred, a value of $p = 2$ was employed in the GCI calculations. A GCI below 5% was obtained for all target quantities with mesh 2, which is considered sufficiently accurate, therefore, this mesh was used to perform all CFD calculations of the Brooks *et al.* (1989) cases.

As a preliminary validation, the results are compared to experimental values. A detailed validation of the CFD results is presented in Chapter 6.

5.7.2 Du-96-180 airfoil

For the DU 96-180 case, the grid refinement study was conducted for a 91.4 cm chord airfoil, at an angle of attack of $AoA = 7$ degrees and a Reynolds number based on chord of $Re_c = 3,130,000$. The displacement thickness δ^* and momentum thickness θ were calculated at a location 1.9 mm downstream of the trailing edge to match the measurement location reported in Devenport *et al.* (2010). The results of this study are shown in Tables 5.9 and 5.10. Mesh 3 was selected for all CFD calculations of the DU 96-180 airfoil, due to the very low GCI values obtained with this mesh for all target quantities (all below 5%), and because the values for all target quantities were very close to the asymptotic value, which indicates that any further increase in grid resolution will produce negligible improvements in the accuracy of the results.

5.7.3 FP-12 airfoil

For the FP-12 airfoil, experimental data for fully turbulent boundary layer are available only for a single case (Moreau *et al.* 2011). The airfoil has a chord of $c = 20.00$ cm, the angle of attack was set at $AoA = 0$ and the free stream velocity was $U_\infty = 38\,\mathrm{m/s}$. Tables 5.11, 5.12 and 5.13 show the grid properties, boundary layer properties and GCI results, respectively, for the FP-12 airfoil. All meshes show very low values of $y+$. Meshes 2 and 3 show low GCI values for all target quantities, and are therefore well resolved. Mesh 3 was used, due to its better grid statistics. It should be noted that the predicted values for all boundary layer properties are much smaller than those measured by Moreau *et al.* (2011). This could be caused by the effect of the shear layers in the experimental data, as the measurements were performed in an open jet wind tunnel.

Table 5.4: Grid properties or a NACA-0012 airfoil at $Re = 1.5 \times 10^6$

	No. of cells	TE $y+$	max $y+$	average $y+$
Mesh 1	215,400	9.4	22.5	13.8
Mesh 2	112,998	11.3	29.6	18.3
Mesh 3	53,850	13.9	42.4	26.1

Table 5.5: Grid properties for a NACA-0012 airfoil at $Re = 4 \times 10^6$

	No. of cells	TE $y+$	max $y+$	average $y+$
Mesh 1	215,400	23.1	56.7033	35.1289
Mesh 2	112,998	24.0	74.8261	46.8289
Mesh 3	53,850	37.5	112.224	69.5361

Table 5.6: Numerical and experimental displacement thickness δ^* and momentum thickness θ_s, measured at the 1.3 mm downstream of the trailing edge, and drag coefficient C_d, for the NACA-0012 airfoil with a chord based Reynolds number of $Re_c = 1.5 \times 10^6$ and angle of attack of $AoA = 0$. The symbols f_e and f_m stand for exact value (asymptotic value) and measured value.

	δ^* (mm)	θ (mm)	$Cd \times 10^{-3}$
Mesh 3	2.1237	1.2697	11.6677
Mesh 2	2.0586	1.2211	11.2917
Mesh 1	2.0486	1.2131	11.2383
f_e	2.1063	1.2050	11.1849
f_m	2.96	1.62	–

Table 5.7: Order of accuracy and Grid Convergence Index (GCI) for the 30.48 cm chord NACA-0012 airfoil at $Re = 1.5 \times 10^6$.

Variable	$\lvert\epsilon_{3,2}\rvert$	$\lvert\epsilon_{2,1}\rvert$	R	p	$GCI_{3,2}$	$GCI_{2,1}$
δ^*	0.0316	0.0049	0.1532	2, (5.4139)	3.9559%	0.6088 %
θ	0.0398	0.0066	0.1658	2, (5.1853)	4.9738%	0.8300%
C_d	0.0333	0.0048	0.1420	2, (5.6316)	4.1623%	0.5940%

Table 5.8: Grid properties DU-96-180

Mesh	No. of cells	TE $y+$	max $y+$	average $y+$
Mesh 1	346,580	3.9	38.6	14.6
Mesh 2	224,078	5.1	52.9	20.6
Mesh 3	123,716	7.0	73.1	29.1

Table 5.9: Numerical and experimental displacement thickness δ^*, momentum thickness θ_s, recorded at 1.9 mm downstream of the trailing edge, and drag coefficient C_d, for the DU 96-180 airfoil, with a chord based Reynolds number of $Re_c = 3,13 \times 10^6$ and angle of attack of $AoA = 7$. The symbols f_e and f_m stand for exact value (asymptotic value) and measured value (Devenport *et al.* 2010). Subscripts s and p denote suction side and pressure side, respectively.

	δ^*_s(mm)	θ_s(mm)	δ^*_p(mm)	θ_p(mm)	$Cd \times 10^{-3}$
Mesh 3	17.3544	7.1158	1.0894	1.4625	16.2385
Mesh 2	17.0857	6.9449	1.5069	1.5523	15.6365
Mesh 1	17.0243	6.9141	1.4679	1.5853	15.5701
f_e	16.9629	6.8833	1.4290	1.6183	15.5037
f_m	19.7	6.1	3.3	1.6	–

Table 5.10: Order of accuracy and Grid Convergence Index (GCI) for the Du96 airfoil. Subscripts s and p denote suction side and pressure side, respectively

Variable	$\lvert\epsilon_{3,2}\rvert$	$\lvert\epsilon_{2,1}\rvert$	R	p	$GCI_{2,1}$	$GCI_{3,2}$
δ_s^*	0.0157	0.0036	0.2286	2 (4.2588)	1.9654%	0.4508%
θ_s	0.0246	0.0045	0.1802	2 (4.9447)	3.0759%	0.5567%
δ_p^*	0.2770	0.0265	-0.0933	2 (6.8443)	34.6300%	3.3164%
θ_p	0.0579	0.0208	0.3672	2 (2.8908)	7.2340%	2.6010%
C_d	0.0385	0.0043	0.1103	2, (6.3610)	4.8125%	0.5331%

Table 5.11: Grid properties for the FP-12 airfoil

	No. of cells	min $y+$	max $y+$	average $y+$
Mesh 3	64,600	0.0397	1.1714	0.1468
Mesh 2	106,675	0.0095	0.2851	0.0356
Mesh 1	187,850	0.0024	0.0702	0.0088

Table 5.12: Boundary layer parameters for the FP-12 airfoil at 0.7 mm downstream of the trailing edge. The symbols f_e and f_m stand for exact value (asymptotic value) and measured value (Moreau *et al.* 2011).

Mesh	$\delta^*/c \times 10^{-3}$	$\theta/c \times 10^{-3}$	$Cd \times 10^{-3}$
Mesh 3	5.5373	3.3806	27.785
Mesh 2	5.6775	3.4685	28.734
Mesh 1	5.7115	3.4847	29.693
f_e	5.7455	3.5008	30.652
f_m	6.5	5.0	–

Table 5.13: Order of accuracy and Grid Convergence Index (GCI) for the FP-12 airfoil.

Variable	$\lvert\epsilon_{3,2}\rvert$	$\lvert\epsilon_{2,1}\rvert$	R	p	$GCI_{3,2}$	$GCI_{2,1}$
δ^*	0.0247	0.0059	0.2423	2, (4.0897)	3.0863%	0.7435%
θ	0.0254	0.0046	0.1839	2, (4.8857)	3.1688%	0.5801%
C_d	0.0330	0.0323	1.0105	2, (0.0151)	1.3761%	1.3457

5.8 Summary

In this chapter the fundamentals of RANS and the SST $k - \omega$ model have been explained, as well as the numerical settings, grids and boundary conditions used for all the CFD calculations in this thesis. A grid refinement study has been conducted, showing that the grids used are sufficiently resolved to provide a grid independent solution, and the CFD results for three different airfoils at a range of operating conditions have been compared against experimental data of Brooks *et al.* (1989), Devenport *et al.* (2010) and Moreau *et al.* (2011). The CFD results results for boundary layer integral properties are generally smaller than the corresponding experimental values; however, the agreement is considered sufficiently good as a preliminary validation of the CFD data. A more detailed validation is provided in the results chapters for each airfoil.

Chapter 6

Results

6.1 Introduction

In this chapter, the RSNM method is applied to three different airfoil shapes,namely a NACA 0012, a DU-96-180 and a FP-12 airfoil, for a range of operating conditions, and the noise predictions resulting from the different cross-spectrum models are compared with each other as well as with experimental data from the literature. The required mean flow data is taken from RANS CFD, and results for mean velocity, turbulent kinetic energy and turbulence dissipation are presented for selected cases and related to the far field noise spectrum obtained from the simulations.

6.2 Sampling domain

All RSNM calculations were performed on an acoustic grid superimposed on the RANS grid. The values at each cell on the acoustic grid are calculated from the RANS grid by means of linear interpolation. A grid refinement study was conducted in order to determine the resolution required to obtain grid independent acoustic predictions. This was done using a 15.24 cm chord, NACA 0012 airfoil at 31.7 m/s case ($Re_c = 3.33 \times 10^5$). The RANS data were sampled over a domain extending one boundary layer thickness (δ) in both the upstream and downstream directions from the trailing edge, and with a height of one boundary layer thickness. An initial grid resolution of 50×50 cells per δ^2 was used for the noise calculation, which was then increased to 100×100 and 200×200 per δ^2. As Figure 6.2 shows, no discernible change occurs when the resolution was increased beyond 100×100 cells per δ^2;

therefore this resolution was chosen for all noise calculations in this study.

In order to determine extent of the sampling domain required for converged results, simulations were carried out extending the domain upstream and downstream of the trailing edge. Three domain sizes were tested, namely a small, a medium and a large domain. The sampling domain was defined by all the points (x,y) such that $TE - \Delta_i \leq x \leq TE + \Delta_i$ and $TE - \delta \leq y \leq TE + \delta$, where $\Delta = i \times \delta$, $i = (1, 2, 4)$ and δ is the boundary layer thickness at the trailing edge on the suction side. The results of this domain size extension are shown in Figure 6.3. The noise predictions are different between the small and medium domains, but they show no change between the medium and large domains, confirming that the medium sized domain is enough to achieve converged results. Therefore, all noise predictions in this thesis were carried out using the medium size domain, extending a distance of two boundary layer thickness (suction-side) upstream of the trailing edge to two boundary layer thickness downstream of the trailing edge, and from one boundary layer thickness above the trailing edge to one boundary layer thickness below the trailing edge.

6.3 RANS CFD results for the NACA 0012 airfoil

The selected test cases are shown in Table 6.3, with conditions matching the tripped cases of Brooks *et al.* (1989). Table 6.3 also shows the wall shear stress τ_ω and the pressure gradient parameter β. The pressure gradient was obtained from the CFD data by using a linear curve fit to the pressure for $0.95c \leq x < c$, and τ_ω was chosen as the wall shear stress at the trailing edge. Both the pressure gradient and the wall shear stress vary significantly over the surface of the airfoil, so these results are only valid near the trailing edge, and even there, they provide only a rough

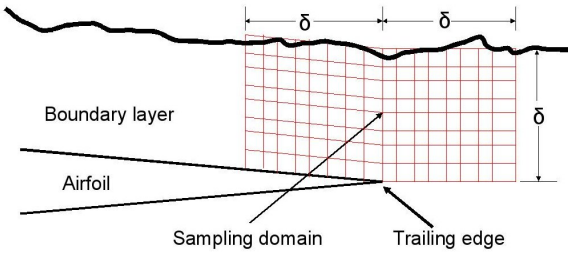

Figure 6.1: Schematic of the sampling domain used for RSNM acoustic calculations.

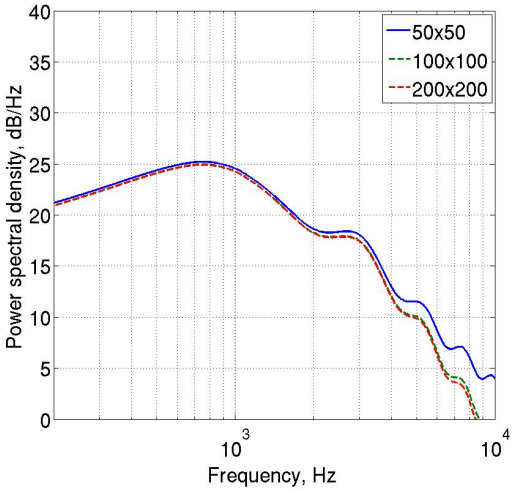

Figure 6.2: Computed acoustic power spectral density of a 15.24 cm chord NACA 0012 airfoil at a free stream velocity of 31.7 m/s ($Re_c \approx 333,000$), calculated with RSNM using three different grid resolutions.

approximation. The values of β are about one order of magnitude bigger than those of the experimental cases of Chapter 3.

6.3.1 Reynolds number effects

Figure 6.4 shows the normalized mean velocity, turbulence kinetic energy and turbulence dissipation profiles for a NACA 0012 airfoil at zero angle of attack and at Reynolds numbers ranging from $3 \times 10^5 \leq Re_c \leq 1.5 \times 10^6$. Increasing the Reynolds number has the effect of decreasing the peak turbulence intensity, as well as decreasing the peak dissipation. From the velocity profiles, it is clear that the displacement thickness is also reduced when the Reynolds number is increased. This can be corroborated by looking at Figure 6.5, which shows the boundary layer thickness, displacement thickness and momentum thickness as a function of Reynolds number. All these quantities decrease as the Reynolds number is increased.

6.3.2 Effect of angle of attack

Figure 6.6 shows the mean velocity, turbulent kinetic energy and turbulence dissipation profiles for the suction side of a NACA 0012 with a chord length of 30.48 cm ($Re_c = 1.5 \times 10^6$) at four different angles of attack.

On the suction side, increasing the angle of attack increases the displacement thick-

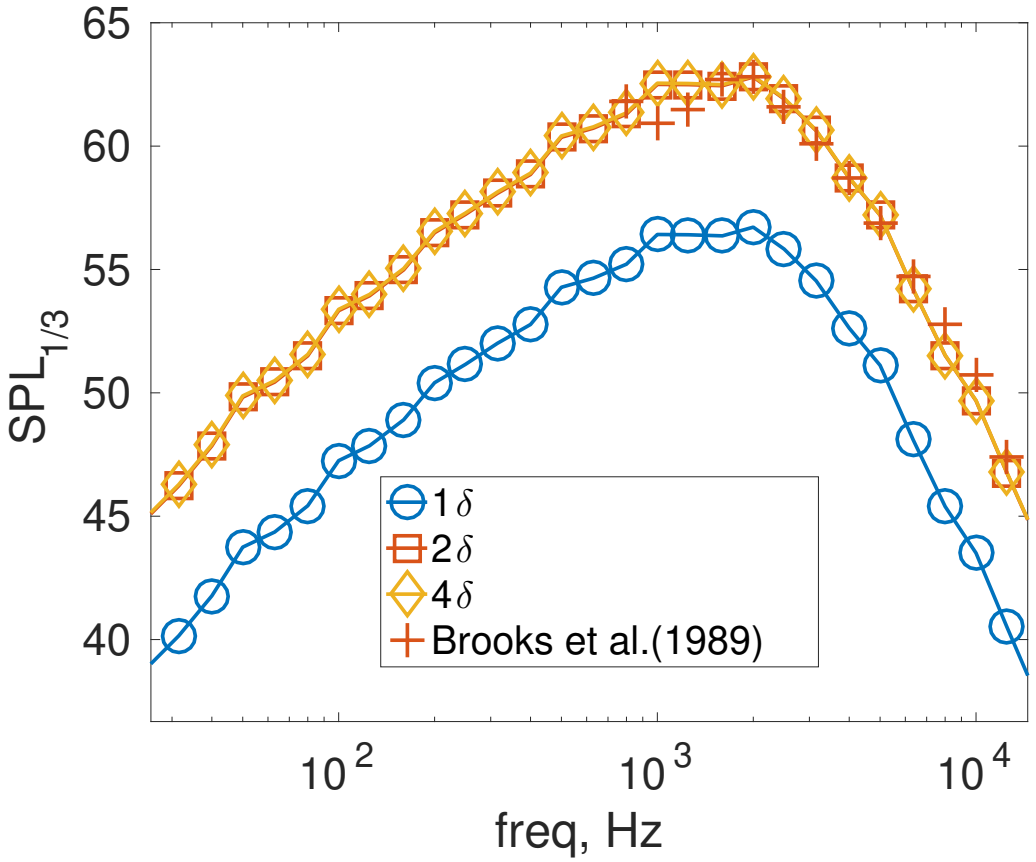

Figure 6.3: Sampling domain study for a NACA 0012 airfoil at $\alpha = 0$ at $Re_c = 1.5e^6$.

ness. From the turbulent kinetic energy profiles, it is clear that increasing the angle of attack has the effect of increasing the turbulence intensity in the boundary layer; it also thickens the boundary layer. The peak dissipation decreases with angle of attack, but the dissipation levels increase in the outer part of the boundary layer as the angle of attack is increased.

The opposite effect is observed for the pressure side, as shown in Figure 6.7. Here the velocity profiles show a decrease in the displacement thickness when the angle of attack is increased. The turbulence kinetic energy profiles show lower levels and the boundary layer is thinned as the angle of attack increases. The peak dissipation levels also increase close to the wall, but decrease in the outer part of the boundary layer.

The boundary layer thickness, displacement thickness and momentum thickness are shown in Figures 6.8. There is an increase in δ, $\delta^\star$ and θ on the pressure side as the angle of attack is increased, and the opposite is observed on the pressure side.

Table 6.1: Boundary layer parameters for a NACA 0012 airfoil at various operating conditions. τ_ω obtained at the trailing edge from CFD. Pressure gradient obtained between $0.95c \leq x < c$. Results for the suction side.

c, m	α, deg	U, m/s	Re_c	$1000\delta/c$	$1000\delta^\star/c$	$1000\theta/c$	τ_ω, Pa	β
0.3048	0.0	71.3	1.5e6	36.3635	7.1694	4.1230	2.3498	16.7393
0.3048	0.0	55.5	1.1e6	38.3839	7.6060	4.3155	1.4286	16.2278
0.3048	0.0	39.6	8.0e5	39.3940	8.2397	4.5644	0.6569	17.9687
0.3048	0.0	31.7	6.4e5	41.4140	8.7369	4.7637	0.3593	20.7548
0.2286	0.0	71.3	1.1e6	38.3839	7.6700	4.3398	2.3405	16.4810
0.2286	0.0	55.5	8.5e5	39.3939	8.1475	4.5296	1.3168	16.9731
0.2286	0.0	39.6	6.0e5	41.4141	8.8751	4.8135	0.5241	22.0665
0.2286	0.0	31.7	4.8e5	43.4343	9.3878	5.0203	0.2719	26.8366
0.3048	1.5	71.3	1.5e6	40.4042	8.3137	4.6569	2.3752	19.2033
0.3048	3.3	71.3	1.5e6	44.4446	9.7041	5.2689	2.4720	20.3413
0.3048	4.0	71.3	1.5e6	48.4849	10.8468	5.7572	2.5648	21.9135
0.2286	2.0	71.3	1.1e6	43.4343	9.3564	5.0847	2.4070	19.5498
0.2286	4.0	71.3	1.1e6	49.4948	11.5771	5.9966	2.6005	20.3544
0.2286	5.3	71.3	1.1e6	54.5455	13.4527	6.7178	2.7973	19.7884

6.4 Validation of RANS data for the NACA 0012 airfoil

For validation of the zero angle of attack cases, the CFD results for the displacement thickness, normalized by chord, are compared to the empirical BPM models (Brooks *et al.* 1989) and also with an XFOIL calculation setting turbulence transition to occur at 10% of the chord. As can be seen in Figure 6.9, the CFD results fall within the tripped and untripped experimental data of Brooks *et al.* (1989), and also follow reasonably closely the results of the XFOIL calculation, showing the same trends.

Figure 6.9 also shows the displacement thickness normalized by its value at zero angle of attack δ^*/δ_0^*, for the non-zero angle of attack cases. The CFD results are in excellent agreement with the XFOIL calculation and follow the BPM empirical curves reasonably well.

For further validation, CFD calculations of mean velocity, turbulent kinetic energy and dissipation profiles are compared to experimental data of Herr and Kamruzzaman (2013). The agreement between CFD results and experimental data is good for the mean velocity profiles at all angles of attack shown in Figure 6.10(a). The turbulent kinetic energy shows good agreement at zero angle of attack, but the CFD underpredicts the turbulent kinetic energy at greater angles of attack, as shown in

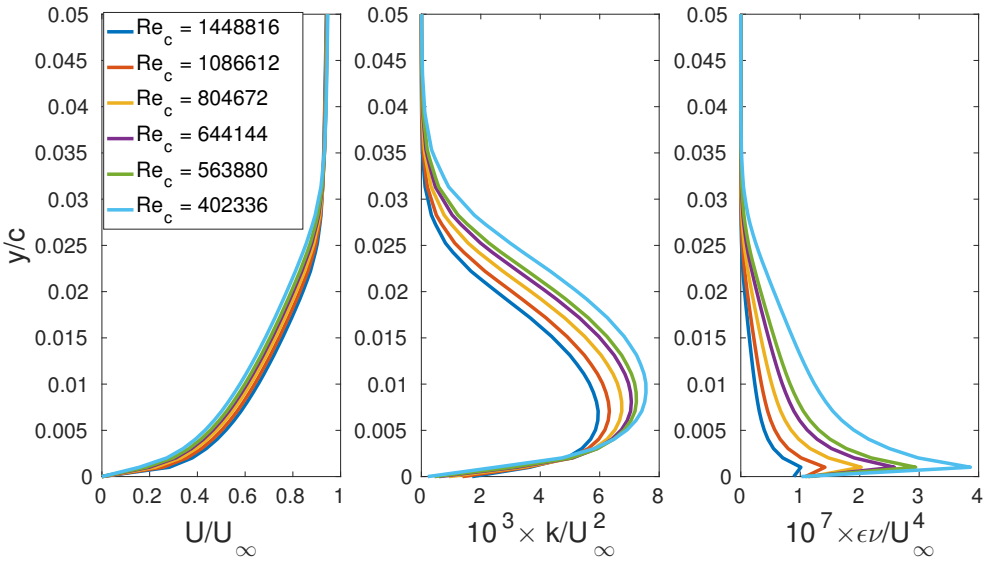

Figure 6.4: Normalized mean velocity, turbulence kinetic energy and turbulence dissipation profiles for a NACA 0012 airfoil at $\alpha = 0$ at various Reynolds numbers.

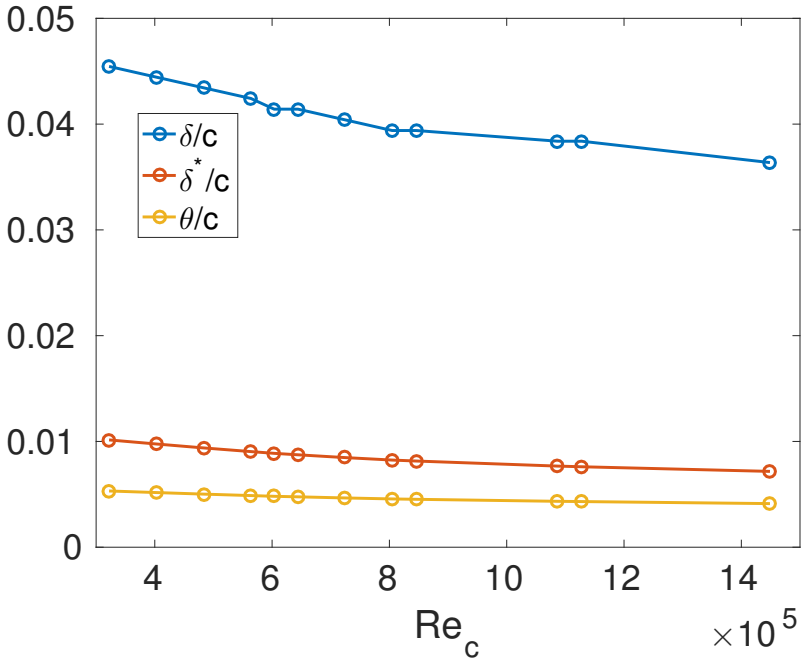

Figure 6.5: Normalized boundary layer thickness, displacement thickness and momentum thickness for a 30.48 cm chord NACA 0012 airfoil at $\alpha = 0$ at various Reynolds numbers.

Figure 6.10(b). The turbulence dissipation is greatly overpredicted at all angles of attack, in particular in the near wall region, where a large peak is observed in the CFD data, which is not present in the experimental results. This is a well known feature of two-equation RANS models (Kamruzzaman *et al.* 2012).

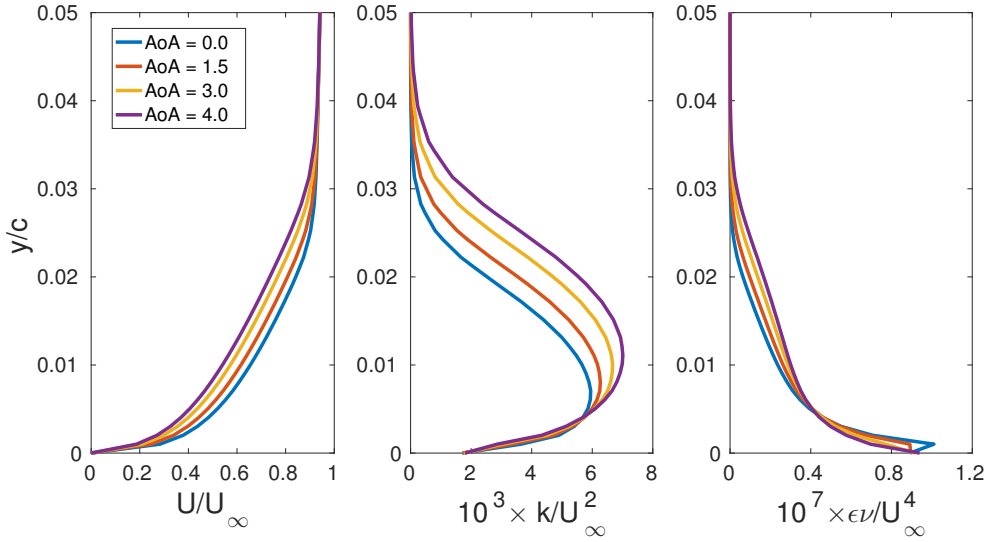

Figure 6.6: Normalized mean velocity, turbulent kinetic energy and turbulence dissipation profiles for the suction side of a 30.48 cm chord NACA 0012 airfoil at various angles of attack and at a Reynolds number of $Re_c = 1.5 \times 10^6$.

6.5 RANS CFD results for the DU-96-180 airfoil

The selected test cases are shown in Table 6.5, with conditions matching the tripped cases of Devenport *et al.* (2010). Table 6.5 also shows the wall shear stress τ_ω and the pressure gradient parameter β, both of them calculated with the same procedure used for the NACA 0012 airfoil. The values of β are of similar magnitude to those of the NACA 0012 cases described, and about one order of magnitude bigger than those of the experimental cases of Chapter 3.

Table 6.2: Boundary layer parameters for the suction side of a DU-96-180 airfoil at various operating conditions. τ_ω obtained at the trailing edge from CFD. Pressure gradient obtained between $0.95c \leq x < c$. Results for the suction side.

c, m	α, deg	U, m/s	Re_c	$1000\delta/c$	$1000\delta^\star/c$	$1000\theta/c$	τ_ω, Pa	β
0.914	3	28	1.7e6	39.3940	15.3084	6.6116	0.7435	12.3406
0.914	7	28	1.7e6	51.5151	23.9009	8.4225	0.5736	17.0759
0.914	3	40	2.4e6	36.3637	13.8914	6.2004	1.0242	18.5948
0.914	7	40	2.4e6	48.4849	21.6190	7.9751	1.3140	14.2862
0.914	3	58	3.5e6	35.3535	12.7644	5.8904	1.8436	21.5153
0.914	7	58	3.5e6	45.4546	19.5349	7.5551	2.4057	16.3283

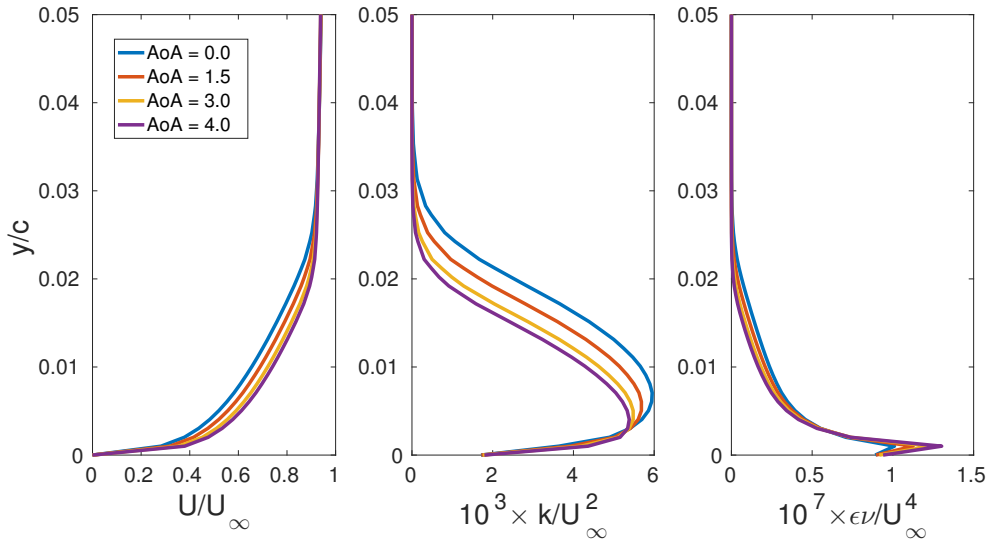

Figure 6.7: Normalized mean velocity, turbulent kinetic energy and turbulence dissipation profiles for the pressure side of a 30.48 cm chord NACA 0012 airfoil at various angles of attack and at a Reynolds number of $Re_c = 1.5 \times 10^6$. $x/c = 1$.

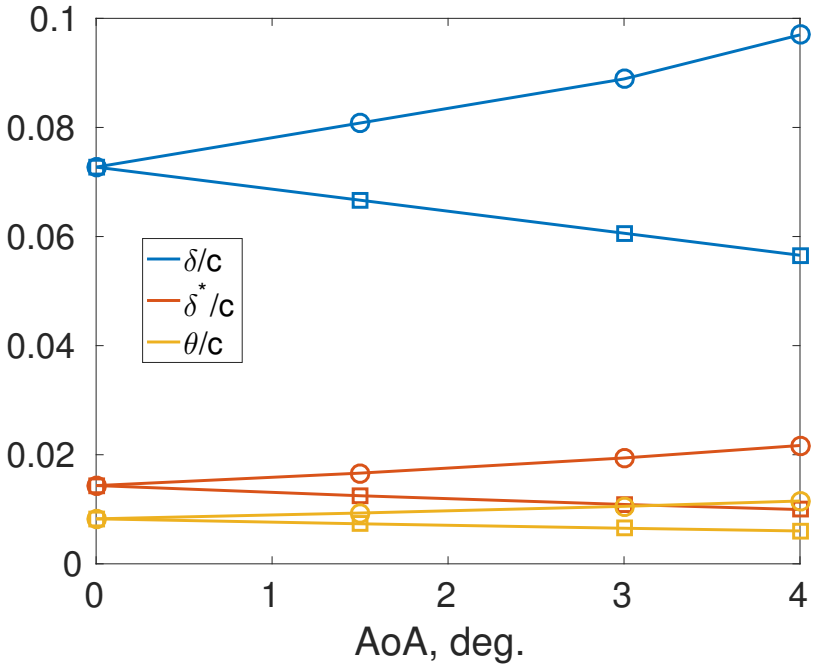

Figure 6.8: Normalized boundary layer thickness, displacement thickness and momentum thickness for a 30.48 cm chord NACA 0012 airfoil at various angles of attack and at a Reynolds number of $Re_c = 1.5 \times 10^6$. Circles: suction side. Squares: pressure side. $x/c = 1$.

6.5.1 Reynolds number effects for the Du-96-180 airfoil

Figure 6.11 shows the normalized mean velocity, turbulence kinetic energy and turbulence dissipation profiles for the suction side of 0.914 m chord DU-96-180 airfoil

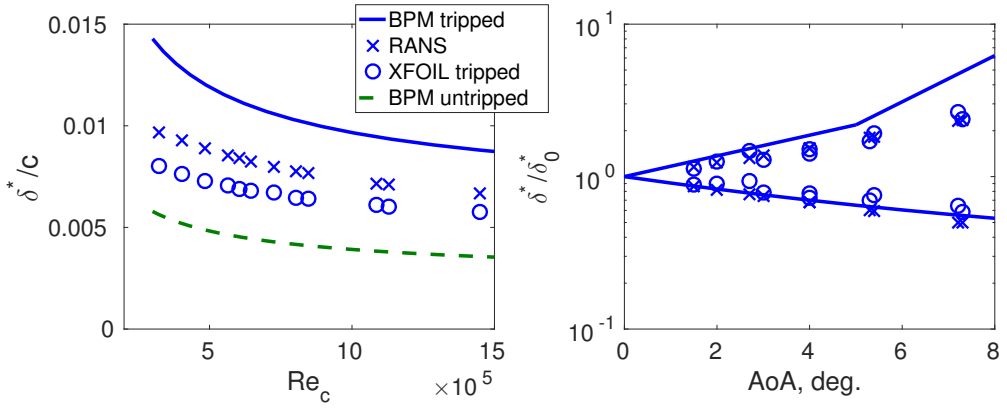

Figure 6.9: Validation of CFD results versus experimental data of Brooks *et al.* (1989). Left) Displacement thickness normalized by chord as a function of Reynolds number. Right) Displacement thickness for various NACA-0012 airfoils at a flow velocity of $U_\infty = 71.3$ m/s at various angles of attack, normalized by displacement thickness at zero angle of attack. $x/c = 0.0043$ and $x/c = 0.0057$.

at Reynolds numbers ranging from $1.7 \times 10^6 \leq Re_c \leq 3.5 \times 10^6$ at angles of attack of $\alpha = 3°$ and $\alpha = 7°$. Increasing the Reynolds number has the effect of decreasing the peak turbulence intensity, as well as decreasing the peak dissipation. From the velocity profiles one can infer that the displacement thickness is also reduced when the Reynolds number is increased. The turbulence intensity profiles also show a reduction in the boundary layer thickness as the Reynolds number is increased. This can be corroborated by looking at Figures 6.13(a) to 6.13(d), which show the boundary layer thickness, displacement thickness and momentum thickness as a function of Reynolds number. All these quantities decrease as the Reynolds number is increased.

A similar behaviour is observed on the pressure side for both angles of attack, as shown in Figure 6.12.

6.5.2 Effect of angle of attack for the Du-96-180 airfoil

For the suction side of the airfoil, increasing the angle of attack produces an increase in turbulence intensity and dissipation, a thickening of the boundary layer and an increase in displacement and momentum thickness, as shown in Figures 6.11, 6.13(a) and 6.13(b).The opposite effect is observed on the pressure side, as shown in Figures 6.12, 6.13(c) and 6.13(d).

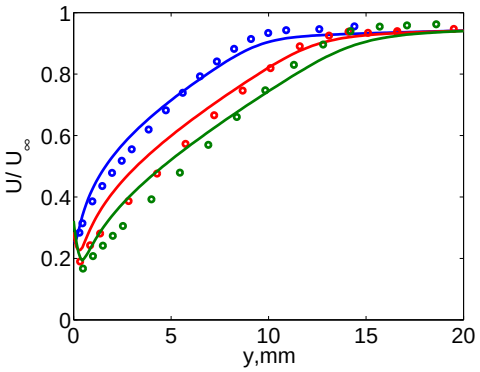

(a) Mean velocity, suction side.

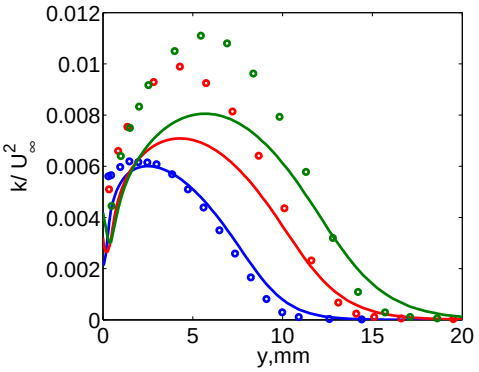

(b) Turbulent kinetic energy, suction side.

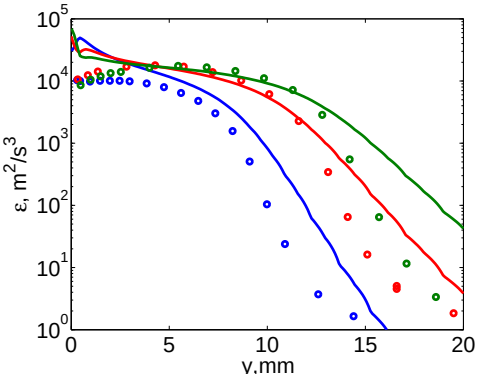

(c) Turbulence dissipation, suction side.

Figure 6.10: Mean velocity, turbulent kinetic and dissipation profiles for the suction side of a 40 cm chord NACA 0012 airfoil at a Reynolds numbers of $Re = 1.500.000$. Symbols are experimental data from Herr and Kamruzzaman (2013), solid lines are RANS CFD data. Colors blue, red and green represent angles of attack of 0, 4 and 6 degrees, respectively. $x/c = 1.0038$.

6.6 Validation of RANS data for the Du-96-180 airfoil

For validation of the CFD results, the testcase at $Re_c = 3.5 \times 10^6$ and $\alpha = 7°$ was selected, as it is the only tripped case in Devenport *et al.* (2010) for which integral boundary layer parameters and velocity measures were provided. The integral boundary layer parameters are shown in Figures 6.13(b) and 6.13(d) for both experimental and numerical results. The CFD results agree well with the experimental data for both the pressure and suction sides. Further validation is provided by comparing the mean velocity and turbulence intensity profiles, shown in Figures 6.14(a) and 6.14(b). The agreement is satisfactory for the velocity profiles, but the CFD underpredicts the turbulence intensity on both the pressure and suction sides, par-

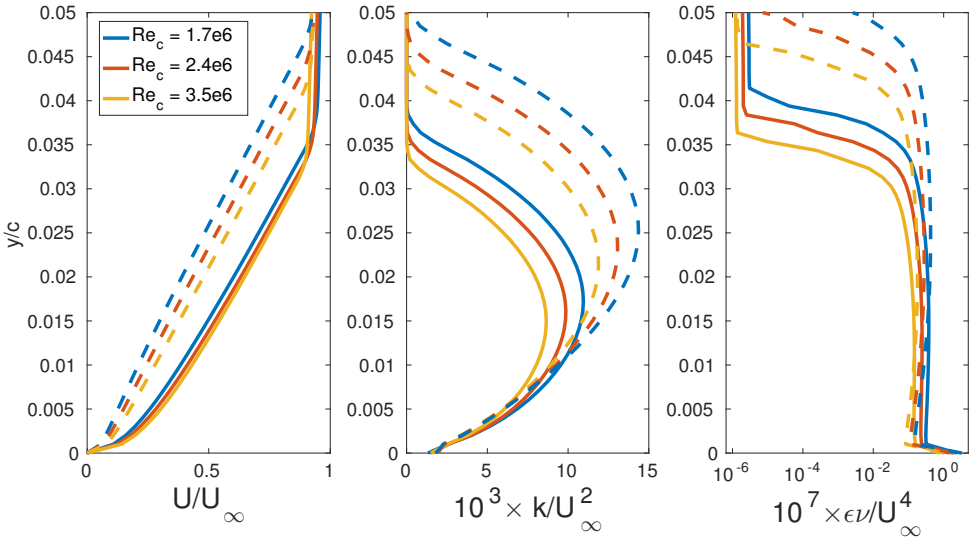

Figure 6.11: Normalized mean velocity, turbulence kinetic energy and turbulence dissipation profiles for the suction side of a DU 96-180 airfoil at various Reynolds numbers. Solid lines: AoA=3. Dashed lines: AoA=7. $x/c = 1$.

ticularly the peaks. However, the curves follow the same trends as the experimental data. The underprediction of the turbulence intensity is expected, as two equation models have difficulty predicting the correct levels of turbulent kinetic energy at non-zero angles of attack (Herr and Kamruzzaman 2013), and a similar behaviour was observed for the NACA 0012 cases for $\alpha \neq 0$.

6.7 RANS CFD results for the FP12 airfoil

The boundary layer parameters, δ, δ^* and θ calculated from the mean velocity and turbulent kinetic energy profiles provided by the CFD are compared to the experimental results of Moreau *et al.* (2011) and to the experimental results from Chapter 3 in Figure 6.15(a). The CFD results are in good agreement with the experimental data for δ^* and θ, but show some discrepancy for the boundary layer thickness δ. The percentage error for all three parameters is shown in Figure 6.15(b). In all cases, the error is significantly smaller when the CFD is compared to the experimental data of Chapter 3, as opposed to the data of Moreau *et al.* (2011). The error for δ is below 20% , less than 10% for δ^*, and the agreement for θ is very good.

For further validation, the mean velocity, turbulent kinetic energy and dissipation profiles are compared in Figures 6.16(a), 6.16(b) and 6.16(c), respectively. The mean

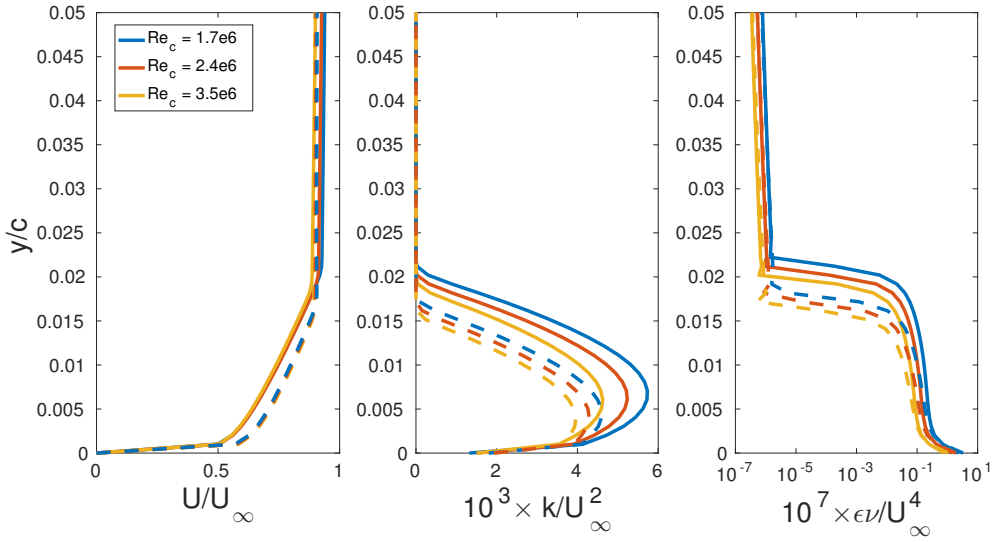

Figure 6.12: Normalized mean velocity, turbulence kinetic energy and turbulence dissipation profiles for the pressure side of a DU 96-180 airfoil at various Reynolds numbers. Solid lines: AoA=3. Dashed lines: AoA=7. $x/c = 1$.

velocity profiles are very similar for both experimental data sets; however, the CFD results follow the experimental data of Chapter 3 more closely. This is possibly due to the better resolution achieved in the experimental measurements of Chapter 3, where the chord of the airfoil was five times bigger than that of Moreau *et al.* (2011), providing a much thicker boundary layer, and hence a much smaller probe diameter to δ ratio. This difference is more pronounced in the kinetic energy profiles, where the effects of spatial averaging are more evident, resulting in a smaller peak in the inner boundary layer. It must also be noted that in the present experiments it was possible to measure closer to the trailing edge; however, the effects of a small difference in x/c are minor and only limited to the inner part of boundary layer or near wake, as shown in Figures 6.16(a) to 6.16(c). The CFD severely underpredicts the kinetic energy, also showing a more narrow profile, which results in a smaller boundary layer. Figure 6.16(c) compares the dissipation obtained from CFD with the experimental data of Chapter 3. The CFD overpredicts the dissipation, which is consistent with the underprediction of kinetic energy. The peak dissipation is reasonably well predicted.

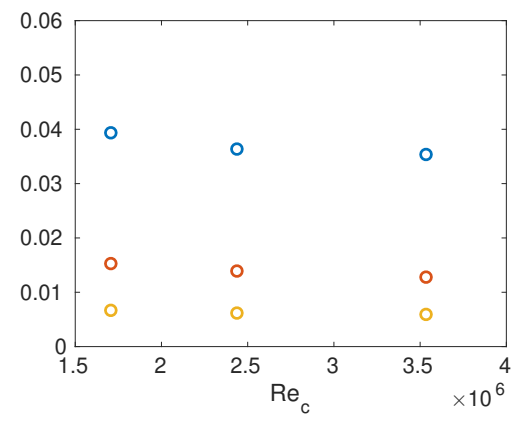

(a) AoA=3 deg, Suction side.

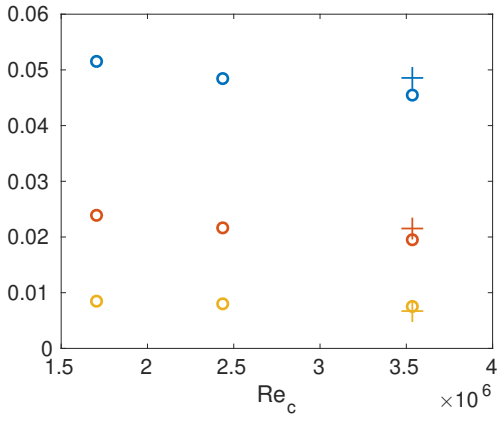

(b) AoA=7 deg, Suction side.

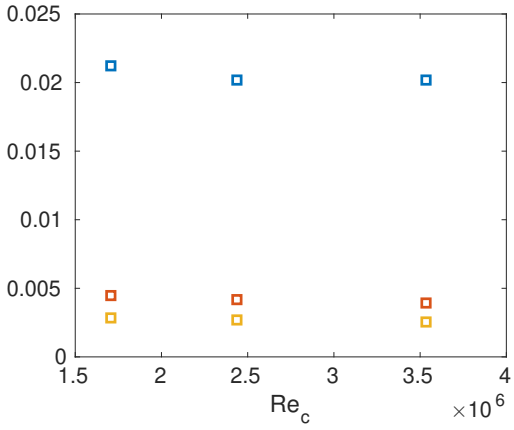

(c) AoA=3 deg, Pressure side.

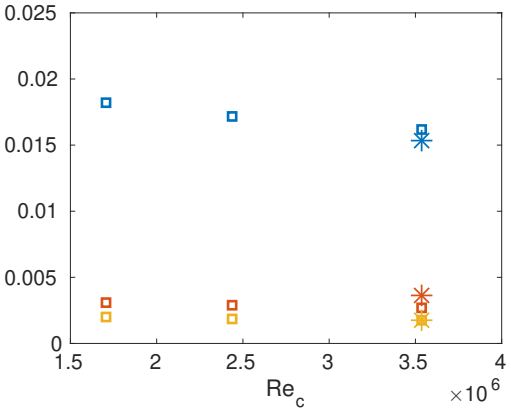

(d) AoA=7 deg, Pressure side.

Figure 6.13: Integral boundary layer parameters for a DU 96-180 airfoil at various Reynolds numbers. Blue: δ/c, red: δ^*/c, yellow: θ/c. Circles: suction side, squares: pressure side. Experimental data suction side: $+$, experimental data pressure side: $*$. $x/c = 0.0021$. (Devenport *et al.* 2010).

6.8 Acoustic results fo the NACA 0012 airfoil

This section shows the acoustic predictions for the baseline RSNM and several modifications of RSNM. The baseline model uses a Gaussian autospectrum model and a Gaussian coherence model with a length scale defined by $\ell_s = k/\epsilon^{3/2}$, and empirical coefficients $c_\tau = 0.016 \times U_\infty + 0.8$ and $A_1 = 1.9 \times 10^{-6}$. These parameters were determined by best fit to the data of Brooks *et al.* (1989). The modifications are constructed by changing either the autospectrum model, the spatial coherence model, or both. A detailed description of the autospectrum and coherence models is given in Chapter 4. Table 6.14 shows the different configurations employed in all noise predictions.

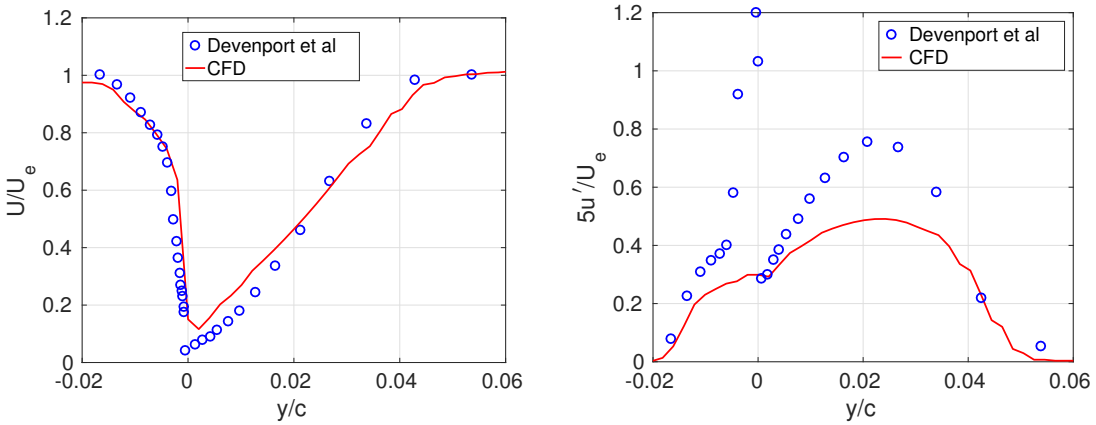

(a) Mean velocity . (b) Turbulence intensity.

Figure 6.14: Mean velocity and turbulence intensity profiles for a DU 96-180 airfoil at $R_e = 3.14 \times 10^6$ at $\alpha = 7°$. Symbols: experimental data from (Devenport *et al.* 2010). Solid lines: CFD results. $x/c = 0.0021$.

The first modification (Mod 1) uses the same Gaussian coherence model and autospectrum as the baseline model, but uses an iterative process to calculate the coefficients c_τ and A_1 at each point in the sampling domain. The coefficients were initially given a value of 1 and the turbulent kinetic energy k was calculated by integrating the autospectrum over all wave numbers using Equation **??**. An error function was defined as:

$$error = 100(k_{RANS} - k_{calculated})/k_{RANS}. \tag{6.1}$$

A Matlab script then modified the coefficients and repeated the process. The iterating process was stopped when the error was below 0.1% or 800 iterations were performed, whichever happened first. In order to incorporate the dissipation into the optimization process, an alternative error function can be defined as:

$$\begin{aligned} error_1 &= 100(k_{RANS} - k_{calculated})/k_{RANS} \\ error_2 &= 100(\epsilon_{RANS} - \epsilon_{calculated})/\epsilon_{RANS} \\ error &= error_1 + error_2. \end{aligned} \tag{6.2}$$

This approach produced the same coefficients as the one defined by Equation 6.1, and due to its simplicity, Equation 6.1 was preferred.

The second modification (Mod 2) uses an autospectrum model proposed by Pope (2000). The empirical coefficients C_η and C_L are found by the same process described for mod 1.

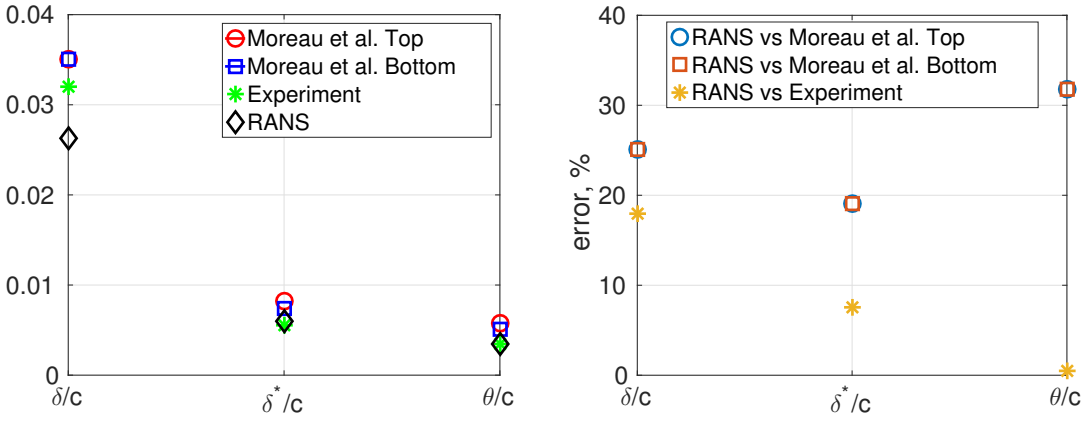

(a) Boundary layer parameters.

(b) Error.

Figure 6.15: Boundary layer parameters for The FP12 airfoil at $R_e \approx 5 \times 10^5$ at $\alpha = 0°$ and percentage error. Experimental data taken from Moreau *et al.* (2011) ($x/c = 0.003$) and Chapter 3 ($x/c = 0.00083$).

The third modification (Mod 3) combines Gavin's spatial coherence model and the baseline Gaussian autospectrum (fixed coefficients). The length scale is taken to be a function of the boundary layer thickness, $\ell_s = 0.35\delta$. The fourth modification (Mod 4) is the same as Mod 3, except that the length scale is now calculated for each point in the boundary layer, and is a function of the turbulent kinetic energy and dissipation, $\ell_s = k^{3/2}/\epsilon$.

Modifications 5, 6 and 7 introduce an anisotropic coherence model described in Chapter 4. The empirical coefficients c_{ℓ_x} and c_{ℓ_y} are shown in table 4.2. Modifications 5, 6 and 7 use the coefficients for Cases 2, 1 and 3, respectively.

For all modifications, the value of the amplitude coefficient A_0 was found by adjusting the amplitude to match the experimental data of the Brooks *et al.* (1989) case at $Re_c = 1.5 \times 10^6$. The values of A_0 for each case can be found in Table 6.14.

6.8.1 Zero angle of attack

Figures 6.17(a) and 6.17(b) show the third octave band spectra predicted by the baseline model, Mod 1 and Mod 2, compared to the experimental data of Brooks *et al.* (1989) at $U_\infty = 71.3$ m/s for chords of 30.48 cm and 22.86 cm, respectively. The baseline model follows the experimental data closely, matching the location of the peak, while Mod 1 and Mod 2 predict a peak at a higher frequency. Mod 1 predicts the correct spectral shape, but there is a shift of the spectra to higher

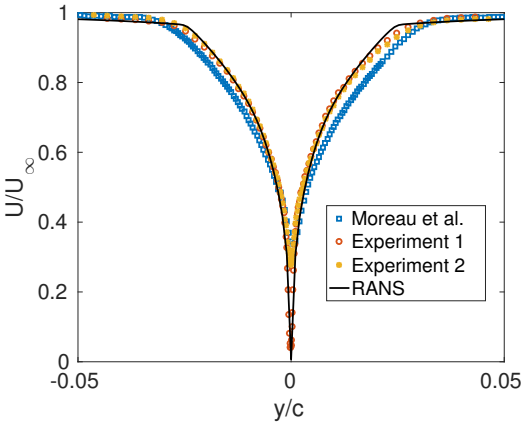

(a) Mean velocity .

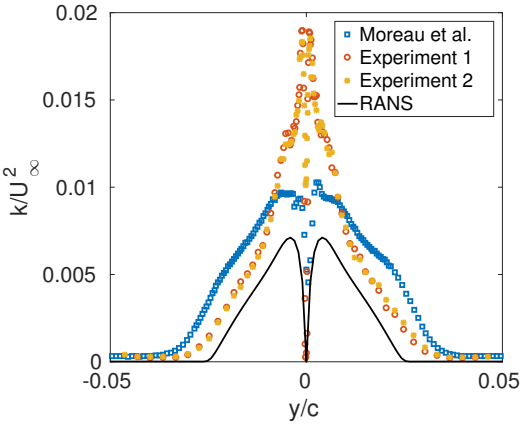

(b) Turbulence kinetic energy.

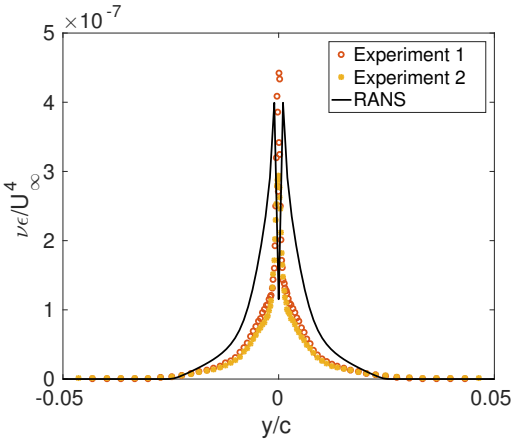

(c) Turbulence dissipation.

Figure 6.16: Mean velocity, turbulence kinetic energy and dissipation profiles for the FP12 airfoil at $R_e \approx 5 \times 10^5$ at $\alpha = 0°$. Blue: experimental data from Moreau *et al.* (2011) at $x/c = 0.0030$. Red: experimental data from Chapter 3 at $x/c = 0.0008$. Yellow: experimental data from Chapter 3 at $x/c = 0.0042$. Solid lines: CFD results at $x/c = 0$.

frequencies. Mod 2 shows a much steeper decay after the peak, which does not conform to the trend in the experimental data.

A similar behaviour is observed for all other test cases, as shown in Figures 6.17(c) to 6.17(h). In all these cases, the baseline model provides an accurate representation of the experimental data, with the amplitude scaling correctly as a function of free stream velocity.

Mod 1 consistently shows a shift in frequency, and even though it predicts a lower amplitude with smaller free stream velocity, it significantly overpredicts the sound levels. Mod 2 predicts the correct peak levels for the different velocities, but it incorrectly determines the frequency of the peak and produces the wrong spectral

shape. Both Mod 1 and Mod 2 rely on an iterative process to determine model parameters which give the autospectrum its shape. This is done by integrating the autospectrum over all frequencies to calculate the kinetic energy, and then minimizing the difference between this value and the kinetic energy obtained form RANS. It is possible to obtain the same kinetic energy by integrating vastly different spectral shapes, therefore it is possible that the optimization algorithm is finding a local minimum rather than the true global minimum, resulting in an incorrect prediction of the peak frequency and the shape of the noise spectrum. Another source of error is the inaccurate prediction of the dissipation (ϵ) by RANS, as shown in Figure 6.10(c). This will affect the length scales, time scales and amplitude in both the Gaussian autospectrum model and the Pope autospectrum model, leading to erroneous noise predictions.

Due to the poor performance of these alternative autospectrum models, they will not be used in combination with the rest of the spatial coherence models.

6.8.1.1 Effect of changing the spatial coherence model

In this section, the effect of changing the spatial coherence model is investigated. For this purpose, the baseline autospectrum model will be used in all calculations in combination with the alternative spatial coherence models, and compared to the baseline model and the experimental data of Brooks *et al.* (1989).

Figures 6.18(a) to 6.18(h) show the acoustic predictions for a NACA 0012 at zero angle of attack and at various flow speeds compared to the experimental data of Brooks *et al.* (1989).

Both Mod 3 and Mod 4 follow the shape of baseline model very closely, but with slightly decreased amplitudes. All models scale appropriately with free stream velocity.

Figures 6.19(g) to 6.19(h) show the predictions of Mods 5, 6 and 7 for a NACA 0012 at zero angle of attack for a range of flow speeds, and compare them to the baseline model and the experimental data of Brooks *et al.* (1989).

Mod 5 and 7 are indistinguishable from the baseline model for frequencies up to 4 kHz. Above this frequency, both Mod 5 and Mod 6 predict higher levels than the baseline model, showing a slower decay with frequency. This effect is much more pronounced for Mod 7.

Mod 6 is indistinguishable from the baseline model for frequencies below 500 Hz. Above this frequency, Mod 6 predicts a smaller amplitude, but a slower decay rate, which results in higher levels above approximately 4 kHz.

6.8.2 Non-zero angle of attack

Figures 6.20(a) and 6.20(b) show the noise predicted by the baseline model for a NACA 0012 airfoil in a free stream velocity of 71.3 m/s at various angles of attack, for chords of 30.48 cm and 22.86 cm, respectively. The model shows little sensitivity to a change in the angle of attack, and provides a good prediction for frequencies above 2 kHz. There is a slight increase in amplitude with angle of attack for frequencies below 1 kHz and a slightly larger decrease in amplitude for frequencies above 1 kHz. The experimental data show a marked increase in low frequency noise as the angle of attack increases, showing a distinct peak. This effect is not captured by the model. It is hypothesised that the large broadband peak occurring in the noise spectrum at higher angles of attack is caused by vortex shedding or other

noise mechanisms of a different nature than broadband trailing edge noise. These broadband peaks are not present in the experimental data of Devenport et al.(2010), which was captured using beamforming techniques, focusing on the trailing edge and excluding extraneous sources. Their results show almost no difference in the noise generated at different angles of attack when the airfoil is tripped; however, they note that for untripped conditions, thre was vortex shedding at all angles of attack tested, and the acoustic results changed significantly with angle of attack. Devenport *et al.* (2010) also found that in their data, the noise at low frequencies for high angle of attack cases is dominated by vortex shedding for the untripped boundary layers. They found that tripping the boundary layer reduces the vortex shedding, but does not eliminate it, and for some frequencies, it barely affects it.

Figures 6.21(a) and 6.21(b) show the noise predictions for RSNM Mod 3. The predictions follow a very similar pattern as the baseline model, showing low sensitivity to angle of attack variations, except for a small increase at low frequencies and a slightly larger decrease in amplitude for frequencies over 1 kHz. The same features are observed in the predictions of RSNM Mod 4, shown in Figures 6.22(a) and 6.22(b).

Mod 5, 6 and 7 shows a similar behaviour as the baseline model and Mods 3 and 4, namely a small sensitivity to angle of attack and an inability to reproduce the low frequency peaks. An important difference is an increase in amplitude with angle of attack for frequencies over 8 kHz, as shown in Figures 6.23(a) to 6.25(b).

Mod 2 and 3 are not shown, as they suffer from the same problems discussed in the zero angle of attack cases.

6.9 Acoustic results for the DU-96-180

Experimental data were sourced from Devenport *et al.* (2010), where the boundary layer was tripped by a serrated tape. Two angles of attack are presented at three free stream velocities. Devenport *et al.* (2010) plot both angles of attack and multiple runs on the same figure, making it impossible to discern which curve corresponds to which angle of attack; however, all the results follow the same trends. The data are presented as three clouds of points, each corresponding to a different free stream velocity, but including both angles of attack. The data are presented in 1/12 octave bands.

Figure 6.26(a) shows the results for the baseline model. The model captures the

shape of the spectra correctly, and also captures the increment in amplitude with free stream velocity. There is a small underprediction of the velocity spectrum for the 58 m/s case; however, Devenport *et al.* (2010) note that in many cases at the higher speed, trailing edge noise was difficult to observe from the noise maps, so it is possible that the discrepancies are caused by noise mechanisms other than trailing edge noise. The angle of attack has a weak effect on the noise predictions, which is within the spread shown in the experimental data. The effects become more pronounced at higher frequencies, where there are no experimental data to compare it with.

Figures 6.26(b) and 6.26(c) show the results for Modifications 3 and 4, respectively. The results are almost indistinguishable from the baseline model and from each other below 1 kHz, but Modification 3 follows the experimental data more closely above 1 kHz, showing a steeper decline with frequency. There are more pronounced differences between the models above 2 kHz, which increase with frequency.

Figures 6.26(d), 6.26(e) and 6.26(f) show the results for Modifications 5, 6 and 7, respectively. All these modifications behave similarly for frequencies below 1 kHz, producing adequate results, but departing from the experimental data much quicker after 1 kHz, and showing large differences to each other as frequency increases.

Figure 6.27 compares the experimental data of Herr and Kamruzzaman (2013) with the noise predictions of the baseline model and five model modifications in third-octave bands. The baseline model shows excellent agreement with the experimental data, staying within 3 dB from the experimental data for 1 kHz $\leq f \leq$ 16 kHz. Modification 4 shows the same shape as the baseline model, but with a decreased amplitude of approximately 2 dB. Modification 3 is indistinguishable from Modification 4 for $f \leq 4$ kHz, but shows a more pronounced decay with frequency above 4 kHz, departing from the experimental data. This gives support to the idea of using a local length scale $\ell_s = k^{3/2}/\epsilon$ in the coherence model, as opposed to the global length scale $\ell_s = 0.35\delta$ used in Modification 3.

Modification 5 agrees well with the experimental data up to $f = 8$ kHz, at which point it predicts a slower decay with frequency, resulting in an overprediction of the noise levels. A similar effect is observed for Modifications 6 and 7, but with the slower decay starting at $f = 4$ kHz. This could be the result of neglecting the frequency dependency of the coherence function, which was a core assumption of the semi-empirical cross-spectrum model developed in this thesis. The coherence decays rapidly as a function of frequency, and approximating it by its value at $\omega = 0$ will inevitably cause errors, which are more pronounced as the frequency increases.

This is consistent with the results observed in Figure 4.2(b), which displays the measured cross-spectrum and the cross-spectrum calculated using the approximated coherence.

6.10 Acoustic results for the FP12 airfoil

The acoustic predictions of the baseline model and several modifications are shown in Figure 6.28 and compared to the experimental data of Moreau *et al.* (2011). All the predictions are significantly lower than the experimental data; however, they all show the correct slope for frequencies above 2 kHz, as shown by offsetting the experimental data by -15 dB. All predictions show a peak between 1 kHz and 2 kHz, and a decay in amplitude as frequency is decreased below this point. The experimental curve does not follow this trend, showing the highest levels close to 300 Hz, and decaying with increasing frequency.

All models used the offsets listed in Table 6.14.

It is worth noting that the peak in the spectrum at 1.5 kHz in the experimental data is likely caused by noise mechanisms other than trailing edge noise, as it was present at the same frequency for all cases tested by Moreau *et al.* (2011), which ranged from 15 ms^{-1} to 38 ms^{-1}, and the frequency of the peak was independent of the flow velocity. The high levels of low frequency noise were attributed by Moreau *et al.* (2011) to boundary layer instabilities and vortex shedding induced by the strong adverse pressure gradient in the steep angled trailing edge region. These noise mechanisms are not taken into account in the present noise prediction model, which explains some of the discrepancies between the predictions and the experimental data. However, this does not explain the 15 dB offset required to match the data at high frequency. The underprediction of noise levels can be related to the underprediction of turbulent kinetic energy by the RANS CFD, and an overprediction of dissipation; however, this is unlikely to account for 15 dB. Other factors contributing to the underprediction of the noise spectrum are an inaccurate prediction of the turbulence length scales and an inaccurate modelling of the turbulence spectrum. These factors are examined in the following sections.

6.11 Effect of length scales on acoustic results

The length scales affect the amplitude of the velocity spectrum, and can therefore affect the noise levels predicted by RSNM. Figure 6.29 shows the length scales measured for the experimental cases and compares them to the values calculated from RANS as $L = c_\ell k^{3/2}/\epsilon$. The length scale parameter is $c_\ell = 1$ for the baseline model, which produces an underprediction of the length scales when compared with the experimental data. Three values of c_ℓ are tested to match the experimental data and investigate the effects of the length scale in the noise predictions. Increasing c_ℓ produces a more accurate length scale for $y/\delta \leq 1$, but creates an artificial increase of the length scale outside of the boundary layer; however, this effect is not important for the noise calculations, as the data used in RSNM is sampled within the boundary layer.

Figure 6.30 shows the effects of increasing the length scale coefficient in the noise predictions. There is an increase in noise levels of up to 3 dB at 1 kHz, but this level does not change when the coefficient is increased past a value of $c_\ell = 2.5$. There is a small decrease in levels for frequencies over 4 kHz when c_ℓ is increased, which slightly changes the spectral shape.

Although an underprediction of the length scale has an effect on the noise predictions, this effect can only account for up to 3 dB and does not account for the large difference in low frequency noise between the experiment and the model predictions.

6.12 Effect of underpredicting turbulent kinetic energy and dissipation.

To investigate the effects of the underprediction of turbulent kinetic energy and overprediction of dissipation, experimental data for these quantities were used in the noise calculations instead of the RANS CFD data. To accomplish this, it was assumed that the data in the sampling domain was the same as the trailing edge data. The calculations were performed using the same sampling points as for the RANS based calculations, and the values for U, k and ϵ were interpolated from the experimental data at the trailing edge. The noise calculations were performed using the baseline model. The resulting noise predictions are compared to the experimental data of Moreau *et al.* (2011) and to RANS based predictions in Figure 6.31. The

experimental flow data creates a different noise spectrum, with higher levels of low frequency noise, and a steep decline in levels for $2000Hz < f < 5000Hz$, followed by a plateau for $f > 5000Hz$. The noise predictions are still 15 dB under the experimental data of Moreau *et al.* (2011), which means the underprediction of k and overprediction of ϵ by the RANS CFD cannot account for the underprediction of the noise levels.

6.13 Effect of incorrectly modelling the turbulence spectrum

The autospectrum model is not only responsible for the spectral shape of the noise prediction, but also affects the amplitude significantly. Therefore, an accurate modelling of the autospectrum is required to obtain accurate noise predictions. Figure 6.32 shows the baseline autospectrum model calculated using experimental data (U, k and ϵ) as inputs and compares it with the autospectrum measured experimentally. The spectra have been normalized as $E_s = E/(\epsilon\nu^5)^{(1/4)}$, and are plotted in decibels as $10log_{10}(E_s)$ for selected points in the boundary layer. The model has been offset by +50 dB for easier visualization. Not only are modelled spectra 50 dB under the experimental values, they are also very different in shape, with the model decaying much faster with frequency than the experimental data. This can explain the underprediction of noise by RSNM, and also the different spectral shape between the noise predictions and the experimental data. The 50 dB difference is probably offset by other sources of error, such as errors in the coherence function, errors in the length scale and inaccuracies in the flow data predicted by RANS, resulting in the 15 dB difference between the noise predictions and the experimental noise spectrum. It is unclear at the moment how the RSNM can perform so badly for the FP12 airfoil, yet so well for the DU-96-180 and the NACA 0012, when the same cross-spectrum models are used. Experimental data on the velocity spectrum at various locations in the boundary layer of both a DU-96-180 and the NACA 0012 airfoil would be a valuable resource to improve and validate the autospectrum models, as well as to elucidate the causes behind their extremely poor performance.

6.14 Summary

In this chapter, several variations of the RSNM method were applied to a NACA 0012 airfoil at a range of operating conditions. The results for the NACA 0012 airfoil show that the baseline model follows the experimental data accurately for zero angle of attack cases. For non-zero angle of attack, the baseline model provides a good prediction of the noise for frequencies above 2 kHz, but fails to predict the large low frequency peaks present in the experimental data for angles of attack of four degrees or more. It is argued that these peaks are due to vortex shedding, a noise generation mechanism that is not included in the physics of the RSNM model.

Two modifications were tested for the autospectrum model, both of which used an optimization algorithm to determine the empirical coefficients in the autospectrum model. Both of these modifications showed a tendency to shift the energy to higher frequencies, resulting in the incorrect spectral shape. It is hypothesised that this is caused by the algorithm finding a local minimum which does not correspond to the true solution.

Three alternative spatial coherence models were tested in combination with the baseline autospectrum model. All of them produced very similar results, indicating that the model is most sensitive to the autospectrum, as this is the part that controls the frequency dependence and, to a large extent, it also controls the amplitude of the predictions. Of the three coherence models tested, only the anisotropic exponential model required an adjustment of the amplitude parameter A_0.

The anisotropic exponential model showed an overprediction of high frequency levels, which was most pronounced when using the coefficients obtained for Case 1. A better fit was obtained when using the coefficients obtained for Case 2.

In conclusion, the baseline model produced accurate results, following the trends in the experimental data and scaling correctly with free stream velocity. The model does not capture the large low frequency peaks present in the experimental data for angles of attack of four degrees or more. The different modifications tested did not produce improvements to the acoustic predictions.

For the Du-96-180, experimental data sets were taken from Devenport *et al.* (2010) and Herr and Kamruzzaman (2013) for comparison. The results show that the baseline model follows the experimental data accurately for the 28 m/s and 40 m/s cases of the Devenport *et al.* (2010) data for both angles of attack. The model slightly underpredicts the levels for the 58 m/s case.

The use of Gavin's coherence model (Modifications 3 and 4) also produced excellent results, following the data of Devenport *et al.* (2010) very closely. Similarly to the baseline model, there was a slight underprediction of the 58 m/s case.

The anisotropic exponential model (Modifications 5, 6 and 7) produced good predictions at lower frequencies, but departed form the experimental data above 1 kHz.

When compared to the experimental data of Herr and Kamruzzaman (2013), the baseline model predicts the spectral shape and levels accurately. Modifications 3 and 4 slightly underpredict the levels, but produce a very similar spectral shape to the baseline model. For frequencies above 4 kHz, Modification 3 decays too fast and underpredicts the noise levels.

Modifications 5, 6 and 7 predict the correct levels below 4 kHz, but tend to overpredict the noise for higher frequencies, particularly Modifications 6 and 7.

The results for the FP12 airfoil are very dissapointing. The model underpredicts the noise levels by 15 dB, although it produces the correct spectral shape for frequencies above 2 kHz. The underprediction of noise levels can be related to the underprediction of turbulent kinetic energy, an overprediction of dissipation by the RANS CFD, an underprediction of the turbulent length scales, and mostly to the large difference between the turbulence autospectrum model and the experimental autospectrum. It is unclear at the moment why RSNM performs so badly for the FP12 airfoil, yet so well for the DU-96-180 and the NACA 0012, when the same cross-spectrum models are used. Experimental measurements of the velocity spectrum at in the boundary layer of both a DU-96-180 and the NACA 0012 airfoil are needed to improve and validate the autospectrum models, and to understand the reasons for their poor performance. What is abundantly clear is that a more accurate turbulence spectrum model is required to improve the performance of RSNM, and this requires significant further research.

Table 6.3: RSNM variations

	γ	E	ℓ_s	empirical parameters	offset (dB)
baseline	Gaussian	Gaussian	$k^{3/2}/\epsilon$	$c_\tau = 0.016 \times U_\infty + 0.8$ $A_1 = 1.9 \times 10^{-6}$	0
Mod 1	Gaussian	Gaussian	$k^{3/2}/\epsilon$	found by $\int E(\kappa)d\kappa = k$	-47.8
Mod 2	Gaussian	Pope Spectrum	$k^{3/2}/\epsilon$	found by $\int E(\kappa)d\kappa = k$	-68
Mod 3	Gavin (Exponential)	Gaussian	0.35δ	$c_\tau = 0.016 \times U_\infty + 0.8$ $A_1 = 1.9 \times 10^{-6}$	0
Mod 4	Gavin (Exponential)	Gaussian	$k^{3/2}/\epsilon$	$c_\tau = 0.016 \times U_\infty + 0.8$ $A_1 = 1.9 \times 10^{-6}$	0
Mod 5	Anisotropic, Case 2(Exponential)	Gaussian	$k^{3/2}/\epsilon$	$c_\tau = 0.016 \times U_\infty + 0.8$ $A_1 = 1.9 \times 10^{-6}$	8
Mod 6	Anisotropic, Case 1(Exponential)	Gaussian	$k^{3/2}/\epsilon$	$c_\tau = 0.016 \times U_\infty + 0.8$ $A_1 = 1.9 \times 10^{-6}$	12.73
Mod 7	Anisotropic, Case 3(Exponential)	Gaussian	$k^{3/2}/\epsilon$	$c_\tau = 0.016 \times U_\infty + 0.8$ $A_1 = 1.9 \times 10^{-6}$	12.06

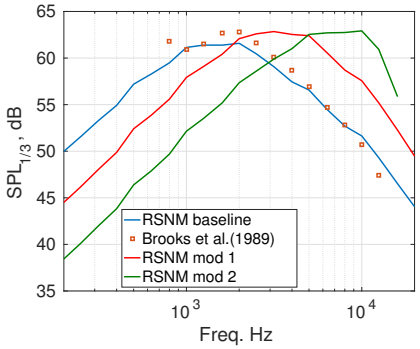

(a) Chord:30.48 cm, $U_\infty = 71.3m/s$.

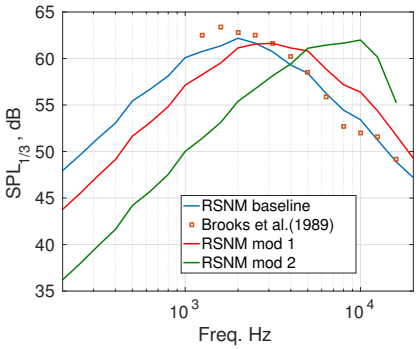

(b) Chord:22.86 cm, $U_\infty = 71.3m/s$.

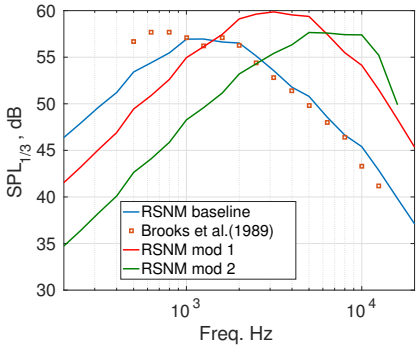

(c) Chord:30.48 cm, $U_\infty = 55.5m/s$.

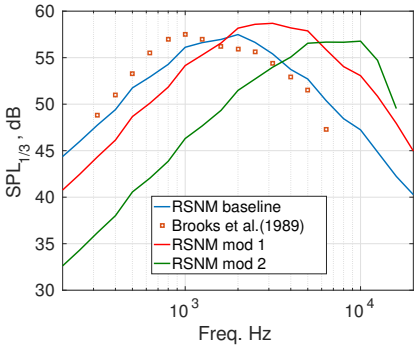

(d) Chord:22.86 cm, $U_\infty = 55.5m/s$.

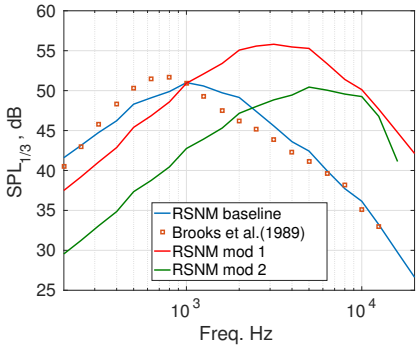

(e) Chord:30.48 cm, $U_\infty = 39.6m/s$.

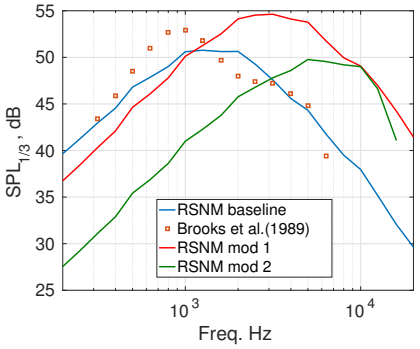

(f) Chord:22.86 cm, $U_\infty = 39.6m/s$.

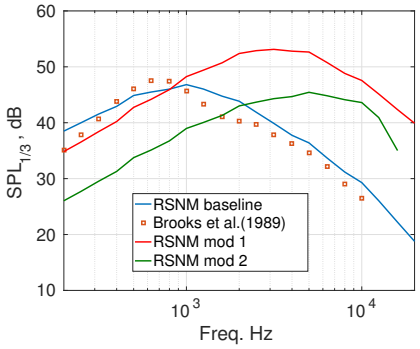

(g) Chord:30.48 cm, $U_\infty = 31.7m/s$.

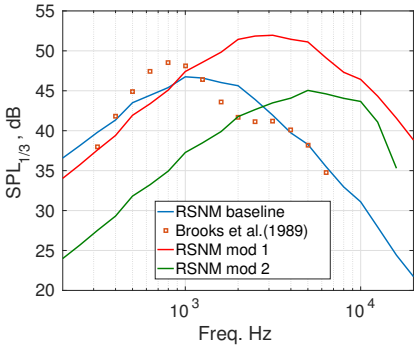

(h) Chord:22.86 cm, $U_\infty = 31.7m/s$.

Figure 6.17: Acoustic predictions (solid lines) and experimental data of Brooks et al.(1989) for a NACA 0012 airfoil at $\alpha = o$.

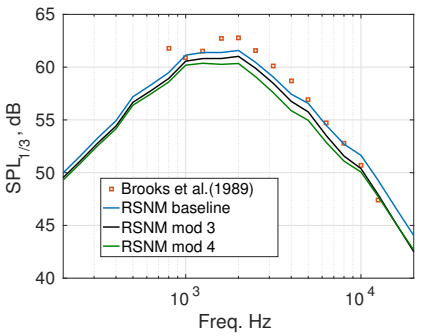

(a) Chord:30.48 cm, $U_\infty = 71.3m/s$.

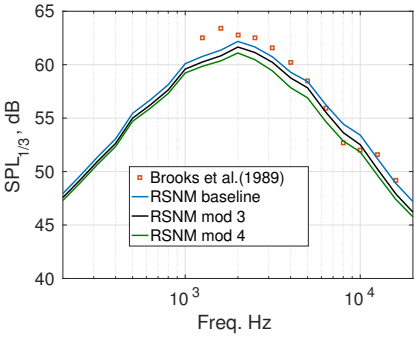

(b) Chord:22.86 cm, $U_\infty = 71.3m/s$.

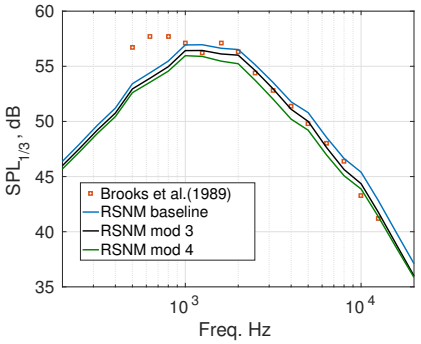

(c) Chord:30.48 cm, $U_\infty = 55.5m/s$.

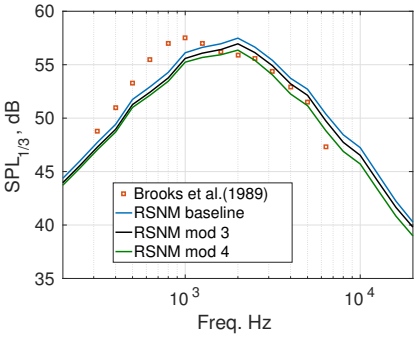

(d) Chord:22.86 cm, $U_\infty = 55.5m/s$.

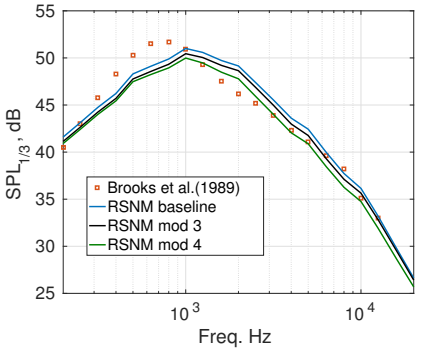

(e) Chord:30.48 cm, $U_\infty = 39.6m/s$.

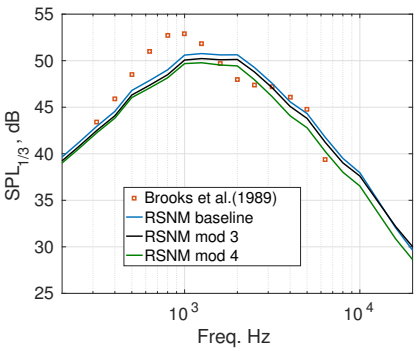

(f) Chord:22.86 cm, $U_\infty = 39.6m/s$.

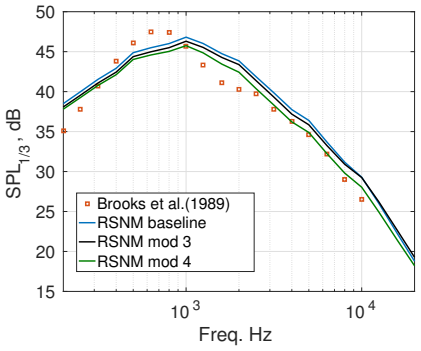

(g) Chord:30.48 cm, $U_\infty = 31.7m/s$.

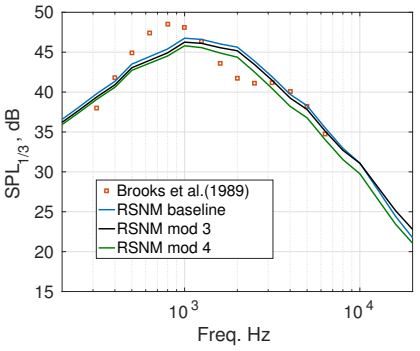

(h) Chord:22.86 cm, $U_\infty = 31.7m/s$.

Figure 6.18: Acoustic predictions (solid lines) and experimental data of Brooks et al.(1989) for a NACA 0012 airfoil at $\alpha = o$.

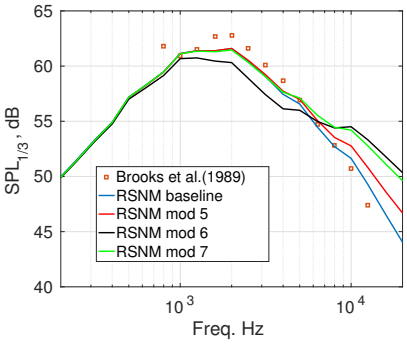

(a) Chord:30.48 cm, $U_\infty = 71.3m/s$.

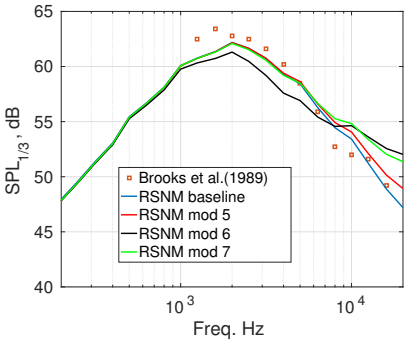

(b) Chord:22.86 cm, $U_\infty = 71.3m/s$.

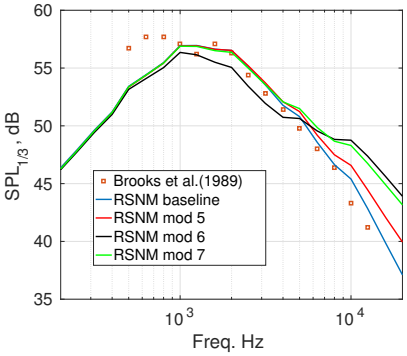

(c) Chord:30.48 cm, $U_\infty = 55.5m/s$.

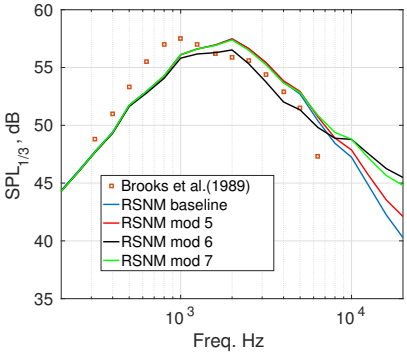

(d) Chord:22.86 cm, $U_\infty = 55.5m/s$.

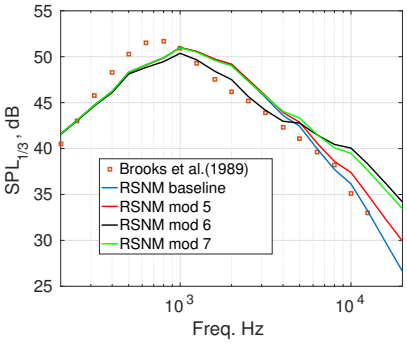

(e) Chord:30.48 cm, $U_\infty = 39.6m/s$.

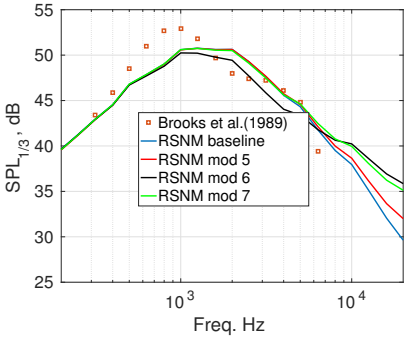

(f) Chord:22.86 cm, $U_\infty = 39.6m/s$.

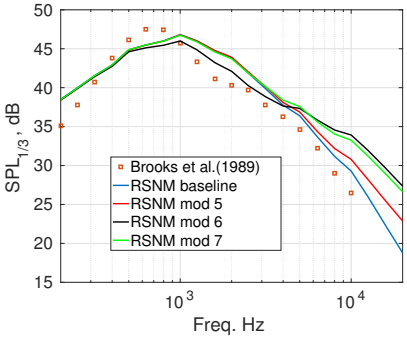

(g) Chord:30.48 cm, $U_\infty = 31.7m/s$.

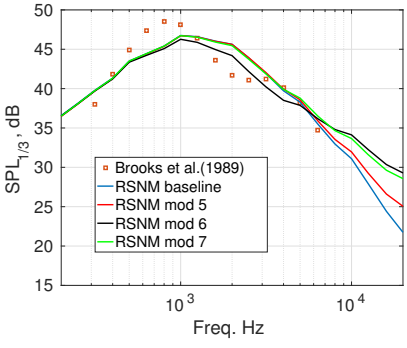

(h) Chord:22.86 cm, $U_\infty = 31.7m/s$.

Figure 6.19: Acoustic predictions (solid lines) and experimental data of Brooks et al.(1989) for a NACA 0012 airfoil at $\alpha = o$.

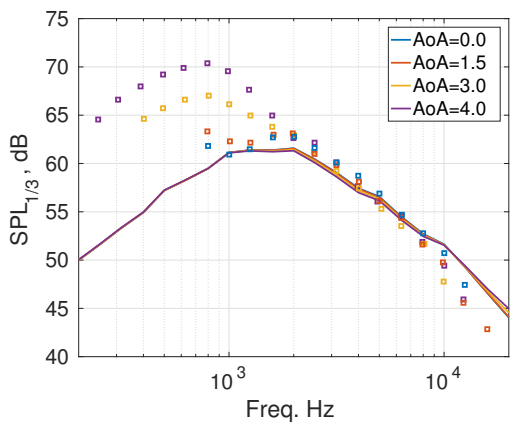

(a) Chord:30.48 cm, $U_\infty = 71.3m/s$.

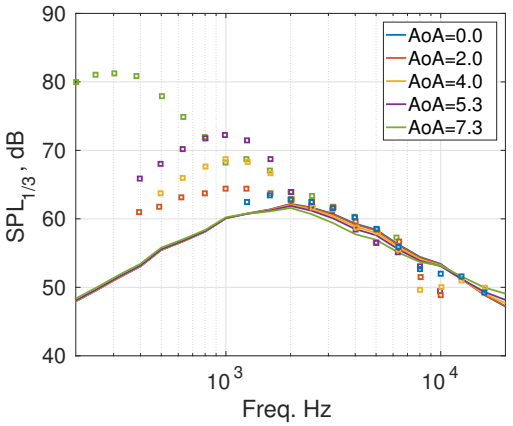

(b) Chord:22.86 cm, $U_\infty = 71.3m/s$.

Figure 6.20: Acoustic predictions for RSNM baseline (solid lines) and experimental data of Brooks et al.(1989) for a NACA 0012 airfoil at various angles of attack.

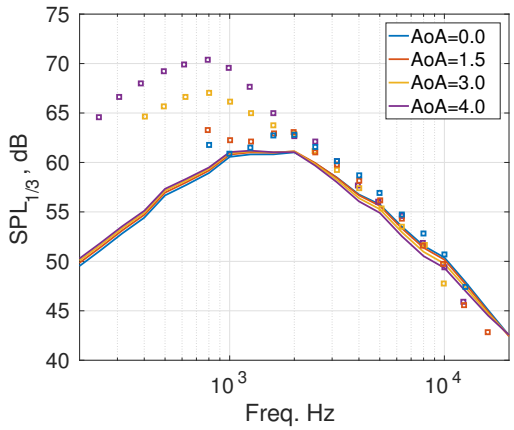

(a) Chord:30.48 cm, $U_\infty = 71.3m/s$.

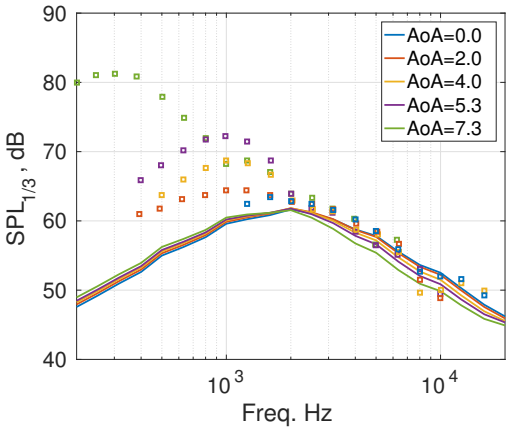

(b) Chord:22.86 cm, $U_\infty = 71.3m/s$.

Figure 6.21: Acoustic predictions for RSNM Mod 3 (solid lines) and experimental data of Brooks et al.(1989) for a NACA 0012 airfoil at various angles of attack.

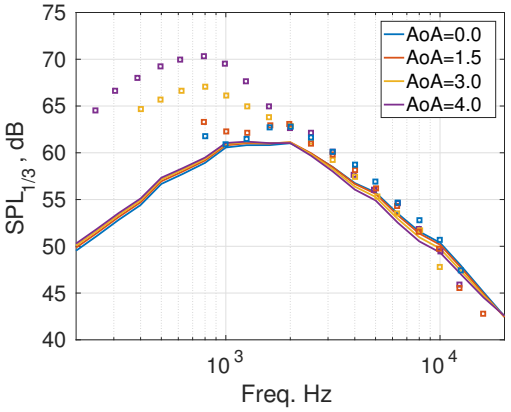

(a) Chord:30.48 cm, $U_\infty = 71.3m/s$.

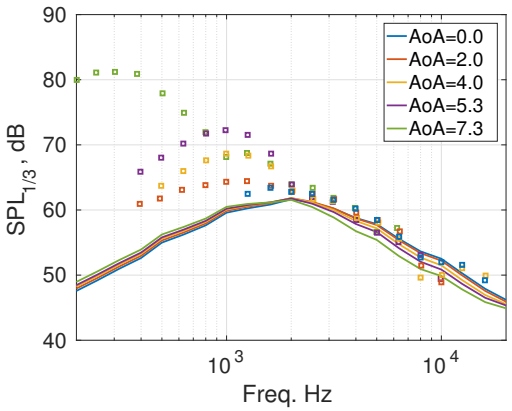

(b) Chord:22.86 cm, $U_\infty = 71.3m/s$.

Figure 6.22: Acoustic predictions for RSNM Mod. 4 (solid lines) and experimental data of Brooks et al.(1989) for a NACA 0012 airfoil at various angles of attack.

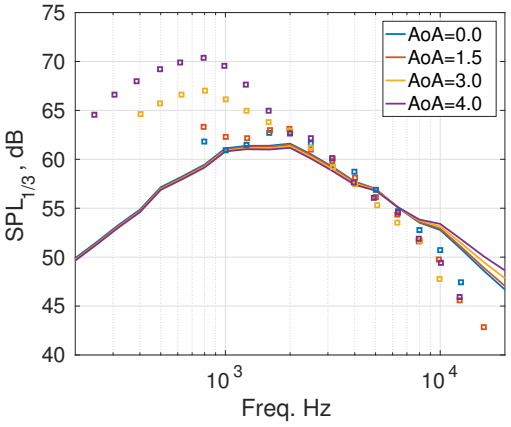

(a) Chord:30.48 cm, $U_\infty = 71.3m/s$.

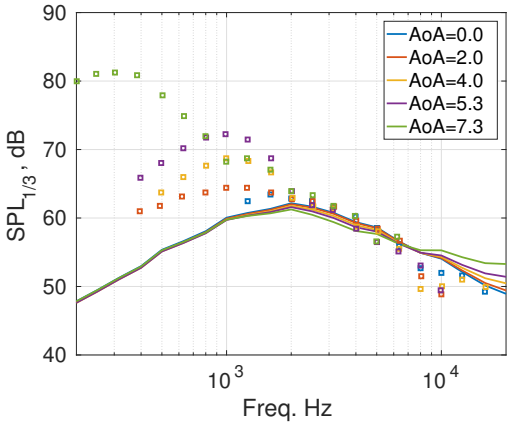

(b) Chord:22.86 cm, $U_\infty = 71.3m/s$.

Figure 6.23: Acoustic predictions for RSNM Mod. 5 (solid lines) and experimental data of Brooks et al.(1989) for a NACA 0012 airfoil at various angles of attack.

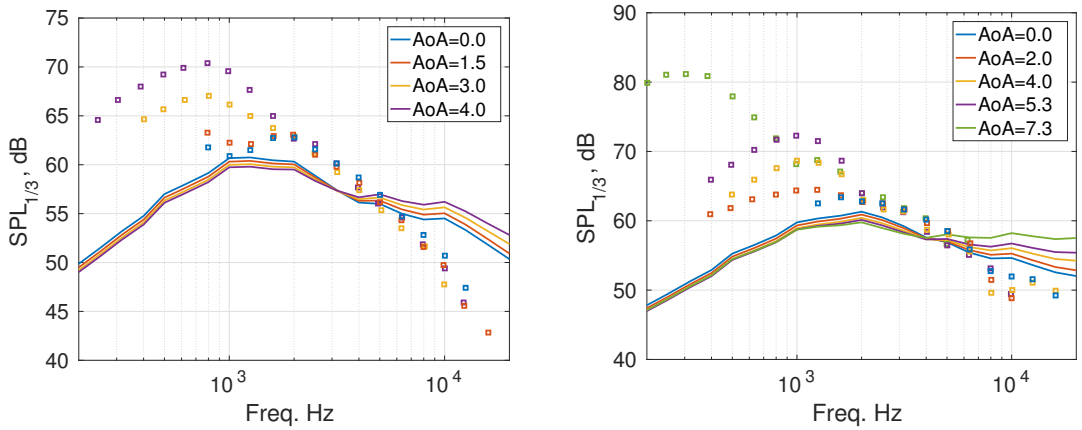

(a) Chord:30.48 cm, $U_\infty = 71.3m/s$. (b) Chord:22.86 cm, $U_\infty = 71.3m/s$.

Figure 6.24: Acoustic predictions for RSNM Mod. 6 (solid lines) and experimental data of Brooks et al.(1989) for a NACA 0012 airfoil at various angles of attack.

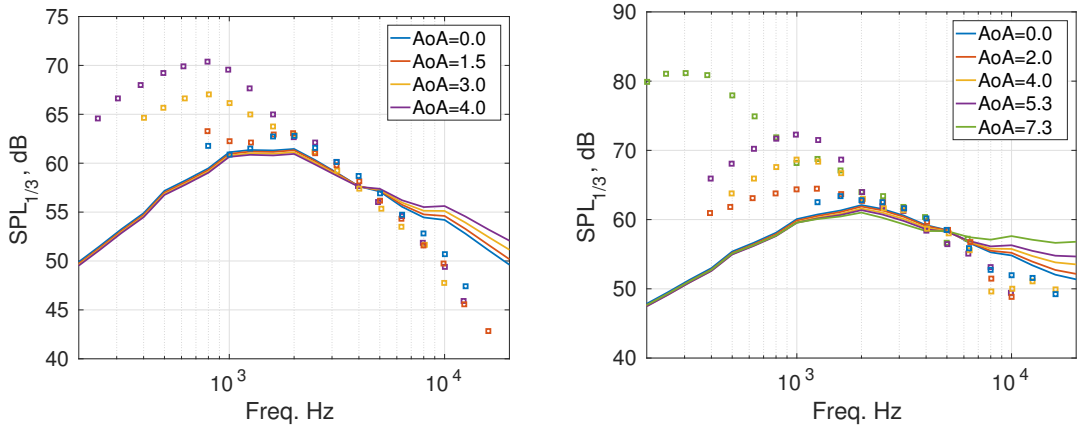

(a) Chord:30.48 cm, $U_\infty = 71.3m/s$. (b) Chord:22.86 cm, $U_\infty = 71.3m/s$.

Figure 6.25: Acoustic predictions for RSNM Mod. 7 (solid lines) and experimental data of Brooks et al.(1989) for a NACA 0012 airfoil at various angles of attack.

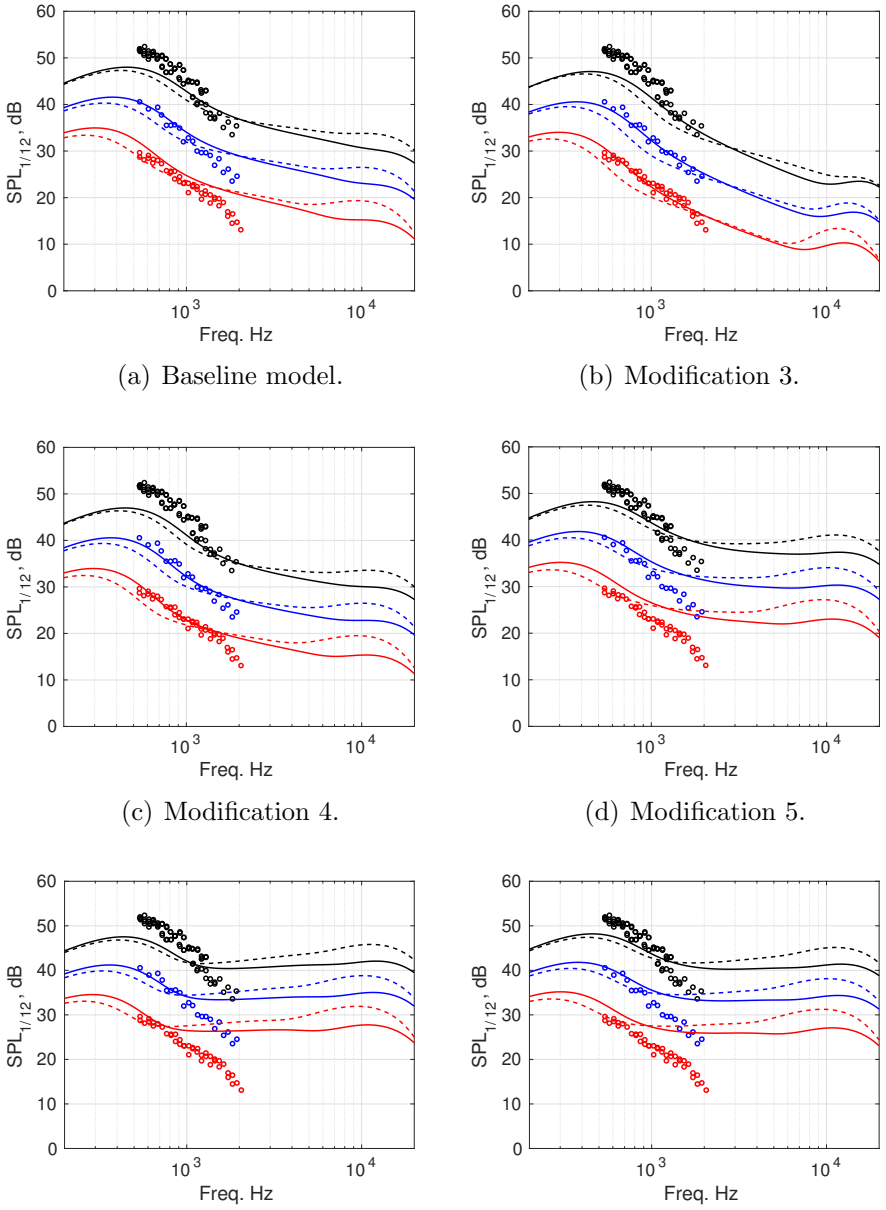

(a) Baseline model.

(b) Modification 3.

(c) Modification 4.

(d) Modification 5.

(e) Modification 6.

(f) Modification 7.

Figure 6.26: Acoustic results for a 91.40 cm chord DU-96-180 airfoil. Symbols: Experimental data of Devenport *et al.* (2010). Solid lines: RSNM at $\alpha = 3°$. Dashed lines: RSNM at $\alpha = 7°$. Red: 28 m/s. Blue: 42 m/s. Black: 58 m/s.

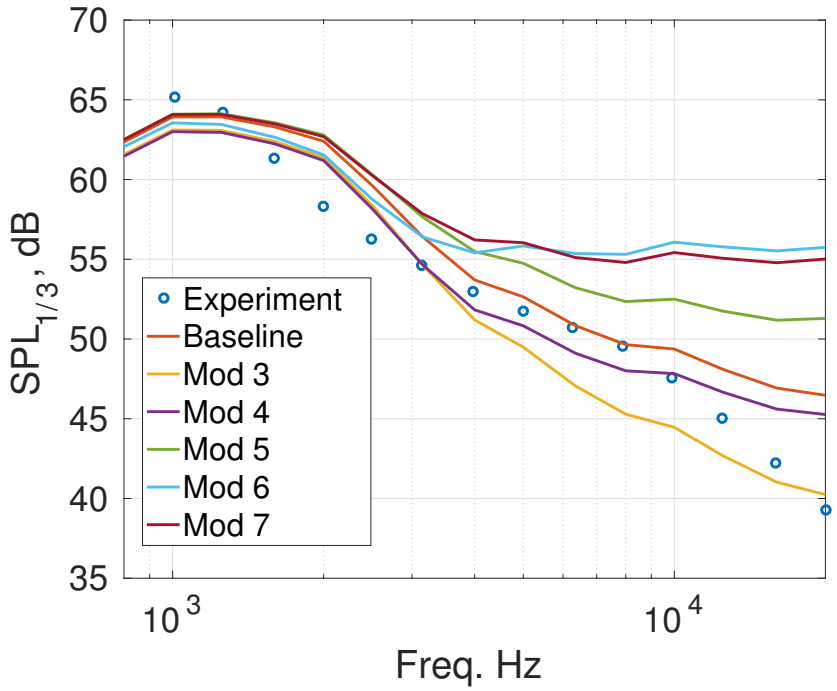

Figure 6.27: Acoustic results for a 30 cm chord DU-96-180 airfoil at $U_\infty = 40m/s$. $\alpha = 4°$. Symbols: Experimental data of Herr and Kamruzzaman (2013). Solid lines: RSNM predictions

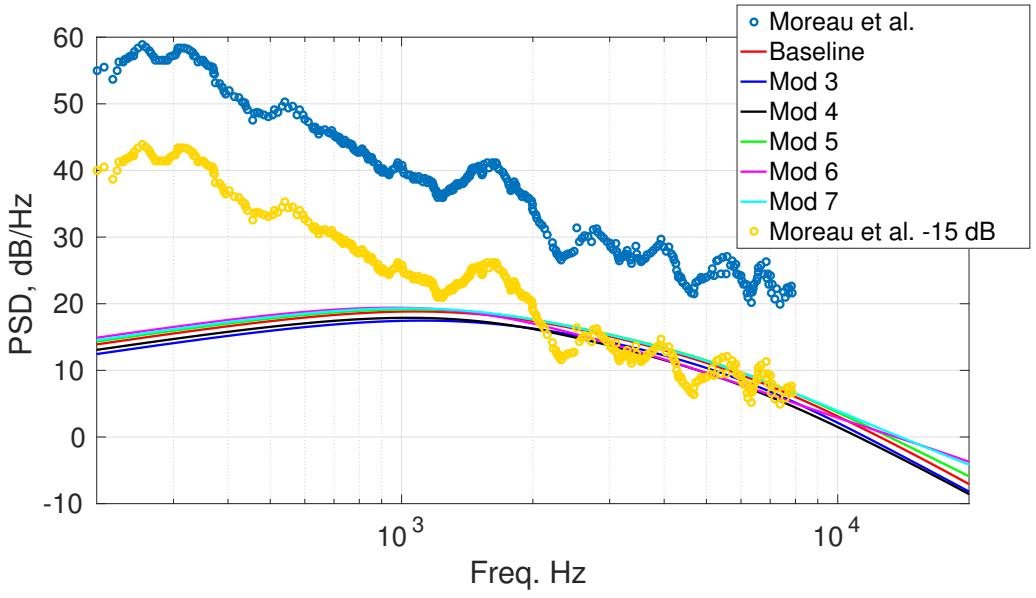

Figure 6.28: Acoustic power spectral density for the FP12 airfoil at $R_e \approx 5 \times 10^5$ at $\alpha = 0°$. Symbols: experimental data from Moreau *et al.* (2011). Solid lines: RSNM predictions.

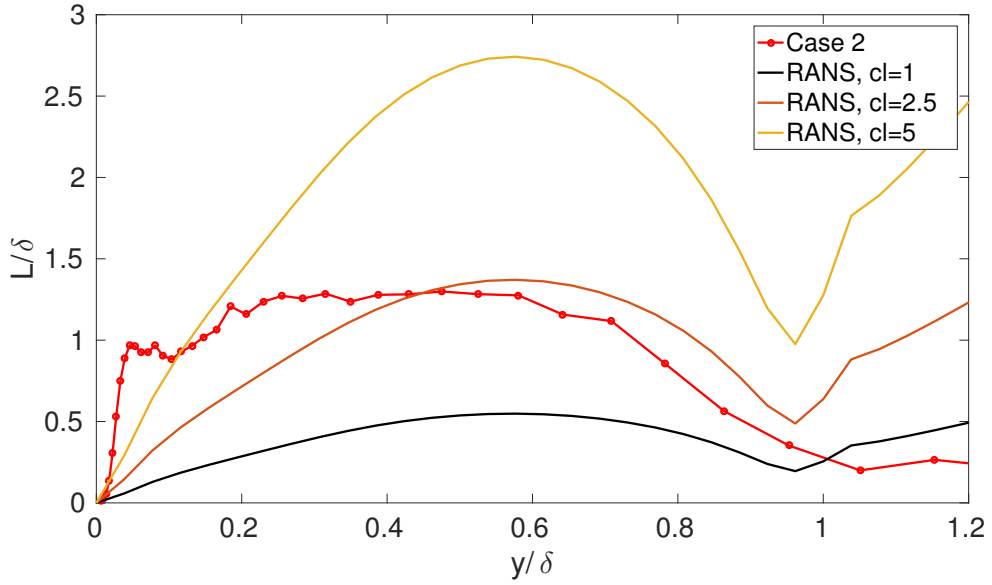

Figure 6.29: Length scale $L = c_\ell k^{3/2}/\epsilon$ for Case 1 (FP12 airfoil) at $R_e \approx 5 \times 10^5$ at $\alpha = 0°$. Symbols: experimental data, $c_\ell = 1$. Solid lines: RANS.

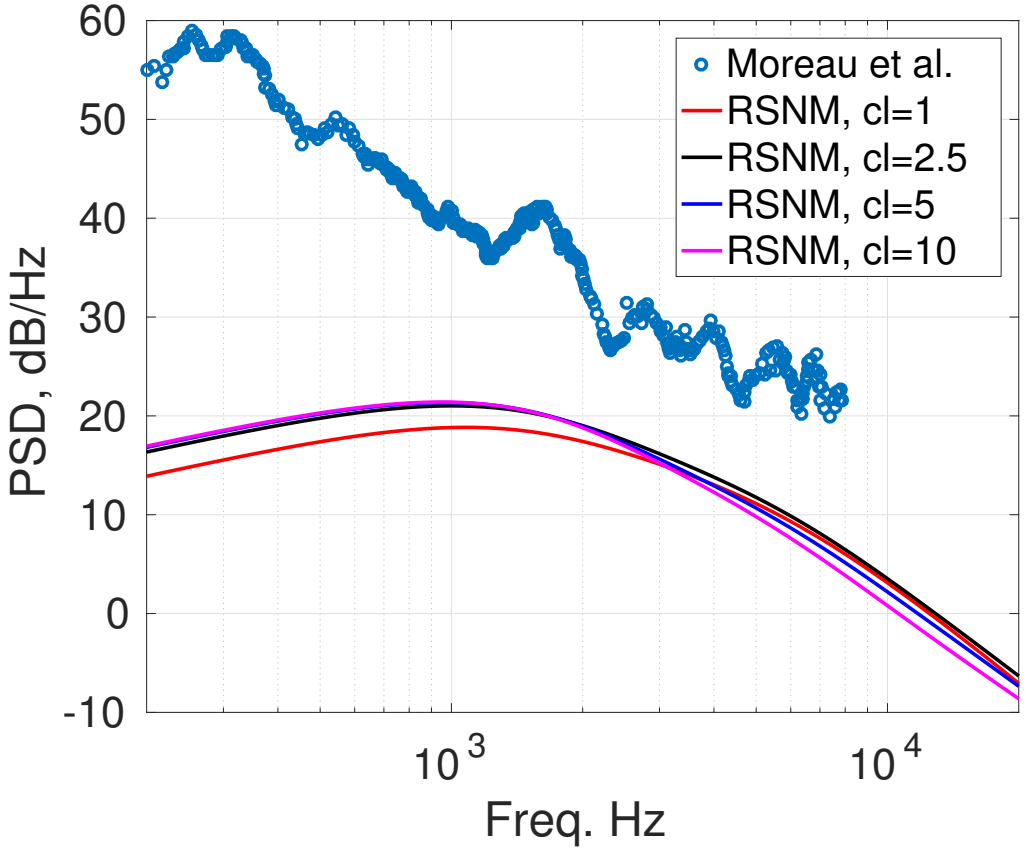

Figure 6.30: Effects of changing the length scale on the acoustic predictions of RSNM for the FP12 airfoil at $R_e \approx 5 \times 10^5$ at $\alpha = 0°$. Symbols: experimental data. Solid lines: RSNM.

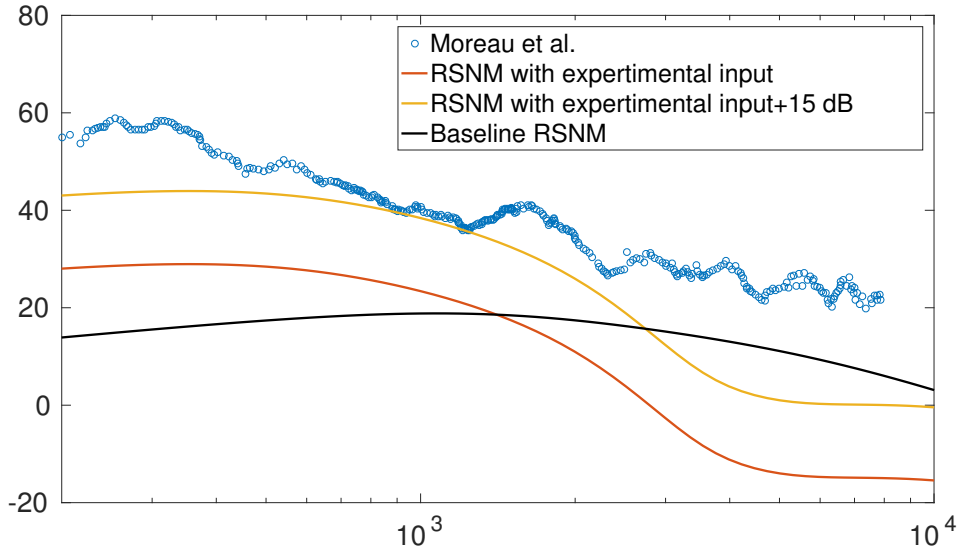

Figure 6.31: Effects of using experimental data as input to RSNM in the noise predictions for the FP12 airfoil at $R_e \approx 5 \times 10^5$ at $\alpha = 0°$. Symbols: experimental data. Solid lines: RSNM.

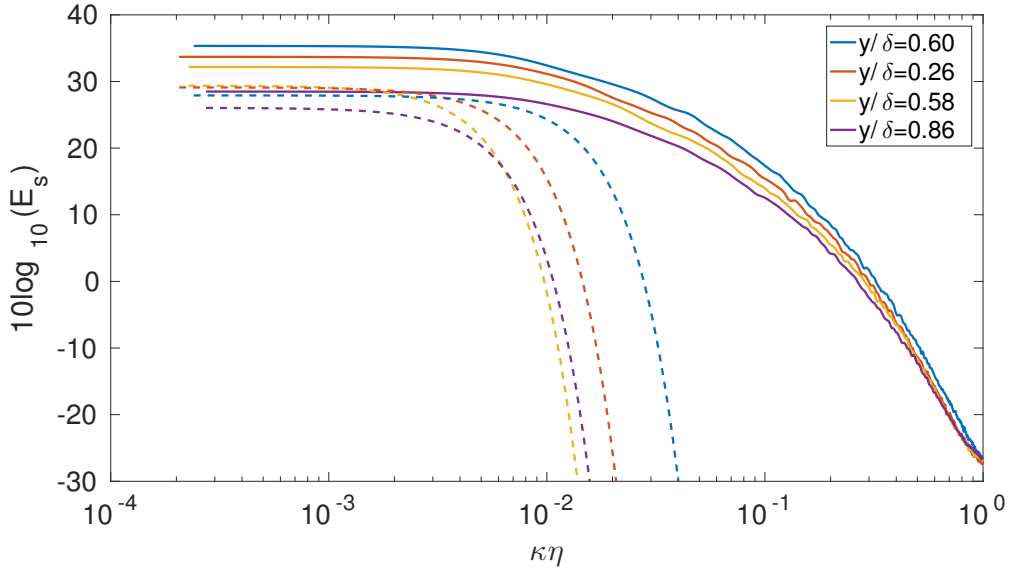

Figure 6.32: Experimental spectrum compared to baseline Gaussian model using experimental data as input at selected points in the boundary layer. The scaled spectrum $E_s = E/(\epsilon\nu^5)^{(1/4)}$. Solid lines: experimental data. Dashed lines: Gaussian spectrum+50 dB.

Chapter 7

Conclusions and future work

The general aim of this thesis was to develop a trailing edge noise prediction methodology based on mean flow data obtained from RANS CFD. The methodology, called RANS-based Statistical Noise Model (RSNM), combines the theory of Ffowcs Williams and Hall (1970) and a statistical model of the turbulent velocity cross-spectrum.

To achieve this aim, a model for the cross-spectrum of the turbulent velocity was developed by adapting a model proposed by Morris and Farassat (2002) for jet flow, and modifying it to account for the presence of the trailing edge. The model was reformulated as the product of two decaying Gaussian functions, one that depends solely on spatial separation and one that depends only on frequency. The frequency dependent part was modelled as the autospectrum of the turbulent velocity, and the dependency on spatial separation was modelled as the coherence function at zero frequency. The autospectrum model contained two empirical parameters, an amplitude parameter and a length-scale parameter, which were determined by best fit to the experimental data. This formulation was defined as the baseline model.

Seven alternative models were formulated by modifying either the spatial coherence model, or the autospectrum model. They were labelled as Modifications 1 to 7 (see Table 6.14).

Two modifications to the autospectrum model were investigated. The first modification replaced the global empirical parameters in the Gaussian model by local parameters calculated at each point in the sampling domain. This was done by an optimization routine in Matlab that followed the following steps: 1) The parameters were set to their empirical values and the spectrum was integrated to obtain the turbulent kinetic energy k. 2) A cost function was defined by the error between k

obtained from integrating the spectrum and k obtained from RANS-CFD. 3) The cost function was minimized by an iterative process.

The second modification consisted in replacing the Gaussian model by the model spectrum of Pope (2000). This model also contained empirical parameters, which were obtained with the same method described for Modification 1.

Two models for the spatial coherence were investigated, namely the Simplified Anisotropic Model (SAM) of Gavin (2002), and a new empirical anisotropic model, which was developed as part of this research.

The SAM models the coherence as an ellipsoid, which is inclined with respect to the wall. The ellipsoid is then mapped onto a sphere and the coordinate system is rotated on to the major/minor axes of the ellipsoid by means of a transformation matrix. The model is closed by using isotropic turbulence theory and a set of empirical parameters, including a global length scale based on the boundary layer thickness. The combination of the SAM coherence model with the baseline autospectrum model was labelled Modification 3. The SAM model was also modified by replacing the global length-scale by a local length-scale based on the turbulent kinetic energy and dissipation at each point in the sampling domain. The combination of the modified SAM coherence model with the baseline autospectrum model was labelled Modification 4.

The new empirical anisotropic model was based on the experimental investigation of the flow in the vicinity of the trailing edge of sharp-edged struts. It models the coherence function as the product of two decaying exponential functions (streamwise and wall-normal directions) and a Gaussian function (spanwise direction). The decay rate in each direction is controlled by a length-scale based on the turbulent kinetic energy the turbulence dissipation, and an empirical parameter, which is different in each direction. The empirical parameters were found by best fit to the experimental data. Three sets of parameters were found, one for each of the experimental cases investigated in this thesis. Modifications 5, 6 and 7 used the empirical parameters determined for Cases 2, 1 and 3, respectively.

To validate the RSNM methodology, the noise predictions obtained from the baseline model, as well as those obtained from the seven alternative models, were compared with experimental data from the literature for three different airfoils, a NACA 0012, a DU-96-180 and the FP12, at a range of operating conditions. The main conclusions of this study are as follows:

1. The baseline model was able to match the experimental data very well for the

NACA 0012 cases at zero angle of attack. At non zero angle of attack, the baseline model predicts the correct levels and spectral shape for frequencies over 2 kHz; however, it does not capture the large peaks present in the experimental data below 1 kHz for angles of attack of three degrees or more. It is argued that these peaks are caused by noise mechanisms other than broadband trailing edge noise, such as vortex shedding or separation. These mechanisms were not included in the formulation of the model used in this thesis. The baseline model also predicted the correct levels and spectral shape for the DU-96-180 cases, which included angles of attack of 3, 4 and 7 degrees.

2. The baseline model is not very sensitive to changes in angle of attack, showing differences only for $f \geq 2$ kHz with a spread of less than 3 dB for the NACA 0012 airfoil, which is consistent with the experimental data of Brooks *et al.* (1989). The effect of angle of attack is more visible in the DU-96-180 results, as the results are displayed in 12th octave bands. Here the model predicts a decrease in amplitude with angle of attack for $f \leq 2$ kHz, but the difference is less than 3 dB, which is consistent with the spread in the experimental data of Devenport *et al.* (2010). For $f \geq 2$ kHz, the model predicts a slight increase in amplitude with increased angle of attack, with the largest difference (4 dB) occurring close to 10 kHz. There were no experimental data available over 2 kHz to assess the accuracy of this prediction.

3. Modifications 1 and 2 resulted in large overpredictions (up to 20 dB) of the noise levels and an upward shift in the frequency of the peak (up to 3 kHz shift). It is argued that these effects are caused by the optimization routine being unable to find the correct values of the empirical coefficients, possibly due to finding a local minimum of the error function.

4. Modifications 3 and 4 follow the same trends as the baseline model, but predict slightly lower noise levels. The differences are less than 2 dB For the NACA 0012 airfoil. This is the case for both zero and non-zero angles of attack. For the DU-96-180, Mod 4 follows the same shape as the baseline model, but approximately 2 dB below. Modification 3 shows the same behaviour for $f \leq 1$ kHz, but predicts a steeper decay with frequency above 1 kHz, which agrees with the data of Devenport *et al.* (2010).

5. Modifications 5, 6 and 7 follow the same trends as the baseline model for the NACA 0012 cases for frequencies below 5 kHz, but begin to depart from both the baseline model and the experimental data for higher frequencies. This is particularly severe for the higher angle of attack cases, where Modifications 6

and 7 result in overpredictions of the noise levels and a flatter spectral shape. For the DU-96 180 cases, Modifications 5, 6 and 7 begin to depart from the baseline model and the experimental data as early as $f = 1$ kHz, predicting a plateau in the spectral shape. This plateau is not present in the data of Herr and Kamruzzaman (2013). The data of Devenport *et al.* (2010) do not go above 2 kHz; however, the trends displayed by the experimental spectra do not suggest the existence of a plateau, but a sharp decay in levels with increased frequency. The predicted plateau could be a consequence of neglecting the frequency dependency of the coherence function in the modelling process.

6. When applied to the FP12 airfoil, all the models tested produced the correct slope for frequencies above 2 kHz; however, they did not produce the correct absolute levels, requiring an offset of 15 dB to match the experimental data. The underprediction of noise levels was attributed to the underprediction of turbulent kinetic energy, an overprediction of dissipation by the RANS CFD, an underprediction of the turbulent length scales, and most importantly, the large difference between the turbulence autospectrum model and the experimental autospectrum.

In summary, the main contribution of this thesis is a validated RANS-based Statistical Noise Model (RSNM), which was capable of accurately and efficiently predicting the spectral shape and levels of a NACA 0012 airfoil and a DU-96-180 airfoil at a range of operating conditions.

The baseline model produced more accurate predictions than all the modifications tested, followed closely by Modifications 3 and 4, which used the SAM model for the coherence function and produced nearly equivalent results to the baseline model, except for a small offset of less than -2 dB. Other modifications to the model were detrimental to the model's performance, particularly the modifications to the autospectrum model (Modifications 1 and 2).

The development of a new empirical cross-spectrum model for the turbulent velocity in the vicinity of the trailing edge is also an important contribution of this thesis. The formulation of RSNM makes the modification of the cross-spectrum model or the incorporation of new models for the cross-spectrum relatively easy. Modifications to the cross-spectrum model could be made by changing either the autospectrum model, or by changing the model of the spatial coherence, for example by incorporating the frequency dependence of the coherence function, which was neglected in the present model.

7.1 Future work

As future work, the first step would be to apply RSNM to a range of different airfoils to further validate the method and increase confidence in its noise predicting capabilities. As a first test, the model could be applied to the S831 airfoil, developed by the National Renewable Energy Laboratory (NREL). Both flow and noise data are presented in Devenport *et al.* (2010) and the airfoil coordinates are available in the NREL website.

Later, RSNM could be extended to three dimensional cases, such as wings with a sweep angle or with sinusoidal trailing edges, by modifying the Green's function, or simply by dividing the airfoil into spanwise strips, applying the model to each one of them and then adding the contributions as incoherent sources. This approach would need to be validated.

The major difficulty in the RSNM approach is to provide an accurate cross-spectrum model. Having access to DNS or LES data would have been of great help in developing a model for the cross-spectrum. A possible way forward would be to run a DNS calculation of one of the NACA 0012 cases and extract cross-correlation data from the source region to develop and validate a RANS-based cross-spectrum model

Alternatively, one could obtain the cross-spectrum directly from an LES solution. The LES solution would provide the correlation function, which can then be used to obtain the cross-spectrum by means of a Fourier transform. These cross-spectrum data can then be used directly in the RSNM method to compute the noise in the frequency domain.

As the noise sources are located in the boundary layer, only a small region around the airfoil would need to be simulated using LES, and a RANS solution over the entire domain can be used as a boundary condition to the LES simulation. This would reduce the computational effort required to obtain the noise sources.

The assumptions made regarding the spanwise extent of the cells and their relation to the spanwise coherence length require further investigation. Neglecting the frequency dependency of the spanwise coherence length can be a significant source of error. An alternative worth exploring would be to use a frequency dependent coherence length, as described in Appendix B. The spanwise length of the cell should be set to $L_s = \delta/100$, to be consistent with the cell dimensions chosen in x and y directions. These assumptions would provide a frequency dependent correction factor that would more accurately model the flow physics and hopefully improve the

performance of RSNM.

Similarly, incorporating the frequency dependence of the spatial coherence function in both the streamwise ad wall-normal directions, which was neglected in the present model, could improve the performance of RSNM, albeit at the cost of more modelling complexity.

Finally, there is a large spread in the experimental data available for TE noise, particularly for moderately high Re_c. This makes it very difficult to validate a noise model. Also, more data at higher Re_c are needed. These data should include simultaneous flow and noise measurements, preferably using non-intrusive flow measurement techniques such as PIV, and acoustic measurements using beamforming to better identify the noise sources and to quantify the contribution of TE noise more accurately.

Ideally, a variety of airfoil shapes should be tested at various angles of attack and Reynolds numbers. This is an enormous undertaking, and requires a large wind tunnel with a dedicated aeroacoustic test section and costly instrumentation.

References

Amiet, R. K. 1975. Acoustic radiation from an airfoil in a turbulent stream. *Journal of Sound and Vibration* 41(4), pp. 407–420.

Amiet, R. K. 1976. Noise due to turbulent flow past a trailing edge. *Journal of Sound and Vibration* 47(3), pp. 387–393.

Arguelles, P., Bischo, M., Busquin, P., Droste, R., Evans, Kroll, W., Lagardere, J., Lina, A., Lumsden, J. and Ranque, D. 2001. European aeronautics: A vision for 2020. Tech. rep., The European Commission, Luxembourg.

Batchelor, G. K. 1953. *The theory of homogeneous turbulence.* Cambridge University Press.

Bauer, M. and Zeibig, A. 2006. Towards the applicability of the modified von karman spectrum to predict trailing edge noise. *Notes on Numerical Fluid Mechanics and Multidisciplinary Design (NNFM)* 92, pp. 381–388.

Bendat, J. S. and Piersol, A. G. 2011. *Random data: analysis and measurement procedures.* John Wiley & Sons, New York, 4 ed.

Bridges, J. and Podboy, G. G. 1999. Measurements of two-point velocity correlations in a round jet with application to jet noise. *5th AIAA/CEAS Aeroacoustics Conference* AIAA-99-1966.

Brooks, L. A. and Hodgson, T. H. 1981. Trailing edge noise prediction from measured surface pressures. *Journal of Sound and Vibration* 78, pp. 69–117.

Brooks, T., Pope, D. and Marcolini, M. 1989. Airfoil self-noise and prediction. Reference Publication 1218, NASA.

Bruun, H. 1995. Hot-wire anemometry-principles and signal analysis .

Casalino, D. and Barbarino, M. 2011. Stochastic method for airfoil self-noise computation in frequency domain. *AAIA Journal* 49(11).

Catlett, M. R., Forest, J. B., Anderson, J. M. and Stewart, D. O. 2014. Empirical spectral model of surface pressure fluctuations beneath adverse pressure gradients. In: *20th AIAA/CEAS Aeroacoustics Conference, AIAA AVIATION Forum, Atlanta, GA*. vol. (AIAA 2014-2910).

Chandiramani, K. L. 1974. Diffraction of evanescent waves, with applications to aerodynamically scattered sound and radiation from unbaffled plates. *The Journal of the Acoustical Society of America* 55, pp. 19–29.

Chase, D. M. 1972. Sound radiated by turbulent flow off a rigid half-plane as obtained from a wavevector spectrum of hydrodynamic pressure. *J . of the Acoustical Society of America* .

Chin, C., Hutchins, N., Ooi, A. and Marusic, I. 2011. Spatial resolution correction for hot-wire anemometry in wall turbulence. *Exp Fluids* 50, p. 14431453.

Christophe, J., Anthoine, J. and Moreau, S. 2009. Trailing edge noise of a controlled-diffusion airfoil at moderate and high angle of attack. In: *Fifteenth AIAA/CEAS Aeroacoustics Conference*.

Cipolla, K. and Keith, W. 2000. Effects of pressure gradients on turbulent boundary layer wave number frequency spectra. *AIAA journal* 38(10), pp. 1832–1836.

Clauser, F. 1954. Turbulent boundary layers in adverse pressure gradients. *Journal of the Aeronautical Sciences* 21(2), pp. 91–108.

Coles, D. 1962. The turbulent boundary layer in a compressible fluid. *Rand Report R-403-PR* .

Curle, N. 1955. The influence of solid boundaries upon aerodynamic sound. *Proceedings of the Royal Society of London. Series A, Mathematical and Physical Sciences* 231(1187), pp. 505–514.

Devenport, W., Burdisso, R., Camargo, H., Crede, E., Remilleux, M., Rasnik, M. and Van Seeters, P. 2010. Aeroacoustic testing of wind turbine airfoils. Tech. rep., National renewable energy laboratories, Virginia Polytechnic Institute and State University Blacksburg, Virginia.

Devenport, W. J., Muthanna, C., Ma, R. and L. Glegg, S. A. 2001. Two-point descriptions of wake turbulence with application to noise prediction. *AIAA journal* 39(12), pp. 2302–2307.

Dieste, M. and Gabard, G. 2009. Synthetic turbulence applied to broadband in-

teraction noise. In: *15th AIAA/CEAS Aeroacoustics Conference (30th AIAA Aeroacoustics Conference)*.

Dobrzynski, W., Ewert, R., Pott-Pollenske, M., Herr, M. and Delfs, J. 2009. Research at dlr towards airframe noise prediction and reduction. *Aerospace Science and Technology* 12, pp. 80–90.

Ewert, R. 2008. Broadband slat noise prediction based on caa and stochastic sound sources from a fast random particle-mesh (rpm) method. *Computers and Fluids* 37, pp. 369–387.

Ewert, R., Appel, C., Dierke, J. and Herr, M. 2009. Rans/caa based prediction of naca 0012 broadband trailing edge noise and experimental validation. In: *15th AIAA/CEAS Aeroacoustics Conference , Miami, Florida*.

Favre, A. J., Gaviglio, J. J. and Dumas, R. 1957. Space–time double correlations and spectra in a turbulent boundary layer. *Journal of Fluid Mechanics* 2, pp. 313–342.

Ffowcs Williams, J. and Hall, L. 1970. Aerodynamic sound generation by turbulent flow in the vicinity of a scattering half plane. *Journal of Fluid Mechanics* 40(1151), pp. 657–670.

Ffowcs Williams, J. E. and Hawkings, D. L. 1969. Sound generation by turbulence and surfaces in arbitrary motion. *Proceedings of the Royal society of London. Series A,Mathematical and Physical Sciences* 264(1151), pp. 321–342.

Fischer, A., Madsen, H. A. and Bertagnolio, F. 2015. Experimental investigation of the surface pressure field for prediction of trailing edge noise of wind turbine aero foils. *International Journal of Aeroacoustics* 14(5-6), pp. 767–809.

Ganapathisubramani, B., Hutchins, N., Hambleton, W. T., Longmire, E. K. and Marusic, I. 2005. Investigation of large-scale coherence in a turbulent boundary layer using two-point correlations. *Journal of Fluid Mechanics* 524, pp. 57–80.

Gavin, J. 2002. *Unsteady forces and sound caused by boundary layer turbulence entering a turbomachinery rotor*. Ph.D. thesis, The Pennsylvania State University, University Park, PA.

Gessner, F. and Moller, G. 1971. Response behaviour of hot wires in shear flow. *Journal of Fluid Mechanics* 47(03), pp. 449–468.

Glegg, S., Morin, B., Atassi, O. and Reba, R. 2008. Using rans calculations of

turbulent kinetic energy to provide predictions of trailing edge noise. In: *14th AIAA/CEAS Aeroacoustics Conference (29th AIAA Aeroacoustics Conference).*

Gloerfelt, X. and LeGarrec, T. 2009. Trailing edge noise from an isolated airfoil at a high reynolds number. *15th AIAA/CEAS Aeroacoustics Conference, Miami, Florida* .

Goldstein, M. and Rosenbaum, B. 1973. Effect of anisotropic turbulence on aerodynamic noise. *J. Acoust. Soc. Am.* 54(3), pp. 630–645.

Goody, M. 2004. Empirical spectral model of surface pressure fluctuations. *AIAA journal* 42(9), pp. 1788–1794.

Harun, Z. 2012. *The structure of adverse and favourable pressure gradient turbulent boundary layers*. Ph.D. thesis, Department of Mechanical Engineering, University of Melbourne.

Herr, M. and Kamruzzaman, M. 2013. Benchmarking of trailing-edge noise computations: outcome of the banc-ii workshop. In: *19th AIAA/CEAS Aeroacoustics Conference*.

Howe, M. S. 1978. A review of the theory of trailing edge noise. *Journal of sound and vibration* 61(3), pp. 437–465.

Jones, L. E. and Sandberg, R. D. 2009. Direct numerical simulations of noise generated by the flow over an airfoil with trailing edge serrations. *15th AIAA/CEAS Aeroacoustics Conference (30th AIAA Aeroacoustics Conference), Miami, Florida* .

Kallas, S., Geoghegan-Quinn, M., Darecki, M., Edelstenne, C., Enders, T., Fernandez, E. and Hartman, P. 2011. Flightpath 2050 europes vision for aviation. *Report of the High Level Group on Aviation Research, European Commission, Brussels, Belgium, Report No. EUR* 98.

Kamruzzaman, M., Lutz, T., A., H. and Kramer, E. 2008. Rans based prediction of airfoil trailing edge far-field noise: Impact of isotropic and anisotropic turbulence. In: *14th AIAA/CEAS Aeroacoustics Conference (29th AIAA Aeroacoustics Conference,)*.

Kamruzzaman, M., Lutz, T., Herrig, A. and Kramer, E. 2007. An approach to rans based prediction of airfoil trailing edge far-field noise. In: *Second International Meeting on Wind Turbine Noise, Lyon, France, September*.

Kamruzzaman, M., Lutz, T., Herrig, A. and Krämer, E. 2012. Semi-empirical mod-

eling of turbulent anisotropy for airfoil self-noise predictions. *AIAA journal* 50(1), pp. 46–60.

Karweit, M., Belanc-benon, P., Juve, D. and Comte-Billot, G. 1991. Simulation of the propagation of an acoustic wave trhough a turbulent velocity field: A study of phase variance. *Journal of Acoustic Society of America* 89(1), pp. 52–62.

Kato, C., Iida, A., Takano, Y., Fujita, H. and Ikegawa, M. 1993. Numerical prediction of aerodynamic noise radiated from low mach number turbulent wake. *AIAA paper* (93-0145).

Kerherv, F., Fitzpatrick, J. and Kennedy, J. 2010. Determination of two-dimensional spacetime correlations in jet flows using simultaneous piv and ldv measurements. *Experimental Thermal and Fluid Science* 34, pp. 788–797.

Khalighi, Y., Mani, A., Ham, F. and Moin, P. 2010. Prediction of sound generated by complex flows at low mach numbers. *AIAA JOURNAL* 48(2).

Khan, M., MacKenzie, K. and Bruun, H. 1987. The effects of blockage correction in hot-wire probe calibration facilities. *Journal of Physics E: Scientific Instruments* 20(8), p. 1031.

Khavaran, A. 1999. Role of anisotropy in turbulent mixing noise. *AIAA Journal* 37(7), pp. 832–841.

Kim, J., Moin, P. and Moser, R. 1987. Turbulence statistics in fully developed channel flow at low Reynolds number. *Journal of Fluid Mechanics* 177(1), pp. 133–166.

Klebanoff, P. 1954. Characteristics of turbulence in a boundary layer with zero pressure gradient. naca report 1247, nasa–langley research center, hampton, va, 1955. Tech. rep., See also NACA Technical Note 3178.

Launder, B., Reece, G. J. and Rodi, W. 1975. Progress in the development of a reynolds-stress turbulence closure. *Journal of fluid mechanics* 68(03), pp. 537–566.

Lee, Y., Blake, W. K. and Farabee, T. M. 2005. Modeling of wall pressure fluctuations based on time mean flow field. *Journal of Fluids Engineering* 127(2), pp. 233–241.

Lighthill, M. J. 1952. On sound generated aerodynamically. *Mathematical and Physical Sciences* 211(1107), pp. 564–587.

Ligrani, P. and Bradshaw, P. 1987. Spatial resolution and measurement of turbulence in the viscous sublayer using subminiature hot-wire probes. *Experiments in Fluids* 5(6), pp. 407–417.

Lindgren, B. and Johansson, A. V. 2004. Universality of probability density distributions in the overlap region in high reynolds number turbulent boundary layers. *Physics of Fluids* 16.

Lockard, D. P. and Lilley, G. M. 2004. The airframe noise reduction challenge. Tech. Rep. NASA/TM2004213013, NASA.

Macdonald, H. M. 1915. A class of diffraction problems. *Proc. Lond. Math. Sic.* 14(2), pp. 410–427.

Marsden, A. L., Wang, M., Dennis Jr, J. E. and Moin, P. 2007. Trailing-edge noise reduction using derivative-free optimization and large-eddy simulation. *J. Fluid Mech.* 572, pp. 13–36.

Marsden, O., Bogey, C. and Bailly, C. 2008. Direct noise computation of the turbulent flow around a zero-incidence airfoil. *AIAA JOURNAL* 46(4).

Menter, F., Kuntz, M. and Langtry, R. 2003. Ten years of industrial experience with the sst turbulence model. *Turbulence, heat and mass transfer* 4, pp. 625–632.

Menter, F. R. 1992a. Improved two-equation $k - \omega$ turbulence models for aerodynamic flows, nasa ames, ca. *NASA Technical Memorandum TM-103975* .

Menter, F. R. 1992b. Performance of popular turbulence model for attached and separated adverse pressure gradient flows. *AIAA journal* 30(8), pp. 2066–2072.

Mesbah, M. 2006. Flow noise prediction using the stochastic noise generation and radiation approach. *Ph.D Thesis, Katholieke Universiteit Leuven, Belgium* .

Migliore, P. and Oerlemans, S. 2004. Wind tunnel aeroacoustic tests of six airfoils for use on small wind turbines. *AIAA Wind Energy Symposium, Reno, Nevada, January 58* .

Moreau, D., Brooks, L. and Doolan, C. 2011. Broadband noise from sharp-edged struts. *J. Acoust. Soc. Am.* 129(5), pp. 2820–2829.

Moreau, S. and Roger, M. 2009. Back-scattering correction and further extensions of amiet's trailing-edge noise model. part ii: Application. *Journal of Sound and Vibration* 323(1-2), pp. 397–425.

Morris, P. and Zaman, K. 2010. Velocity measurements in jets with application to noise source modeling. *Journal of Sound and Vibration* 329, pp. 394–414.

Morris, P. J. and Farassat, F. 2002. Acoustic analogy and alternative theories for jet noise prediction. *AIAA Journal* 40(4), pp. 671–680.

Oerlemans, S., Maeder, T. and Kgler, K. 2008. Reduction of wind turbine noise using optimized airfoils and trailing-edge serrations. *14th AIAA/CEAS Aeroacoustics Conference (29th AIAA Aeroacoustics Conference), Vancouver, British Columbia Canada, 5 - 7 May 2008* .

Osterlund, J. M. 1999. Experimental studies of zero pressure-gradient turbulent boundary-layer flow. *Ph.D. Thesis, Royal Institute of Technology, Stockholm, Sweden* .

Peltier, L. and Hambric, S. 2007. Estimating turbulent-boundary-layer wall-pressure spectra from cfd rans solutions. *Journal of Fluids and Structures* 23, pp. 920–937.

Phillips, W. R. C. 2000. Eulerian spacetime correlations in turbulent shear flows. *Physics of Fluids* 12(8), pp. 98–108.

Pope, S. B. 2000. *Turbulent flows.* Cambridge university press.

Pröbsting, S., Tuinstra, M. and Scarano, F. 2015. Trailing edge noise estimation by tomographic particle image velocimetry. *Journal of Sound and Vibration* 346, pp. 117–138.

Purtell, L. P., Klebanoff, P. and Buckley, F. 1981. Turbulent boundary layer at low reynolds number. *Physics of Fluids* 24, p. 802.

Quadrio, M. and Luchini, P. 2003. Integral spacetime scales in turbulent wall flows. *Physics of Fluids* 15(8), pp. 2219–2227.

Ribner, H. S. 1969. Quadrupole correlations governing the pattern of jet noise. *Journal of Fluid Mechanics,* 38, pp. 1–24.

Roache, P. J. 1998. *Verification and validation in computational science and engineering.* Albuquerque, NM.: Hermosa Publications.

Roger, M. and Moreau, S. 2005. Back-scattering correction and further extensions of amiet's trailing-edge noise model. part 1: theory. *Journal of Sound and Vibration* 286(3), pp. 477–506.

Saddoughi, S. G. and Veeravalli, S. V. 1994. Local isotropy in turbulent boundary layers at high reynolds number. *Journal of Fluid Mechanics* 268, pp. 333–372.

Sandberg, R. D., Jones, L. E. and Sandham, N. D. 2008. Direct numerical simulations of noise generated by turbulent flow over airfoils. In: *14th AIAA/CEAS Aeroacoustics Conference, Vancouver, British Columbia, Canada*.

Sandberg, R. D., Jones, L. E. and Sandham, N. D. 2009. Investigation and prediction of transitional airfoil self-noise. *15th AIAA/CEAS Aeroacoustics Conference (30th AIAA Aeroacoustics Conference), Miami, Florida,11-13 May* .

Schlinker, R. and Amiet, R. 1981. Helicopter rotor trailing edge noise. *Contractor Report CR-3470, NASA* .

Seo, J. H. and Moon, Y. J. 2007. Aerodynamic noise prediction for long-span bodies. *Journal of Sound and Vibration* 306(3), pp. 564–579.

Singer, B. A., Brentner, K. S., Lockard, D. P. and Lilley, G. M. 2000. Simulation of acoustic scattering from a trailing edge. *Journal of Sound and Vibration* 3(3), pp. 541–560.

Smirnov, A., Shi, S. and Celik, I. 2001. Random flow generation technique for large eddy simulations and particle-dynamics modeling. *Journal of Fluids Engineering* 123, pp. 359–371.

Smol'Yakov, A. and Tkachenko, V. 1991. Model of a field of pseudosonic turbulent wall pressures and experimental data. *Soviet physics. Acoustics* 37(6), pp. 627–631.

Spalart, P. R. 1988. Direct simulation of a turbulent boundary layer up to rj= 1410. *Journal of Fluid Mechanics* 187(1), pp. 61–98.

Tam, C. K. W. and Auriault, L. 1999. Jet mixing noise from fine-scale turbulence. *AIAA JOURNAL* 37(2), pp. 591–615.

Terracol, M. 2005. A zonal rans/les approach for airframe trailing-edge noise prediction. *Euromech Colloquium 467: Turbulent Flow and Noise Generation, Marseille, France, July 18-20, 2005* .

Tritton, D. J. 1967. Some new correlation measurements in a turbulent boundary layer. *Journal of Fluid Mechanics* 28(3), pp. 439–462.

Tutkun, M., Georgeb, W., Delvillec, J., Stanislasd, M., Johanssone, B., Foucautd, J. and Coudertd, S. 2009. Two-point correlations in high Reynolds number flat plate turbulent boundary layers. *Journal of Turbulence* 10(21), pp. 1–23.

van der Velden, W., Pröbsting, S., van Zuijlen, A., de Jong, A., Guan, Y. and Morris,

S. 2016. Numerical and experimental investigation of a beveled trailing-edge flow field and noise emission. *Journal of Sound and Vibration* 384, pp. 113–129.

Versteeg, H. and Malalasekera, W. 2007. *An introduction to Computational fluid Dynamics, the Finite Volume Method*. Pearson.

Wang, M., Freund, J. B. and Lele, K., S. 2006. Computational prediction of flow-generated sound. *Annual Review of Fluid Mechanics* 38, pp. 483–512.

Wang, M. and Moin, P. 2000. Computation of trailing-edge flow and noise using large-eddy simulation. *AIAA Journal* 38(12), pp. 2201–2209.

WHO. 2011. Burden of disease from environmental noise: Quantification of healthy life years lost in europe. In: *Burden of disease from environmental noise: Quantification of healthy life years lost in Europe*, pp. 126–126. Available at: `http://www.euro.who.int/__data/assets/pdf_file/0008/136466/e94888.pdf`.

Wilcox, D. C. 2006. *Turbulence modeling for CFD*. DCW Industries, Inc.

Winkler, J., Carolus, T. and Moreau, S. 2009. Airfoil trailing-edge blowing: Broadband noise prediction from large-eddy simulation. *15th AIAA/CEAS Aeroacoustics Conference (30th AIAA Aeroacoustics Conference), Miami, Florida,11-13 May,2009* .

Wolf, W. R., Azevedo, J. L. F. and Lele, S. K. 2012. Convective effects and the role of quadrupole sources for aerofoil aeroacoustics. *Journal of Fluid Mechanics* FirstView, pp. 1–37. Available at: `http://dx.doi.org/10.1017/S0022112012003278`.

Appendices

Appendix A

Two-point correlation curve fits at various y/δ locations.

This appendix shows the measured spanwise and wall-normal coherence for Cases 1, 2 and 3, which were not included in the main body of the thesis in the interest of brevity.

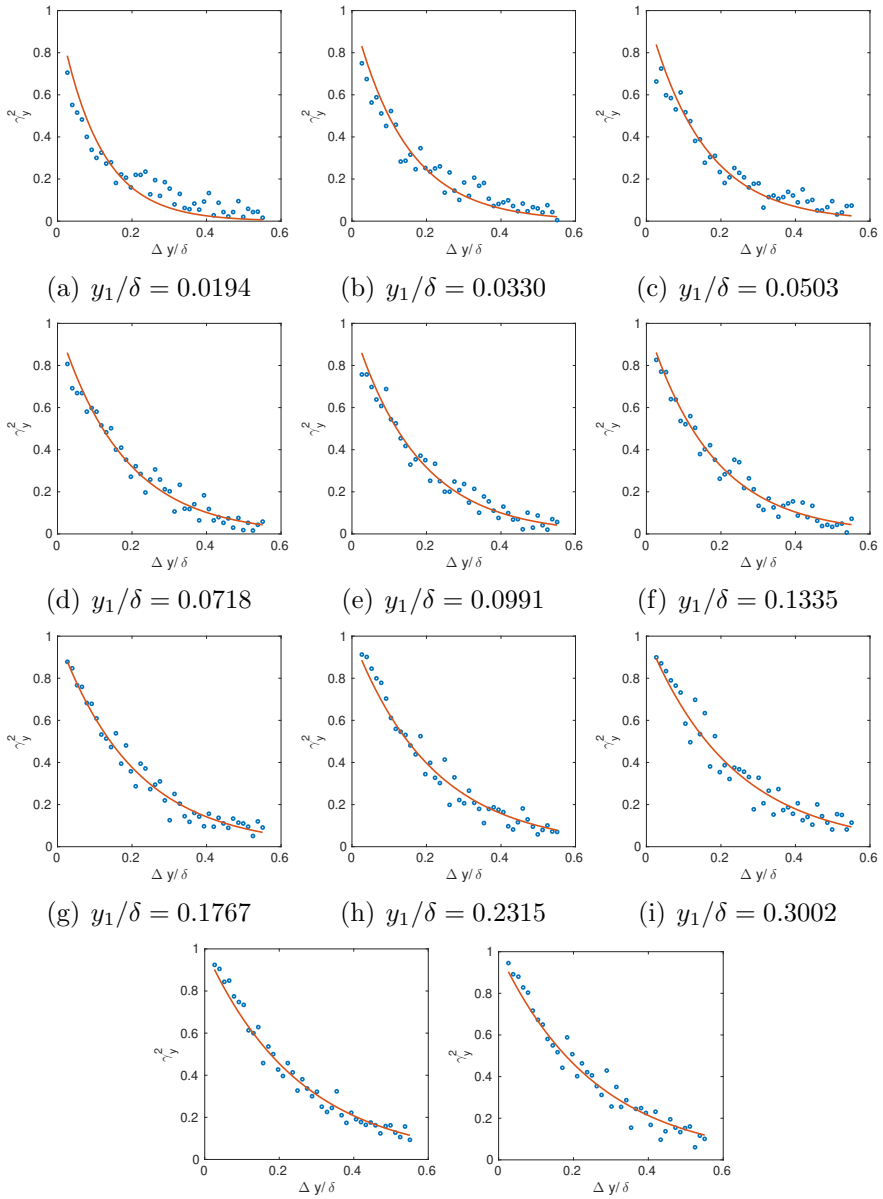

(a) $y_1/\delta = 0.0194$ (b) $y_1/\delta = 0.0330$ (c) $y_1/\delta = 0.0503$

(d) $y_1/\delta = 0.0718$ (e) $y_1/\delta = 0.0991$ (f) $y_1/\delta = 0.1335$

(g) $y_1/\delta = 0.1767$ (h) $y_1/\delta = 0.2315$ (i) $y_1/\delta = 0.3002$

(j) $y_1/\delta = 0.3867$ (k) $y_1/\delta = 0.4961$

Figure A.1: Wall-normal coherence at various wall normal distances for Case 2. Dots are experimental data, solid line is a Gaussian curve fit. $x/c = 1.0033$.

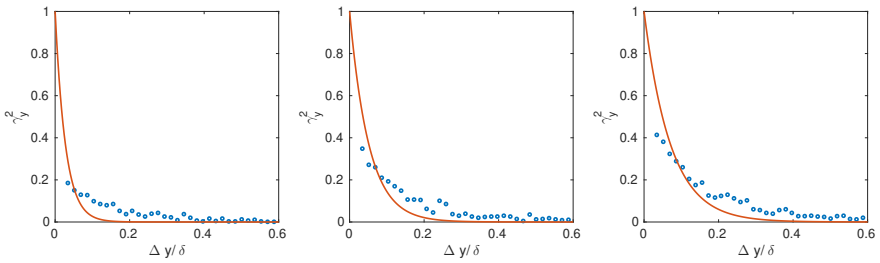

(a) $y_1 = 2$ mm (b) $y_1 = 4$ mm (c) $y_1 = 8$ mm

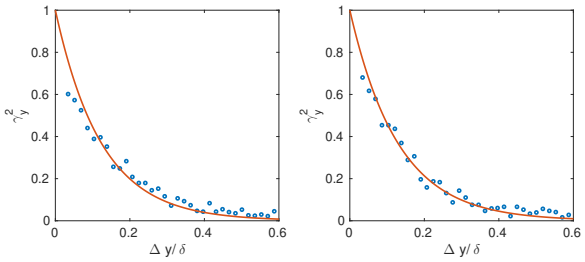

(d) $y_1 = 16$ mm (e) $y_1 = 24$ mm

Figure A.2: WallNormal coherence at various wall normal distances for Case 1. Dots are experimental data, solid line is an exponential curve fit. $x/c = 1.0033$.

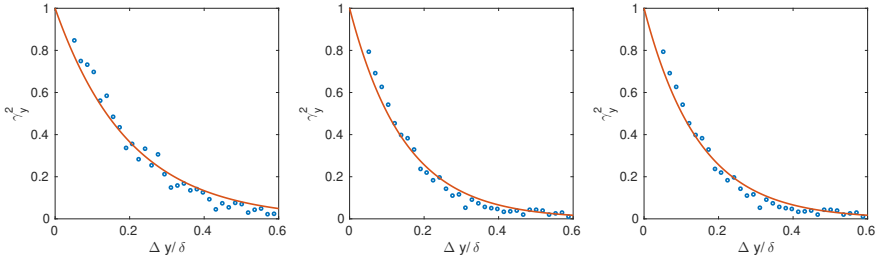

(a) $y_1/\delta = 0.069$ (b) $y_1/\delta = 0.138$ (c) $y_1/\delta = 0.276$

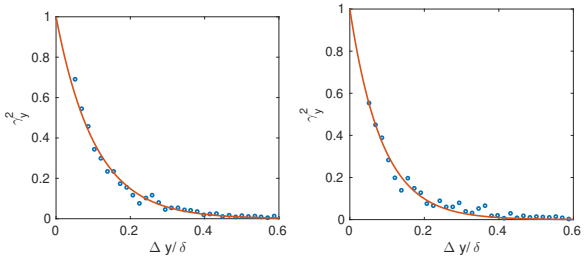

(d) $y_1/\delta = 0.553$ (e) $y_1/\delta = 0.829$

Figure A.3: WallNormal coherence at various wall normal distances for the Case 3. Dots are experimental data, solid line is an exponential curve fit. $x/c = 1.0033$.

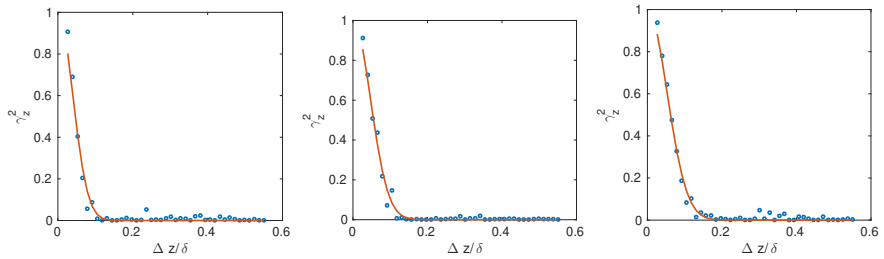

(a) $y_1/\delta = 0.0194$ (b) $y_1/\delta = 0.0330$ (c) $y_1/\delta = 0.0503$

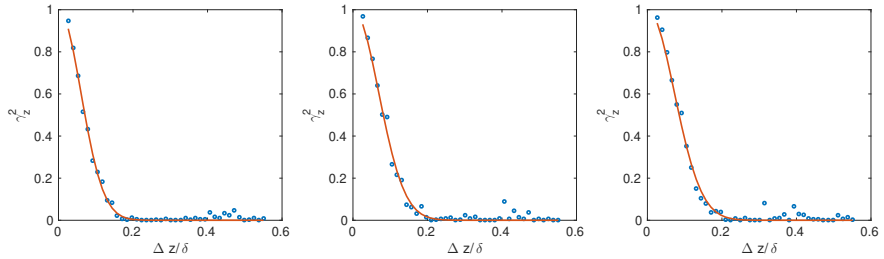

(d) $y_1/\delta = 0.0718$ (e) $y_1/\delta = 0.0991$ (f) $y_1/\delta = 0.1335$

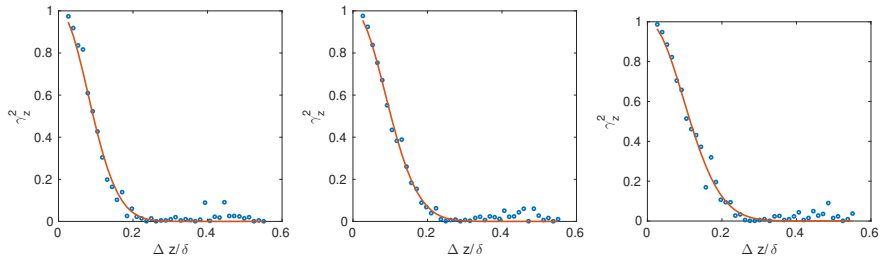

(g) $y_1/\delta = 0.1767$ (h) $y_1/\delta = 0.2315$ (i) $y_1/\delta = 0.3002$

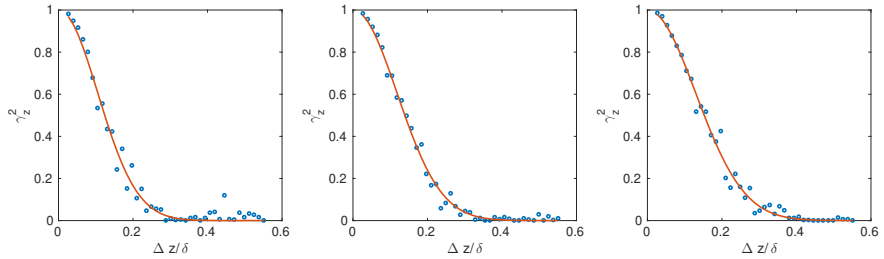

(j) $y_1/\delta = 0.3867$ (k) $y_1/\delta = 0.4961$ (l) $y_1/\delta = 0.6335$

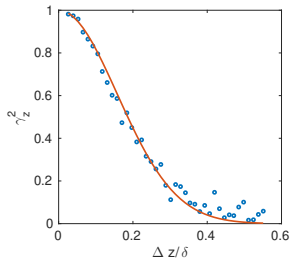

(m) $y_1/\delta = 0.8068$

Figure A.4: Spanwise coherence at various wall normal distances for Case 2. Dots are experimental data, solid line is a Gaussian curve fit. $x/c = 1.0033$.

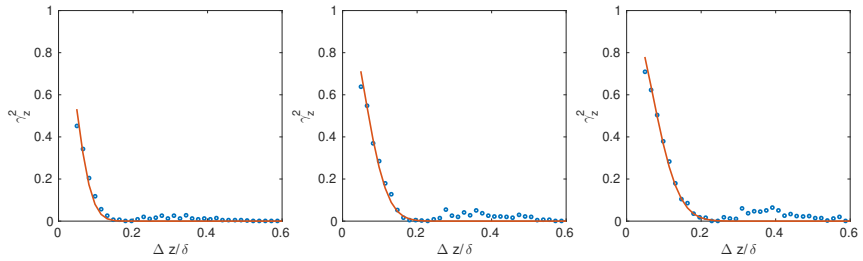

(a) $y_1/\delta = 0.065$ (b) $y_1/\delta = 0.131$ (c) $y_1/\delta = 0.261$

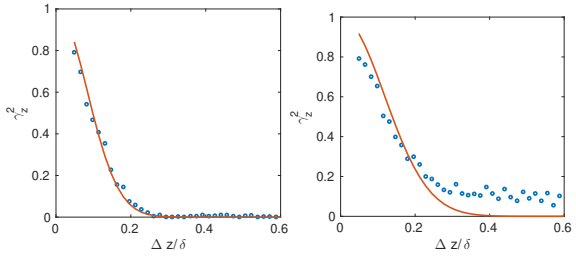

(d) $y_1/\delta = 0.522$ (e) $y_1/\delta = 0.783$

Figure A.5: Spanwise coherence at various wall normal distances for Case 1. Dots are experimental data, solid line is a Gaussian curve fit. $x/c = 1.0033$.

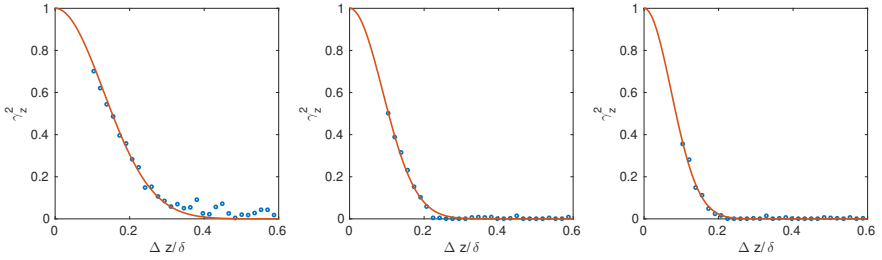

(a) $y_1/\delta = 0.0691$ (b) $y_1/\delta = 0.138$ (c) $y_1/\delta = 0.276$

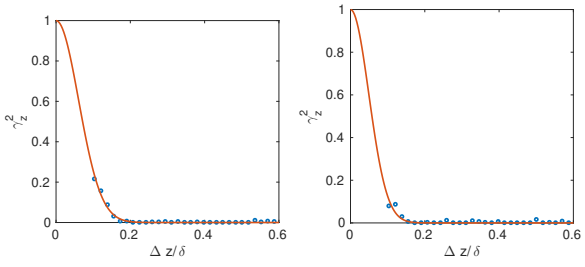

(d) $y_1/\delta = 0.553$ (e) $y_1/\delta = 0.829$

Figure A.6: Spanwise coherence at various wall normal distances for Case 3. Dots are experimental data, solid line is a Gaussian curve fit. $x/c = 1.0033$.

Appendix B

Alternative correction for finite span

B.1 RANS implementation

The power spectral density of the acoustic pressure in the far field was shown in Chapter 2 to be

$$S(\mathbf{x},\omega) = \sum_{V(\mathbf{y_1})} \sum_{V(\mathbf{y_2})} \Psi\Phi \frac{F(\mathbf{y_1})}{r_o^{3/2}(\mathbf{y_1})} \frac{F(\mathbf{y_2})}{r_o^{3/2}(\mathbf{y_2})} dV(\mathbf{y_1}) dV(\mathbf{y_2}). \tag{B.1}$$

This expression can be evaluated on the same grid used to compute the RANS solution, or interpolated onto a superimposed acoustic grid. $S(\mathbf{x},\omega)$ is proportional to the volume of the source elements $dV(\mathbf{y_2})$ and $dV(\mathbf{y_2})$. Assuming uniform grid spacing in a Cartesian coordinate system,

$$dV(\mathbf{y_2}) = dV(\mathbf{y_2}) = dx\ dy\ dz. \tag{B.2}$$

Both dx = and dy were obtained from a grid refinement study. To obtain dV, a suitable spanwise cell length dz has to be chosen. For consistency, the following choice is made:

$$dz = dx = dy = \frac{\delta}{100}. \tag{B.3}$$

In oder to calculate the noise radiated by the full span o the airfoil, a correction for the number of cells along the span must be applied.

B.1.1 Correction for finite span

Consider an airfoil of span L, as shown in Figure B.1.

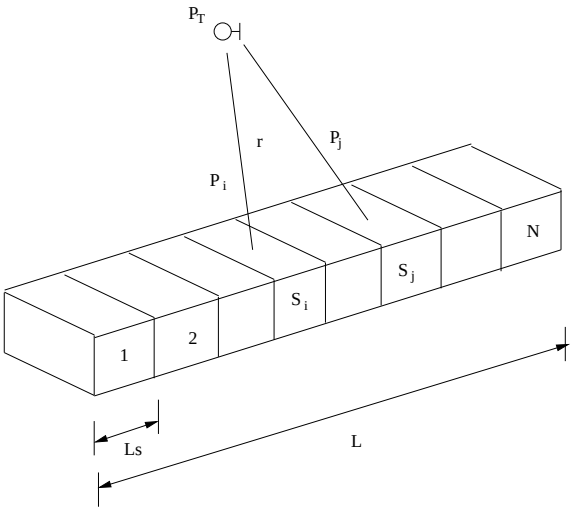

Figure B.1: Schematic of a long-span body divided by N subsections, adapted from Seo and Moon (2007)

Following Seo and Moon (2007), let the spectral acoustic pressure radiated from the i-th subsection be $|p_i|^2$, then the power spectral density of the acoustic pressure for entire span can be written as

$$S_s = p_L \hat{p_L} = \sum_i \sum_j p_i \hat{p_j}. \tag{B.4}$$

The power spectral density of the acoustic pressure radiated from each subsection is assumed to be the same,

$$|p_1|^2 = |p_2|^2 = ... = |p_N|^2 = |p_s|^2, \tag{B.5}$$

The acoustic pressure radiated from each subsection is lagged by a phase difference given by the spanwise coherence function,

$$\gamma_{ij} = \frac{p_i \hat{p_j}}{\sqrt{|p_i|^2}\sqrt{|p_j|^2}}. \tag{B.6}$$

The coherence function is a function of Δz_{ij}, which is the spanwise separation between two subsections given by

$$\gamma_{ij} = \gamma(\Delta_{ij}), \quad \Delta_{ij} = |z_i - z_j| = |i - j| L_s. \tag{B.7}$$

Then the power spectral density of the acoustic pressure emitted from the entire span can be written as

$$|p_L|^2 = \sum_i \sum_j \gamma(\Delta_{ij})|p_s|^2. \tag{B.8}$$

Assuming a Gaussian form for the spanwise coherence,

$$\gamma(\Delta_{ij}) = \exp\left(-\frac{\Delta_{ij}^2}{\ell_{sz}^2(\omega)}\right). \tag{B.9}$$

Then the power spectral density of the acoustic pressure for entire span becomes

$$S_s = \sum_i \sum_j p_s \exp\left(-|i-j|\frac{L_s^2}{\ell_{sz}^2(\omega)}\right). \tag{B.10}$$

To evaluate this equation, we require both L_s and ℓ_{sz}. The following assumption regarding the value of L_s was made:

$$L_s = dz = \frac{\delta}{100}. \tag{B.11}$$

Following Brooks and Hodgson (1981),

$$\ell_{sz} = \frac{U_c}{0.714\omega}. \tag{B.12}$$

The convection velocity is modelled as $U_c = 0.65U_\infty$. The assumptions made regarding dz and ℓ_{sz}, and the resulting frequency dependent correction will require a modification of the empirical parameters A and c_τ, which will have to be re-tuned. Due to time constraints, this will be done as future work.